Politecnico di Torino

Corso di dottorato in Fisica

XXVII ciclo

Generalization of the Eliashberg equations and Density Functional Theory applied to the analysis of the fundamental properties of iron-based superconductors.

Doctoral Thesis

Author:
Sara Galasso

Supervisor:
Giovanni A. Ummarino

March 2015

"If we knew what it was we were doing,
it would not be called research,
would it?"

Albert Einstein

Abstract

Density Functional Theory (DFT) allows a fully *ab-initio* treatment of almost all the quantities that enter in the Eliashberg theory and in many other approaches used to study both the superconducting and the normal phase. A complete description from *first principles* of real materials is, al least in principle, possible. Here DFT and Eliashberg theory are applied to the study of some members of the new family of superconductors discovered in 2008, the iron-compounds. Superconductivity here is unconventional and unlikely mediated by phonons. When electronic mechanisms are involved and the properties of the compounds are more complex, as in the case of Fe-based superconductors, also the *ab-initio* treatment may require some reasonable *ad hoc* approximations, derived from experimental evidences or theoretical argumentations, introducing some phenomenological aspects in the formulation. In this thesis, Eliashberg theory and DFT are applied to study the properties of some iron compounds, in particular the properties of LiFeAs and Co-doped Ba-122 are discussed both in the normal and in the superconducting state.

In order to unveil the the properties of the superconducting state, in particular the symmetry and the amplitude of the order parameter and the coupling mechanism, a four bands Eliashberg model is discussed for LiFeAs suggesting that the specific electronic structure of this peculiar compound may lead to the breakdown of the Migdal's theorem forcing the model to be "phenomenological". The relation between the topology of the Fermi surface and the presence of nodes is studied in Point-contact Andreev-reflection spectra of $Ba(Fe_{1-x}Co_x)_2As_2$ (both thin films and single crystals) and $Ca(Fe_{1-x}Co_x)_2As_2$. The curves presented are fitted within the multiband 3D-BTK model that allows the inclusion of the real shape of the Fermi surface evaluated within DFT.

Thanks to the inclusion of the results obtained within the Eliashberg theory in the 2D-BTK model some additional structures due to the strong electron-boson interaction, that appear at energy higher than the amplitude of the gaps in some AR spectra, can be studied and some guesses about the nature of the superconducting mechanism can be made. This technique is here applied to the case of $Ba(Fe_{1-x}Co_x)_2As_2$ thin films with $x = 0.08$.

Finally, as concern the normal state, the temperature dependence of resistivity is reproduced both in LiFeAs and $Ba(Fe_{1-x}Co_x)_2As_2$ with a model that contains two different kind of carriers. For both compounds spin fluctuations play an important role also in the normal state in addition to being the main bosons that mediate the Cooper pairing and in both compound the transport coupling

constant results to be sensibly smaller than the superconducting one, suggesting a way to find a unifying principle for HTCS.

Acknowledgements

Alla fine di questi tre anni di dottorato è un piacere ringraziare il mio supervisor, Giovanni Ummarino, che mi ha aiutato ogni giorno a non perdere la calma, a superare le difficoltà, a cercare di capire le cose sempre più approfonditamente e infine a non perdere mai il sorriso.
Un grande grazie a tutto il La.T.E.S.T group, in particolare al Prof. Renato Gonnelli che mi ha mostrato che la passione è l'ingrediente fondamentale per dare giusto sapore alla ricerca, al Prof. Dario Daghero che ha sempre cercato di rispondere alle mie domande, specialmente riguardo l'aspetto più sperimentale e a Mauro perché ottimi scambi di idee possono avvenire anche in pausa caffè. Ringrazio Erik, Cristina e tutta la stanza dottorandi per la compagnia e per il supporto quotidiano.
Al Dr. Emmanuele Cappelluti un grazie infinito per i consigli che mi ha dato, ma soprattutto per le importanti e talvolta illuminanti discussioni.
Un doveroso grazie al Prof. Dr. E. K. U. Gross per avermi ospitato al Max Plank Institute di Halle e al Dr. Antonio Sanna per aver avuto la pazienza di lavorare con me e per avermi insegnato tantissimo.

Il pensiero più grande è rivolto senza dubbio ai miei genitori senza cui non avrei avuto la possibilitá di intraprendere il percorso che mi ha condotto fino a questo punto e a Riccardo che prosegue al mio fianco, condividendo con me i momenti gioiosi e mi aiuta ad affrontare quelli che lo sono meno.

Ringrazio Roby, Ale e Giuliano perché la certezza che ci saranno sempre mi fa stare bene.
Ringrazio Ilaria, perché condividere le fatiche le rende sicuramente più lievi.
Ad Arianna vielen Dank! Perché trovare una grande prof. è raro, ma trovare un'amica lo è di più!
A Davide, Stefano a Sem, alla Luta, a Silvia e a Noel un grazie speciale perché gli Schnitzel sono gli Schnitel!
A Grazia, a Delfo, a Paolino e Donatella, a J, a Korwin, al Priore, a Paz, a Marcella e a tutti "i fisici" un pensiero... perché comunque è sempre un piacere!
Un abbraccio gigante lo mando agli amici che si sono trasferiti, a Daniele e a Federico, che comunque sia, mancano.

Ci sia allontana, la vita ogni tanto si diverte a complicare un po' le cose, gli impegni a volte ci sovrastano ma non ci si perde mai.

Contents

List of Figures

List of Tables

Abbreviations

AF	**A**nti - **F**erromagnetic
ARPES	**A**ngle **R**esolved **P**hoto - **E**mission **S**pectroscopy
BTK	**B**londer-**T**inkham-**K**lapwijk
BZ	**B**rillouin **Z**one
DFT	**D**ensity **F**unctional **T**heory
DOS	**D**ensity **O**f **S**tates
FeSC	**I**ron - based **S**uperconductor
FS	**F**ermi **S**urface
FP	**F**ull **P**otential
GGA	**G**eneralized **G**radient **A**pproximation
HK	**H**ohenberg - **K**ohn
HTCS	**H**igh **C**ritical **T**empetrature **S**uperconductivity
INS	**I**neslastic **N**eutron **S**cattering
KS	**K**ohn-**S**ham
LAPW	**L**inearised **A**ugmented **P**lane **W**ave
LDA	**L**ocal **D**ensity **A**pproximation
OP	**O**rder **P**arameter
PCARS	**P**oint **C**ontact **A**ndreev-**R**eflection **S**pectroscopy
SC	**S**ingle **C**rystals
SDW	**S**pin **D**ensity **W**ave
SF	**S**pin **F**luctuation
TF	**T**hin **F**ilms
VCA	**V**irtual **C**rystal **A**pproximation

Ai miei genitori e a Riccardo,
che mi sono accanto
e che mi incoraggiano
ogni giorno

Chapter 1

Iron based superconductors

For more than twenty years cuprates have attracted the attention of physicists, however the nature of high-temperature superconductivity (HTCS) in these class of material is still not completely understood. In this direction, the discovery of iron-based superconducting compounds has given a new motivation to study superconductivity, with the hope that the comprehension of this new class of material can provide other elements and new points of view in solving the open questions about cuprates.
In this chapter the wide framework of iron compounds will be reviewed, clarifying where the work of this thesis is located with respect to the worldwide research. I will give general overview, focusing on the electronic properties, the role of magnetic fluctuations and other electron-electron interactions and as concern the superconducting phase, I will also discuss the possible Cooper pairing mechanisms and the symmetries of the order parameter.

"The philosopher is in love with truth, that is, not with the changing world of sensation, which is the object of opinion, but with the unchanging reality which is the object of knowledge."
Plato

1.1 Introduction

In 2006 the Hosono's group observed the superconducting transition in LaFePO [1] at a relatively low temperature, T_c= 4 K. However the great breakthrough was in 2008 when a similar superconductor, $LaFeAsO_{1-x}F_x$ [2] was discovered by the same research group. This compound presents a critical temperature that reaches 26 K when the fluorine content is $x = 0.11$. A so high critical temperature suggests an unconventional pairing mechanism and the possibility to find

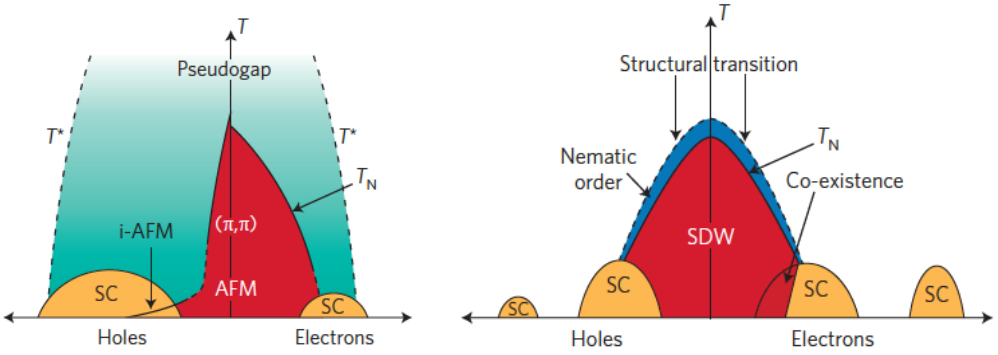

Figure 1.1: Schematic phase diagrams of cuprates on the left and of iron based superconductors on the right. Taken from [8].

similar compounds with even higher critical temperatures. Indeed other structural types of iron-based superconductors (FeSCs) were synthesized.
Considering bulk iron-based superconductors, the highest critical temperature obtained without applying pressure is 55 K in $SmO_{1-x}F_xFeAs$ [3]. On the basis of these researches many other superconducting iron-compounds have been discovered [4–7]. During the later years many efforts have been spent to investigate the physical properties of this new family of superconductors: they share same characteristics with HTCS cuprates, such as the layered structure that implies a quasi-two dimensional Fermi surface. Generally, in iron-based compounds, superconductivity appears in the proximity or even in coexistence of antiferromagnetism and then, as cuprates, they are supposed to be unconventional superconductors, i.e. phonons mediated superconductivity is unlikely. On the other hand, FeSCs have a lot of properties that tell them apart from cuprates. First of all the parent compounds of cuprates show strong electron correlations and they are antiferromagnetic Mott insulators while FeSCs arise from metallic parent compounds. For what concerns the superconducting state the two families appear to be very different, cuprates show a single band superconductivity (with a *d*-wave symmetry) while iron compounds are more complex showing a Fermi surface with several sheets, then they generally are multi-band superconductors (more details will be given in the next paragraphs). Even though cuprates have been studied for about 25 years, many questions about their physical properties are still open. In this direction the discovery of a new family of superconductors gave researchers a new motivation to keep studying the key features of HTCS. In Figure 1.1 the schematic phase diagram of iron compounds is compared to that of cuprates. At a first glance the two schemes look very similar, however there are several differences, for instance, even if both of them present a magnetic order at zero doping, in cuprates it is a conventional antiferromagnetic order while in iron compounds it is usually a stripe ordering.

1.2 Basic Properties

More than thousand iron-compounds have already been discovered. Among this huge variety a lot of common properties can still be found. First of all two different classes can be distinguished: iron-pnictides, where the combination "FePn" is always present (Pn=As or P) and iron-chalcogenides, with "FeCh" (Ch=S, Se or Te). The former can be further divided into four classes on the basis of the crystal structure, while the later into two. Then, up to now, six different classes of iron-compound are known. The most relevant for this thesis are reported in Figure 1.2

1.2.1 Cristal structures

The six different classes of iron compounds all share a quasi two-dimentional layered structure Fe_2X_2 (where X=Pn or Ch) that is then intercalated with other elements. The Fe_2X_2 structure is built of tetrahedra with a $\bar{4}m2$ site symmetry where the X ions form a distorted tetrahedra around the Fe ions, giving rise to two different X-Fe-X bond angles. The Figure 1.3 show the "FeAs" layered structure.
The first iron based superconductor discovered ($LaFeAsO_{1-x}F_x$ [2]), obtained with doping from LaOFeAs, is the representative of the 1111 family. Soon after the substitution of lantanium with samarium allowed a growing of the critical temperature up to 55 K. These LnFeAsO compounds contain rare earth (Ln=La, Sm, Gd, etc.), transition metal (Fe, Co, Ni), pnictogen (As, P) and oxigen. They have a primitive tetragonal structure at room temperature, with space group $P4/nmm$ (No. 129) with 8 atoms per unit cell and undergo a structural transition in an orthorombic phase with space group $Cmma$.
The so called 122-class contains compounds like $AeFe_2As_2$, where Ae is a metallic alcaline element, i.e. Ca, Sr, Ba, Eu, K etc. Compounds belonging to this class adopt a body-centered tetragonal structure with the $I4/mmm$ spacegroup (No. 139). In Figure 1.2 is reported the $BaFe_2As_2$ as an example. Here FeAs layers are intercalated by single atoms and the unit cell contains 10 atoms with one Ae atom in the center. Among this class the highest critical temperature is 49 K achieved in Pr-doped $CaFe_2As_2$ [10].
Another class include peculiar compounds such as LiFeAs (reported in Figure 1.2), NaFeAs or LiFeP and thus denominated 111. AFeAs compounds crystallize in a structure with $P4/nmm$ symmetry and the unit cell contains two chemical formula, then six atoms. Here the FeAs layered structure is intercalated by two planes of A atoms.

The simplest structure among iron based superconductor is the 11 type and it is assumed by FeSe (T_c = 8 K). The space group adopted in this case is again

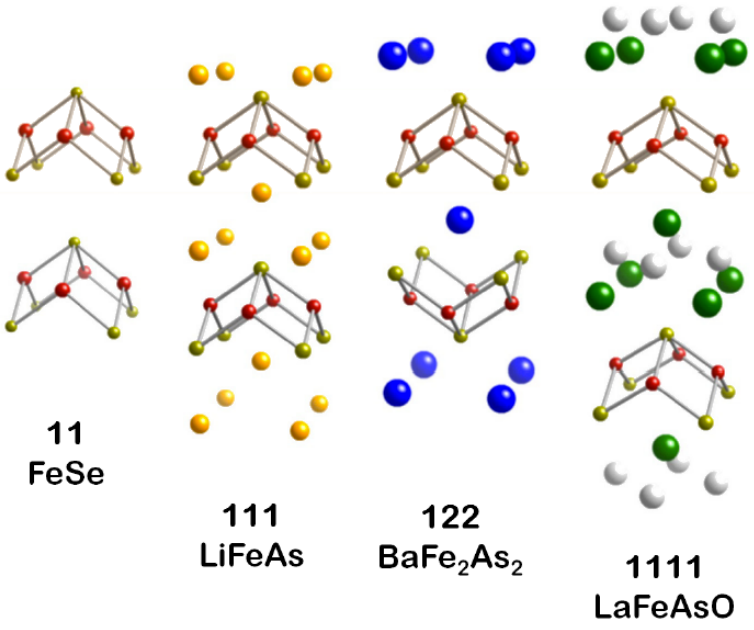

Figure 1.2: Crystallographyc structure of the Iron-based superconductors. Adapted from [9].

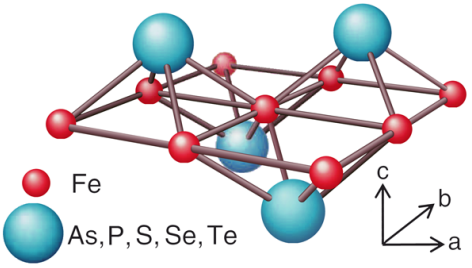

Figure 1.3: Schematic view of the FeX layer. Adapted from [11].

P4/nmm but here layers of Fe_2As_2 come in succession. Again each Fe atom is coordinated with four Se atoms and then they form the classical tetrahedrum. Moreover, there is the 21311 class (also called 43622) to which belong for example $Sr_4Sc_2O_6Fe_2P_2$ where $SrFe_2P_2$ are intercalated with perovskite layers $Sr_4Sc_2O_6$. Finally it was discovered the 122* class, the most recent discovered, with compounds that can be written as $A_xFe_{2-y}Se_2$ where A=K, Rb, Cs or Tl but this structure can be viewed as FeSe intercalated with the A element.

1.2.2 Geometry and superconductivity

It it quite commonly accepted that the geometry of the tetrahedra FeX_4 influences drastically the electronic, the magnetic and then also the superconducting properties of these systems. For example the highest critical temperature can be obtained when the bond angle As-Fe-As is close to the ideal value of $\sim 109.47°$ [12, 13], as can be seen in the left panel of Figure 1.4.
Another important parameter that influences the superconducting state is the anion heigh from the Fe layer. This distance depends on the anion and the variation of the critical temperature related to this parameter is reported in the right panel of Figure 1.4. This behavior seems to be a peculiar characteristic shared by at least 1111, 122, 111, 11 iron-based superconductors, there is just a little exception for the FeSe-derived materials.

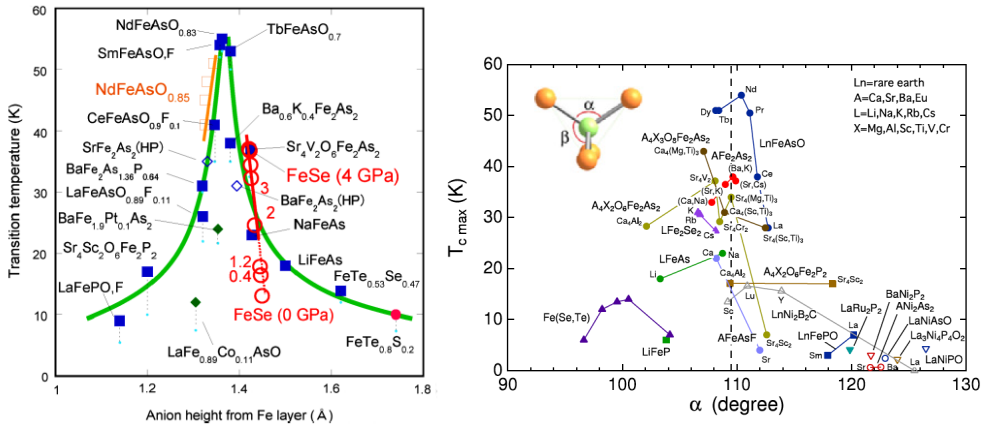

Figure 1.4: Relationship between geometry and superconductivity: Anion height dependence of T_c for the typical Fe-based superconductors, taken from [12] in the left panel and Relation between the As-Fe-As angle and T_c, taken from [**?**]

1.3 Normal state properties

Although composed of different elements, generally speaking, the properties of iron-compounds are quite similar among these materials.
In the next few paragraphs the electronic, magnetic and coupling properties will be discussed.

1.3.1 Electronic properties

The electronic properties of iron compounds are strongly determined by the Fe atoms [14–16]. As already explained, iron compounds are metals or semimetals,

and not Mott insulators as cuprates, with all five $3d$ orbitals giving contribution to the Fermi surface (FS). In Figure 1.5, in order to give an example, the FS of two iron compounds are illustrated.
On the basis of the FS topology, all the iron compounds can be divided in two big categories: systems having both electron and hole pockets and systems with only electron sheets. Most of the iron pnictides and Fe(Se,Te) belong to the first category while heavily electron doped iron pnictides, FeSe single layer and $A_xFe_{2-y}Se_2$ belong to the second category. The exact number of the hole and

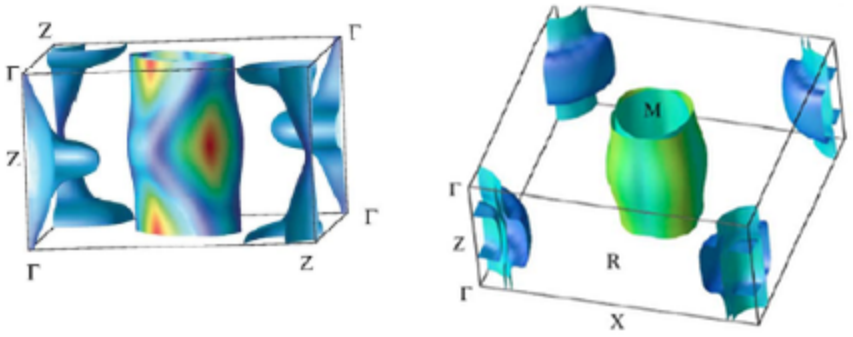

Figure 1.5: 3D view of the Fermi surface of $Ba(Fe,Co)_2As_2$ and of LaFeAsO.

electron bands depends on the specific compound, but generally speaking there are 2-4 hole bands centered in the Γ $[(0,0)]$ point and 2-3 electron bands in M $[(\pi,\pi)]$, if the *folded* Brillouin zone is considered. The 2D character of the FS is not so universal, it is very pronounced in the 1111 family, and less remarkable in the 122 compounds. This characteristic strongly depends on the value of doping that changes the dimension of hole and electron pockets, leading to a reduction of the degree of the nesting condition [15] with important implication on superconductivity, as will be discussed in Chapter 5 in the case of Co-doped $BaFe_2As_2$.

1.3.2 Nematic Phase

Even if the presence of a nematic order in iron-based superconductors is now commonly accepted and confirmed by experimental measurements, its origin remains unclear. Nematic order breaks the discrete lattice rotational symmetry, preserving the time-reversal and translational symmetries. This can be caused by a regular structural transition or by an electronically driven instability.
At first sight, one might view this tetragonal-to-orthorhombic transition as a regular structural transition driven by lattice vibrations (phonons). However, some theoretical works [17, 18] suggested that the tetragonal-to-orthorhombic transition may be driven by electronic rather than lattice degrees of freedom.

Experimental evidences of electronic anisotropies (for instance the d.c. resistivity [19]) not proportionate to the corresponding anisotropy of the lattice parameters well support this idea. Then this transition is probably driven by the same fluctuations that give rise to superconductivity and magnetic order.
Electronic nematic phases have been proposed in other unconventional superconductors, such as high-Tc cuprates and heavy-fermion materials. An electronically driven nematic state in FeSCs would be in line with a generic reasoning that the pairing in all these correlated electron systems has the same origin. It is likely that magnetic fluctuations drive the nematic instability. In any case, all three orders (spin-driven Ising-nematic, orbital, and structural) appear simultaneously below T_{nem}. It is unlikely that nematic fluctuations can mediate superconductivity as spin or charge fluctuations, as it involves small momentum transfer, but nematic fluctuations may nevertheless enhance T_c by reducing the bare intra-pocket repulsion. Intra-pocket interactions, however, in general do not select the relative sign of the gaps in different pockets. Below T_c nematic order has been found to compete with superconductivity [20, 21], as density-wave orders do. A special case in which nematicity strongly affects T_c is when s-wave and d-wave superconducting instabilities are nearly degenerate, as was suggested to be the case for strongly hole-doped and strongly electron-doped FeSCs. In this situation nematic order leads to an enhancement of T_c by lifting the frustration associated with the competing pairing states [22, 23].

1.3.3 Magnetism and spin fluctuations

Although different families of FeSCs exhibit different phase diagrams, all of their parent compound are characterized by an anti-ferromagnetic (AF) order. This suggests that magnetic excitations play an important role in the coupling pairing that induces superconductivity [24, 25].
The parent compounds of the 11, 1111 and 122 families share the AF collinear structure and the presence of nesting between hole and electron bands (in Γ and M points respectively) leads to a quite noticeable peak in static magnetic susceptibility $\chi_0(\mathbf{q})$, with $\mathbf{q} = (0, \pi)$ and $\mathbf{q} = (\pi, 0)$. This lead to an antiferromagnetic instability and to the formation of spin density wave (SDW) with the appropriate wave vector.
However, in $Fe_{1-y}Te$ compound the spin structure is bi-collinear and then the antiferromagnetic wave vector is $\mathbf{Q}_{AF} = (\pi/2, \pi/2)$ incompatible with the nesting. Then this suggests that the only cause of the AF instability cannot be only the presence of FS nesting.
It is observed that in the electron-overdoped region the spin fluctuations (SF) vanish as well as the hole bands and the superconducting transition does not take place [26]. Moreover the correlation between the spin excitation in the normal

stateand electronic structure is found to be common to for all FeSCs. Finally the "resonance peak" in the spectrum of the spin fluctuations (i.e. the resonance in the spin susceptibility) is present in almost all FeSC in the superconducting state. All these facts strongly support a SF-mediated superconductivity, with important implications on the symmetry of the order parameter (OP) that will be discussed in Section 1.4. SFs provide also an explanation for the differences in the calculated band structure with respect to the experimental data: they dress the single-electron excitation causing a mass renormalization (with a factor 2-2.5) compatible with experiments. Obviously the AF order depends on doping. Generally speaking, electron-doping suppresses the AF order and a resonance is present for low-energy spin excitation that couples to superconductivity [27]. In the overdoped region, spin fluctuations become weaker and more transversally elongated with a reduction of superconductivity. Finally, further increasing the electron doping superconductivity disappears. Electron doping mostly modify the low energy excitation and leave almost unchanged the high energy part of the spectrum suggesting that these arise from itinerant magnetism, while on the other hand the hole doping suppresses the high-energy spin excitations.

1.4 Superconducting state

In conventional superconductors the pairing of the Cooper pairs is provided by phonons. Since the discovery of cuprates new possibilities for the mediating bosons have been taken into account, suggesting a singlet d-wave symmetry where the gap changes sign on the FS (in this case composed by a single sheet). As already discussed and highlighted in Figure 1.1 in a similar way to cuprates in the new class of superconductors of iron based superconductivity emerges in close proximity of the magnetic phase. Also in this case this fact suggests an unconventional pairing mechanisms. Anyway the situation appears to be a little bit different with respects the previous case of cuprates, indeed now the FS is built of several hole and electron bands and then a multiband superconductivity can be also possible. In order to characterize the superconducting state the mediating bosons and the characteristics of the gap have to be analyzed. As will be discussed hereafter these two characteristics are strongly tied one to the other however even considering all the differences between cuprates and iron compounds it is quite commonly accepted that superconductivity is induced by the same mechanism.

1.4.1 Coupling mechanism and symmetry of the order parameter

As soon as the first iron compound was discovered, conventional superconductivity has been immediately ruled out [25]. DFT calculations on the electron-phonon interaction demonstrate that some moderate coupling exists, but it is not strong enough ($\lambda \sim 0.2$) to justify the high critical temperature and this fact is also confirmed by experimental measurements made on several compounds.
However the presence of a large resonance peak in the magnetic susceptibility in these compounds [2] suggests a nearness to critical point and a non trivial contribution between different sheets of the FS.
Spin fluctuations are pair breaking and then, if a singlet superconducting state is taken into account, they need a sign-change of the order parameter somewhere in the Brillouin zone in order to create a Cooper pair. In cuprates, where a single band superconducting state takes place, this condition is realized thanks to the *d*-wave symmetry. If the FS is more complex and several sheets are present then

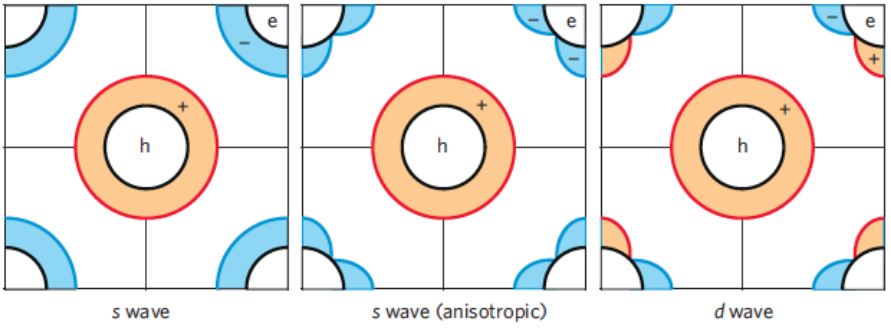

Figure 1.6: Possible symmetries of the order parameter in FeSC.

a multiband superconductivity may appear and various possible gap symmetries are allowed, at least theoretically, even within the picture of spin-fluctuation mediated pairing. These possibilities are shown in Figure 1.6: thanks to the presence of disconnected sheets in the FS the sign-changing can be realized with a node either away from the Fermi energy, realizing so-called $s\pm$ or directly at the Fermi energy, giving rise to a *d*-wave symmetry. Moreover, in some cases, also a modulation of the gap amplitude can occur even in the case of *s*-symmetry, in this case accidental nodes appear. In FeSC a *d*-wave symmetry is unlikely because it would require an unconvincing, strong $\mathbf{q}$ dependence of the interaction on a relatively small FS, however some case of strongly overdoped compounds may show this kind of symmetry, while the presence of nodes will be discussed in Chapter 5.
In most of optimally-doped compounds, the so-called s± symmetry with isotropic OPs of opposite sign on the holelike and electronlike FS sheets is realized [25],

but the emergence of nodes or zeros on some FSs is theoretically predicted in various situations [28, 29].

Chapter 2

Theoretical Background: The Normal State

In this chapter the theoretical methods used to describe the normal state of the systems under study are explained. DFT is nowadays one of the most popular methods for *ab initio* calculations and it provides an alternative way, with respect to the experiments, to investigate the condensed matter systems. It will be clear after reading the next chapter that some parameters characterizing the normal state are necessary to study the superconducting phase. Here the basic concepts of DFT and the fundamental properties of the ELK code used for the electronic structure calculations are presented. Generally speaking, the most widely used programs today are based on the Kohn-Sham ansatz that replaces the original many-body problem by an auxiliary independent-particle system, introducing a fictitious and effective Kohn-Sham single-particle potential. The many-body effects are approximated by a so-called *exchange-correlation* functional in the effective Kohn-Sham single-particle potential.

"If the facts don't fit the theory, change the facts."
A. Einstein

2.1 Introduction

The main idea of DFT is to describe a many-body interacting system through a unique variable, the *particle density*, instead of the usual many-body wavefunction.
The starting poi of DFT is the Born-Oppenheimer approximation which separates the electron Hamiltonian from that of nuclei thanks to the huge difference between their masses that implies the motion of electrons to be considerably

faster then the nuclear motion. This means that one can consider that the electrons are moving in a static external potential $E_{ext}(\mathbf{r})$ generated by the nuclei. Then the Hamiltonian of the system is reduced to:

$$\begin{aligned} H &= \underbrace{-\frac{\hbar^2}{2m_e}\sum_i \nabla_i^2}_{\hat{T}} \underbrace{-\sum_{i,I}\frac{Z_i e^2}{|\mathbf{R_I}-\mathbf{r_i}|}}_{\hat{V}_{ext}} + \underbrace{\frac{1}{2}\sum_{i\neq j}\frac{e^2}{|\mathbf{r_i}-\mathbf{r_j}|}}_{\hat{V}} \\ &\quad \underbrace{+\frac{1}{2}\sum_{I\neq J}\frac{Z_I Z_J e^2}{|\mathbf{R_I}-\mathbf{R_J}|}}_{\hat{V}_{NN}}. \end{aligned} \tag{2.1}$$

It is important to note that the last term, that corresponds to the nuclear repulsion, contributes to the total energy with constant quantity, then it can be removed. However the remaining problem is still too complex to be solved for large systems.
The breakthrough for computational physics was reached with the development of DFT by Hohenberg and Kohn [30] and Kohn and Sham [31].

2.2 The Hohenberg-Kohn theorems

In 1964 Hohenberg and Kohn (HK) states two theorems that are the basis of DFT.
These two theorems refer to the fundamental state without magnetic field, even if they can be generalized also to this situation.

2.2.1 The first HK theorem

The ground state particle density $n_0(\mathbf{r})$ of a system of interacting particles in an external potential $V_{ext}(\mathbf{r})$ uniquely determines the external potential $V_{ext}(\mathbf{r})$, except for a constant.

That is to say, there is a one-to-one mapping between the ground state density $n_0(\mathbf{r})$ and the external potential $V_{ext}(\mathbf{r})$, although the exact formula is unknown. This means that the ground state particle density determines the full Hamiltonian, except for a constant shift of the energy, and then, at least in principle, all the states including ground and excited states of the many-body wavefunctions can be calculated. The ground state particle density uniquely determines all properties of the system completely.

2.2.2 The second HK theorem

There exists a universal functional $F[n(\mathbf{r})]$ of the density, independent of the external potential $V_{ext}(\mathbf{r})$, such that the global minimum value of the energy functional $E[n(\mathbf{r})] \equiv \int n(\mathbf{r})V_{ext}(\mathbf{r})d\mathbf{r} + F[n(\mathbf{r})]$ is the exact ground state energy of the system and the exact ground state density $n_0(\mathbf{r})$ minimizes this functional.

Thus the exact ground state energy and density are fully determined by the functional $E[n(\mathbf{r})]$. The HK theorems can be generalized to spin density functional theory with spin degrees of freedom [32]. In this theory, there are two types of densities, namely, the particle density $n(\mathbf{r}) = n\uparrow(\mathbf{r}) + n\downarrow(\mathbf{r})$ and the spin density $s(\mathbf{r}) = n\uparrow(\mathbf{r}) - n\downarrow(\mathbf{r})$ where $\uparrow$ and $\downarrow$ denote the two different kinds of spins.
Although HK theorems put particle density $n(\mathbf{r})$ as the basic variable, it is still impossible to calculate any property of a system because the universal functional $F[n(\mathbf{r})]$ is unknown. This difficulty was overcome by Kohn and Sham [31] in 1965, who proposed the well known Kohn-Sham ansatz.

2.3 The Kohn-Sham ansatz

Even if the HK theorems are the basis of DFT, they are not sufficient to make the problem solvable. One more step is essential and it is the Kohn-Sham (KS) ansatz [31] that makes DFT calculations possible.
The KS ansatz states that the ground state density of the original many-body interacting system is equal to that of some chosen fictitious independent-particle system with all the difficult many-body term incorporated into an excange-correlation functional of the density. It maps the original interacting system with real potential into a fictitious non-interacting system whereby the electrons move within an effective Kohn-Sham single-particle potential $V_{KS}(\mathbf{r})$. This auxiliary system is then described (if $\hbar = 1$, $m_e = 1$, $e = 1$) by the Hamiltonian:

$$\hat{H}_{KS} = -\frac{1}{2}\nabla^2 + V_{KS}(\mathbf{r}). \tag{2.2}$$

For a system with N independent electrons, the ground state can be obtained by solving N one-electron Shrödinger equations,

$$\left(\frac{1}{2}\nabla^2 + V_{KS}(\mathbf{r})\right)\psi_i(\mathbf{r}) = \varepsilon_i\psi_i(\mathbf{r}); \tag{2.3}$$

then the density of the auxiliary system can be constructed

$$n(\mathbf{r}) = \sum_{i=1}^{N} |\psi(\mathbf{r})|^2, \tag{2.4}$$

with the condition

$$\int n(\mathbf{r})\mathrm{d}\mathbf{r} = N. \tag{2.5}$$

And then the universal functional $F[n(\mathbf{r})]$ is written in the following form

$$F[n(\mathbf{r})] = T_s[n(\mathbf{r})] + E_H[n(\mathbf{r})] + E_{XC}[n(\mathbf{r})], \tag{2.6}$$

where $T_s[n(\mathbf{r})]$ is the non-interacting independent-particle kinetic energy, $E_H[n(\mathbf{r})]$ is the classic electrostatic Hartree energy of electrons

$$E_H[n(\mathbf{r})] = \frac{1}{2}\int\int \frac{n(\mathbf{r})n(\mathbf{r}')}{|\mathbf{r}-\mathbf{r}'|}\mathrm{d}\mathbf{r}\mathrm{d}\mathbf{r}' \tag{2.7}$$

and $E_{xc}[n(\mathbf{r})]$ is the exchange-correlation energy, which contains all the differences between the exact and the non-interacting kinetic energies and also the non-classical contribution to the electron-electron interaction.
The ground state energy then can be obtained minimizing the energy functional $E[n(\mathbf{r})] = F[n(\mathbf{r})] + \int n(\mathbf{r})V_{ext}(\mathbf{r})\mathrm{d}\mathbf{r}$, under the constrain of conservation of the number of electrons:

$$\delta\left\{F[n(\mathbf{r})] + \int n(\mathbf{r})V_{ext}(\mathbf{r})\mathrm{d}\mathbf{r} - \mu\Big[n(\mathbf{r})\mathrm{d}\mathbf{r} - N\Big]\right\} = 0 \tag{2.8}$$

where μ is the chemical potential.
Then the resulting equation is

$$\mu = \frac{\delta T_s[n(\mathbf{r})]}{\delta n(\mathbf{r})} + V_{KS}(\mathbf{r}) \tag{2.9}$$

and

$$\begin{aligned} V_{KS}(\mathbf{r}) &= V_{ext}(\mathbf{r}) + V_H(\mathbf{r}) + V_{XC}(\mathbf{r}) \\ &= V_{ext}(\mathbf{r}) + \frac{\delta E_H[n(\mathbf{r})]}{\delta n(\mathbf{r})} + \frac{\delta E_{XC}[n(\mathbf{r})]}{\delta n(\mathbf{r})} \end{aligned} \tag{2.10}$$

is the KS one-particle potential and in particular

$$V_H(\mathbf{r}) = \frac{\delta E_H[n(\mathbf{r})]}{\delta n(\mathbf{r})} = \int \frac{n(\mathbf{r}')}{|\mathbf{r}-\mathbf{r}'|}\mathrm{d}\mathbf{r}', \tag{2.11}$$

$$V_{XC}(\mathbf{r}) = \frac{\delta E_{XC}[n(\mathbf{r})]}{\delta n(\mathbf{r})} \tag{2.12}$$

are the Hartree potential and the exchange-correlation potential.
The equations (2.3) and (2.10), with the definition (2.4) are the KS equations. They have to be solved in a self-consistent way because $V_{KS}(\mathbf{r})$ depends on the density $n(\mathbf{r})$ through the xc potential.
Although exact in principle, the KS theory is approximate in practice because of the unknown XC energy functional $E_{XC}[n(\mathbf{r})]$. It is crucial to have an accurate XC energy functional $E_{XC}[n(\mathbf{r})]$ or potential $V_{XC}(\mathbf{r})$ to obtain a satisfactory description of a realistic condensed-matter system. The most widely used approximations for the XC potential are the local density approximation (LDA) and the generalized-gradient approximation (GGA) that will be described in the next section.
It is quite important to understand that the KS energy eigenvalues of the equation (2.3) are not for that of the original interacting many-body system and they do not have physical meaning, they cannot be interpreted as one-electron excitation energies of the interacting many-body system, i.e., they are not the energies to add or subtract from the interacting many-body system, because the total energy of the interacting system is not a sum of all the eigenvalues of occupied states in equation (2.3), i.e., $E_{tot} \neq \sum_i^{occ} \varepsilon_i$. Nevertheless, within the KS theory itself, the eigenvalues have a well-defined meaning and they are used to construct physically meaningful quantities.

2.4 The exchange-correlation functional

As mentioned in the previous section the KS equation can be solved if the exchange-correlation functional is known. Given the fact that an exact expression is not available, the introduction of an approximation is needed. Two such often used approximations are LDA and GGA.

2.4.1 Local density approximation

The local density approximation (LDA) [33–35] is the oldest approximation introduced in DFT. It defines the exchange-correlation functional as:

$$\begin{aligned} V_{LDA}[n(\mathbf{r})] &= \int n(\mathbf{r})\varepsilon_{XC}^{hom}[n(\mathbf{r})]\mathrm{d}\mathbf{r} \\ &= \int n(\mathbf{r})\left\{\varepsilon_{X}^{hom}[n(\mathbf{r})] + \varepsilon_{C}^{hom}[n(\mathbf{r})]\right\}\mathrm{d}\mathbf{r} \\ &= E_{X}^{hom}[n(\mathbf{r})] + E_{C}^{hom}[n(\mathbf{r})], \end{aligned} \tag{2.13}$$

for the spin unpolarised system and

$$V_{LSDA}[n_\uparrow(\mathbf{r}), n_\downarrow(\mathbf{r})] = \int n(\mathbf{r})\varepsilon_{XC}^{hom}[n_\uparrow(\mathbf{r}), n_\downarrow(\mathbf{r})]\mathrm{d}\mathbf{r}, \tag{2.14}$$

for the spin polarized case. Here $\varepsilon_{XC}^{hom}[n(\mathbf{r})]$ stands for the exchange-correlation function of the homogeneous electron gas with interacting electrons and is numerically known from Monte Carlo calculations. The underlying idea is very simple. At each point in space the exchange-correlation energy is approximated locally by the exchange-correlation energy of a homogeneous electron gas with the same electron density at that point. LDA is based on the local nature of exchange-correlation and the assumption that the density distribution does not vary too rapidly. In spite of its simplicity, LDA performs quite well even for more realistic systems.

2.4.2 Generalized gradient approximation

A more sophisticated approach is made with the generalized gradient approximation (GGA) [36–38]. While LDA only depends on the local density $n(\mathbf{r})$ itself, GGA also incorporates the density gradient:

$$V_{GGA}[n(\mathbf{r})] = \int n(\mathbf{r})\varepsilon_{XC}^{hom}[n(\mathbf{r}), |\nabla n(\mathbf{r}|]\mathrm{d}\mathbf{r}. \tag{2.15}$$

GGA usually performs better than LDA, but in the case of LDA a unique $\varepsilon_{XC}^{hom}[n(\mathbf{r})]$ is available. For GGA however, because the density gradient can be implemented in various ways, several versions exist. Moreover, many versions of GGA contain free parameters which have to be fitted to experimental data. GGA generally works better than LDA, in predicting bond length and binding energy of molecules, crystal lattice constants, and so on, especially in systems where the charge density is rapidly varying. However GGA sometimes overcorrects LDA results in ionic crystals where the lattice constants from LDA calculations fit well with experimental data but GGA will overestimate it. Nevertheless, both LDA and GGA perform badly in materials where the electrons tend to be localized and strongly correlated such as transition metal oxides and rare-earth elements and compounds. This drawback leads to approximations beyond LDA and GGA.

2.5 Solving the Kohn-Sham equations

Thanks to HK theorems and to the KS ansatz by solving the KS equations, that describe a system of independent-particles, the exact density and energy

of the ground state of a condensed matter system can be obtained. The KS equations must be solved self-consistently because the effective KS potential V_{KS} and the electron density $n(\mathbf{r})$ are closely related, i.e. $V_{XC}[n(\mathbf{r})]$. This solution can be found numerically through some self-consistent iterations. The process starts with an initial electron density, usually a superposition of atomic electron density, then the effective KS potential is calculated and the KS equation is solved with single-particle eigenvalues and wavefunctions, a new electron density is then calculated from the wavefunctions. Finally the self-consistent condition is checked, comparing the obtained charge density with the initial condition. If the two quantities differ by a value less than a certain threshold defined, then the self consistency has been reached, otherwise a new density has to be defined (usually this value is obtained by mixing the initial and the final electron density) and a new iteration will start with the new electron density. This process continues up to the the self-consistency. Having the electron density, various quantities can be calculated, for instance the total energy, forces, stress tensors, eigenvalues, the electron density of states, the band structure, etc..
The most time consuming step in the whole process is the solution of KS equation with a given KS potential. In order to obtain the final solution an important step is the expansion of the sigle-particle wavefunctions in a suitable basis set, $\{\phi_p\}$. Therefore

$$\psi_m = \sum_{p=1}^{P} c_{m,p}\, \phi_p. \tag{2.16}$$

In principle the basis set should be infinite, but in practice obviously it is finite and then the the function Ψ_m will not be described exactly and the choice of the limited basis set is fundamental to well describe Ψ_m. The problem will be then reduced to a solvable matrix problem, whose accuracy increases with the increase of P, the number of the eigenvalues and eigenfunctions.
Not only the number of the functions contained in the basis is important, but also the shape of these functions. A good basis has to be efficient and generally applicable, i.e. adapt to describe a lot of systems.
There are several different schemes to the calculation of the independent-particle electronic states in solids where boundary conditions are applied.

Plane waves

In this method, the wavefunctions are expanded in a complete set of plane waves, according to Bloch theorem eigenfunctions of a periodic hamiltonian can be expanded in a plane wave basis set. However in the proximity of nuclei the wavefunctions oscillate rapidly and too many functions in the basis are needed to describe this behavior and this method becomes very time consuming. Usually

this is used together with a pseudopotential approach for the external potential.The most widely used codes using plane waves and pseudopotentials are Quantum ESPRESSO [39], ABINIT [40] and VASP [41].

Localized atomic orbitals

This method provide a basis that captures the essence of the atomic-like features of solids and molecules. The most well-known methods in this category are linear combination of atomic orbitals (LCAO), also called tight-binding (TB) and full potential non-orthogonal local orbital (FPLO). The basic idea of these methods is to use atomic orbitals as the basis set to expand the one-electron wavefunction in KS equations.

Atomic sphere methods

These are the most general methods for precise solutions of KS equations. Generally speaking they are a combination of plane wave method and localized atomic orbitals, i.e. they use localized atomic orbital presentation near the nuclei and plane waves in the interstitial region. The most widely used methods are (full potential) linear muffin-tin orbital (LMTO) and (full potential) linear augment plane wave (LAPW) as implemented in WIEN2K and ELK.

In Figure 2.1 are summarized the possible choices for each specific part of the KS equation that can be made in order to obtain the appropriate solution.

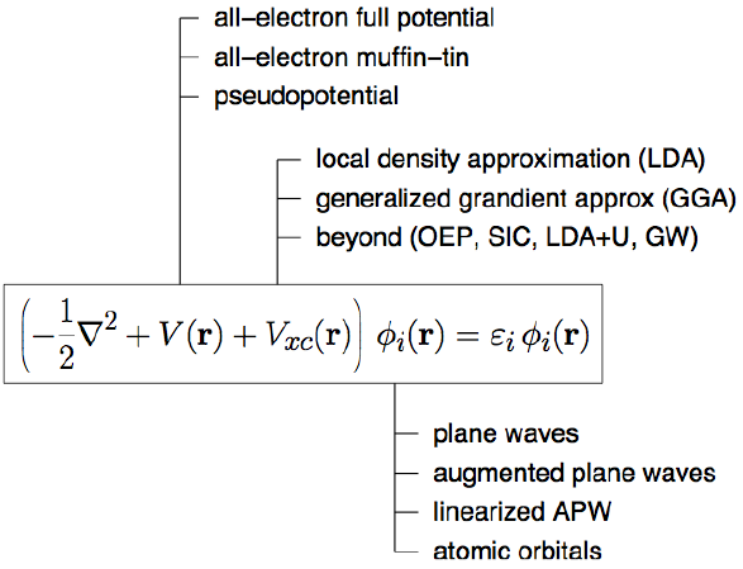

Figure 2.1: Possible choices of approximations to solve KS equation.

2.6 The Elk Code

The most used code for the calculations here under discussion is the ELK code [42]. This is an all-electron full-potential linearised augmented-plane wave (FP-LAPW) code for determining the properties of crystalline solids with many advanced features. Written originally at Karl-Franzens-Universität Graz as a milestone of the EXCITING EU Research and Training Network, the code is designed to be as simple as possible so that new developments in the field of DFT can be added quickly and reliably.

Elk uses atomic units. In this system $\hbar = 1$, the electron mass $m_e = 1$, the Bohr radius $a_0 = 1$ and the electron charge $e = 1$ (note that the electron charge is positive, so that the atomic numbers Z are negative). Thus, the atomic unit of length is 0.52917720859(36) Å, and the atomic unit of energy is the Hartree which equals 27.21138386(68) eV.

Chapter 3

Theoretical Background: The Superconducting State

The basic concepts of superconductivity are explained hereafter. A very brief introduction about the first microscopic theory, proposed by Bardeen, Cooper and Schrieffer will be given. This theory perfectly describes the so called conventional superconductors characterized by a weak coupling between electrons mediated by phonons. Then the more general Eliashberg theory will be described, that is suitable for unconventional superconductors. I will focus in particular on the generalization of this theory needed in order to describe the materials under investigation in this thesis.

"In all things of nature there is something of the marvelous."
Aristotele

3.1 Introduction

The first microscopic theory for superconductivity was proposed by Bardeen, Cooper and Schrieffer [43], and then called BCS theory, in 1957 almost 50 years after the discovery of Kamerlingh Onnes of the zero electric resistance of the mercury under 4.1 K. The theory of superconductivity can be divided into two separate conquests: first the establishment of a pairing formalism, which leads to a superconducting condensate, given some attractive particle-particle interaction, and secondly, a mechanism by which two electrons might attract one another. BCS [44], by simplifying the interaction, succeeded in establishing the pairing formalism. Indeed, one of the elegant outcomes of the BCS pairing formalism is the universality of various properties; at the same time this universality

means that the theory really does not distinguish one superconductor from another, and, more seriously, one mechanism from another. Luckily, while many superconductors do display universality, some do not, and these, as it turns out, provided very strong support for the electron-phonon mechanism. Before establishing a theory of superconductivity, one requires a satisfactory theory of the normal state [45]. In conventional superconductors, the Fermi liquid theory appears to work very well, so that, while we cannot solve the problem of electrons interacting through the Coulomb interaction, experiment tells us that Coulomb interactions give rise to well-defined quasiparticles, i.e. a set of excitations which are in one-to-one correspondence with those of the free-electron gas. The net result is that one begins the problem with a reduced Hamiltonian,

$$H_{red} = \sum_{\mathbf{k}\sigma} \varepsilon_{\mathbf{k}} c^{\dagger}_{\mathbf{k}\sigma} c_{\mathbf{k}\sigma} + \sum_{\mathbf{kk'}} V_{\mathbf{kk'}} c^{\dagger}_{\mathbf{k}\uparrow} c^{\dagger}_{\mathbf{-k}\downarrow} c_{\mathbf{-k'}\downarrow} c_{\mathbf{k'}\uparrow} \tag{3.1}$$

where, for example, the electron energy dispersion ε_k already contains much of the effect due to Coulomb interactions. The important point is that well-defined quasiparticles with a well defined energy dispersion near the Fermi surface are assumed to exist, and are summarized by the dispersion ε_k with a pairing interaction $V_{\mathbf{kk'}} \equiv V(\mathbf{k,k'})$. The BCS equation is

$$\Delta_{\mathbf{k}} = -\frac{1}{N(\mu)} \sum_{\mathbf{k'}} V_{\mathbf{k,k'}} \frac{\Delta_{\mathbf{k'}}}{2E_{\mathbf{k'}}} tanh \frac{E_{\mathbf{k'}}}{2T}, \tag{3.2}$$

where

$$_{\mathbf{k}} = \sqrt{(\varepsilon_{\mathbf{k}} - \mu)^2 + \Delta^2_{\mathbf{k}}} \tag{3.3}$$

is the quasiparticle energy in the superconducting state, $\Delta_{\mathbf{k}}$ is the variational parameter used by BCS, μ is the chemical potential and $N(\mu)$ is the normal density of states at the chemical potential (at the Fermi energy). An additional equation which must be considered along side the gap equation is the number equation,

$$n = 1 - \frac{1}{N(\mu)} \sum_{\mathbf{k'}} \frac{\varepsilon_{\mathbf{k}} - \mu}{E_{\mathbf{k'}}} tanh \frac{E_{\mathbf{k'}}}{2T}. \tag{3.4}$$

Given a pair potential and an electron density, one has to solve these equations to determine the variational parameter $\Delta_{\mathbf{k}}$ and the chemical potential μ generally with an iterative numerical method. For conventional superconductors the chemical potential hardly changes from the normal to the superconducting state, and the variational parameter is much smaller than the chemical potential, with the result that the second equation was usually ignored. BCS then modeled the pairing interaction as a negative (and therefore attractive) constant potential V with a sharp cutoff in momentum space (ω_D is the Debye energy):

$$V_{\mathbf{k,k'}} \approx -V\theta(\omega_D - \mid \varepsilon_{\mathbf{k}} - \mu \mid)\theta(\omega_D - \mid \varepsilon_{\mathbf{k'}} - \mu \mid). \tag{3.5}$$

Using this potential in the BCS equation, along with a constant density of states assumption over the entire range of integration,

$$\frac{1}{\lambda} = \int_0^{\omega_D} \frac{d\varepsilon}{E} tanh(E/2T) \tag{3.6}$$

where $\lambda = N(\mu)V$. At T = 0 K, the integral can be done analytically, leading to

$$\Delta = 2\omega_D \frac{exp(-1/\lambda)}{1 - exp(-1/\lambda)}. \tag{3.7}$$

Close to the critical temperature, T_c, the BCS equation becomes

$$\frac{1}{\lambda} = \int_0^{\omega_D/2T_c} \frac{tanhx}{x}\, dx \tag{3.8}$$

which cannot be solved in terms of elementary functions for arbitrary coupling strength. Nonetheless, in weak coupling regime, one obtains

$$T_c = 1.13\omega_D exp(-1/\lambda). \tag{3.9}$$

It is clear that T_c or the zero temperature variational parameter Δ depends on material properties such as the phonon spectrum ω_D, the electronic structure $N(\mu)$ and the electron-ion coupling strength V. However, it is possible to form various thermodynamic ratios, that turn out to be independent of material parameters. The obvious example from the preceding equations is the ratio $2\Delta/T_c$. In weak coupling (most relevant for conventional superconductors), for example,

$$\frac{2\Delta}{T_c} = 3.53, \tag{3.10}$$

that is a universal result, independent of the material involved. Many other such ratios can be determined within BCS theory, and the observed deviations from these universal values contributed to the need for an improved formulation of BCS theory.

In the '60s the first discrepancies between the experimental results and the theoretical predictions began to be observed and the BCS theory [44] turned out to be inadequate for superconductors in which the electron-phonon interaction is strong. The first reason of this unsuitableness is the instantaneous nature of the BCS interaction which does not incorporate enough of the physics of the electron-phonon system. For example, the electron-phonon interaction causes a mass enhancement of electron states near the Fermi level, as can be seen in specific heat, and a finite lifetime of electron quasiparticle states. In many material these effects are very strong and well-defined quasiparticles no longer exists. Nevertheless, Migdal [46] showed that Feynman-Dyson perturbation theory can

solve the electron-phonon problem to high accuracy, because the small parameter $\lambda\Omega_D/E_F \approx 10^{-3}$ keeps higher order corrections small.
Table 3.1 shows the values of the principal quantities for some characteristic elements. They differ more and more from the BCS predictions with the increase of coupling constant λ. According to the BCS theory, the expected values are $2\Delta/T_C = 3.53$ and $(C_s - C_n)/C_s = 1.43$. These deviations arise when the in-

	$2\Delta/T_c$	$(C_s - C_n)/C_s$	λ	T_C
Al	3.535	1.43	0.43	1.18
Sn	3.705	1.68	2.77	3.75
Pb	4.497	2.77	1.55	7.22
Hg	4.591	2.49	1.62	4.19

Table 3.1: Some deviations from the universality of many formulas of the BCS theory.

teraction between electron and phonon is strong, indeed, in the weak-coupling approximation the properties of the lattice and the dispersion of phonon curves do not enter directly into the BCS theory.
The prediction of superconducting properties such as the critical temperature or the superconducting energy gap remains one of the outstanding challenges in modern condensed matter theory. Owing to the complex nature of the superconducting state, a quantitative understanding of the pairing mechanism in superconductors requires a very detailed knowledge of the electronic structure, the phonon dispersions, and the interaction between electrons and phonons (bosons). For example the conventional superconductors below the critical temperature electron pairing results from a subtle interplay between the repulsive Coulomb interaction and the attractive electron-phonon interaction. Starting from the BCS theory several approaches to the calculation of the superconducting properties have been proposed including the first-principles Green's function methods such as is done in the Migdal-Eliashberg [47, 48] formalism that provides a very accurate description of the superconducting state in almost all superconductors. The electron-electron coupling provided by Eliashberg theory is local in space and retarded in time, reflecting the delay in the development of lattice overscreening. The result is in contrast with the non local, instantaneous nature of the BCS the model interaction, attractive for any pair of electrons both within ω_D (Debye energy) of the Fermi surface. Eliashberg theory is valid only when $\lambda\omega_D/E_F\,(\simeq\sqrt{m^*/M}) \ll 1$, where E_F is the Fermi level. This is the range of validity of the Migdal's theorem.
Migdal [46] argued that all the vertex corrections are $O(\sqrt{m^*/M})$ (where m^* is the electron effective mass and M is the ion mass) compared to the bare vertex, and therefore they can be ignored; this means that only single phonon scattering terms will contribute to the electronic self energy.

3.2 Imaginary-axis Eliashberg equations

3.2.1 The Nambu formalism

The Fröhlich interaction is formally very similar to the electron-electron interaction via Coulomb forces, thus the mutual scattering of two electrons can be explained through the electron-phonon-electron interaction in the same way. But the phase transition to the superconducting state invalidates the perturbation theory developed for a metal in the normal state. However, in 1960, Nambu showed how the formalism used in the normal state can be rewritten in such a way that the diagrams used to deal with the normal state are applicable also to the superconductive state [49]. The inclusion of Coulomb interactions causes the electron-phonon interaction to be screened and this can constitute a considerable reduction.
In spite of the strong electron-phonon coupling, it remains true that phonons corrections to the electron-phonon vertex are small. On the contrary, Coulombic corrections are not necessarily small, but are more or less constant factors, so they can be included in the coupling constant. In the Nambu formalism a 2-component spinor for the electron

$$\psi_{\mathbf{k}} = \begin{pmatrix} c_{\mathbf{k}\uparrow} \\ c^{\dagger}_{-\mathbf{k}\downarrow} \end{pmatrix}, \qquad \psi^{\dagger}_{\mathbf{k}} = \begin{pmatrix} c^{\dagger}_{\mathbf{k}\uparrow} & c_{-\mathbf{k}\downarrow} \end{pmatrix} \tag{3.11}$$

and a bare-phonon field operator

$$\varphi_{\mathbf{q}\nu} = b_{\mathbf{q}\nu} + b^{\dagger}{}_{-\mathbf{q}\nu} \tag{3.12}$$

are defined. The Hamiltonian of an electron-phonon interacting system can be written [45] in terms of ψ and φ, including Coulomb interactions and it becomes

$$\begin{aligned} H \;=\; & \sum_{\mathbf{k}} \varepsilon_{\mathbf{k}} \psi^{\dagger}_{\mathbf{k}} \sigma_3 \psi_{\mathbf{k}} + \sum_{\mathbf{q}\lambda} \Omega_{\mathbf{q}\lambda} b^{\dagger}{}_{\mathbf{q}\lambda} b_{\mathbf{q}\lambda} \sum_{\mathbf{k}\mathbf{k}'\lambda} g_{\mathbf{k}\mathbf{k}'\lambda} \varphi_{\mathbf{k}-\mathbf{k}'\lambda} \psi^{\dagger}_{\mathbf{k}'} \sigma_3 \psi_{\mathbf{k}} \\ & + \frac{1}{2} \sum_{\mathbf{k_1}\mathbf{k_2}\mathbf{k_3}\mathbf{k_4}} \langle \mathbf{k_3}\mathbf{k_4} | V_C | \mathbf{k_1}\mathbf{k_2} \rangle \left(\psi^{\dagger}_{\mathbf{k_3}} \sigma_3 \psi_{\mathbf{k_1}} \right) \left(\psi^{\dagger}_{\mathbf{k_4}} \sigma_3 \psi_{\mathbf{k_2}} \right), \end{aligned} \tag{3.13}$$

where $\varepsilon_{\mathbf{k}}$ is the one-electron Bloch energy relative to the Fermi energy E_F, σ_3 is a Pauli matrix[1], Ω is the bare phonon energy of wavevector $\mathbf{q}$ and mode ν, $g_{\mathbf{k}\mathbf{k}'\nu}$ are electron phonon matrix element and V_C is the coulomb potential.
Translational invariance of V_C restrict $\mathbf{k_1} + \mathbf{k_2} - \mathbf{k_3} - \mathbf{k_4}$ to be either zero or a reciprocal lattice vector $\mathbf{K}$. The electrons are described in an extended zone

[1] The Pauli matrices are

$$\sigma_1 = \begin{pmatrix} 0 & 1 \\ 1 & 0 \end{pmatrix}, \quad \sigma_2 = \begin{pmatrix} 0 & -i \\ i & 0 \end{pmatrix}, \quad \sigma_3 = \begin{pmatrix} 1 & 0 \\ 0 & -1 \end{pmatrix}$$

scheme and the phonons are described in a reduced zone scheme which is extended periodically throughout **q**-space. In order to apply perturbation methods to superconductors the possibility of the existence of Cooper pairs has to be included. This can be done taking the anomalous propagators. Thanks to the new formalism, the Green function [50] becomes

$$\widehat{G}(\mathbf{k}\,\tau) = -\langle T\{\psi_{\mathbf{k}}(\tau)\psi^{\dagger}_{\mathbf{k}}(0)\}\rangle, \tag{3.14}$$

$$D_{\lambda}(\mathbf{q}\tau) = -\langle T\{\varphi_{\mathbf{q}\lambda}(\tau)\varphi^{\dagger}_{\mathbf{k}}(0)\}\rangle \tag{3.15}$$

where the average is over the grand canonical ensemble ($\beta = 1/T$, here T is the temperature)

$$\langle Q\rangle = \frac{Tr\; e^{-\beta H}Q}{Tr\; e^{-\beta H}}, \tag{3.16}$$

where the operators develop with imaginary time and T represents the usual time-ordered product. As the matrix operator $\psi_{\mathbf{k}}(\tau)\psi^{\dagger}_{\mathbf{k}}(0)$ does not conserve the number of particles the definition of a new operator U that adjusts the number of particles is necessary:

$$U = 1 + R^{\dagger} + R, \tag{3.17}$$

where R converts a given state in an N-particle system into the corresponding state in the $N+2$ particle system.
By this definition, the Green function for electrons is a 2×2 matrix, the diagonal elements are the conventional Green functions for spin-up electrons and spin-down holes, while G_{12} and G_{21} describe the pairing properties. It is defined as

$$\widehat{G}(\mathbf{k},\tau) = -\begin{pmatrix} \langle T\{c_{\mathbf{k}\uparrow}(\tau)c^{\dagger}_{\mathbf{k}\uparrow}(0)\}\rangle & \langle UT\{c_{\mathbf{k}\uparrow}(\tau)c_{-\mathbf{k}\downarrow}(0)\}\rangle \\ \langle UT\{c^{\dagger}_{-\mathbf{k}\downarrow}(\tau)c^{\dagger}_{\mathbf{k}\uparrow}(0)\}\rangle & \langle T\{c^{\dagger}_{-\mathbf{k}\downarrow}(\tau)c_{-\mathbf{k}\downarrow}(0)\}\rangle \end{pmatrix}. \tag{3.18}$$

The diagonal elements are the 'normal' propagators, while the off-diagonals elements are Gor'kov's F and $\bar{F}$, respectively.
The phonon and electron Green Function could be expanded in a Fourier series

$$D_{\lambda}(\mathbf{q},\,\tau) = \frac{1}{\beta}\sum_{n=-\infty}^{\infty} e^{-i\nu_n\tau}D_{\lambda}(\mathbf{q},\,i\nu_n) \tag{3.19}$$

$$G(\mathbf{k},\,\tau) = \frac{1}{\beta}\sum_{n=-\infty}^{\infty} e^{-i\omega_n\tau}G(\mathbf{k},\,i\omega_n), \tag{3.20}$$

where

$$\nu_n = 2n\pi/\beta, \qquad \omega_n = (2n+1)\pi/\beta \tag{3.21}$$

where ν_n and ω_n are the Matzubara frequencies and n is an integer. The Matzubara frequencies are odd multiples of π/β for fermions while for bosons

they are even.

3.2.2 The Migdal-Eliashberg Theory

The basic components of a many-body system are the propagators and the Migdal-Eliashberg theory [51–57] is not an exception. The one-electron Green function for the non-interacting system (in momentum and imaginary frequencies space) is given by

$$\widehat{G}_0(\mathbf{k}, i\omega_n) = \left[i\omega_n \mathbb{1} - \varepsilon_{\mathbf{k}}\sigma_3\right]^{-1} \tag{3.22}$$

and for phonons

$$D_0(\mathbf{q}, i\nu_n) = \left[M\left[\omega^2(\mathbf{q}) + \nu^2{}_n\right]\right]^{-1} \tag{3.23}$$

where M is the ion mass and $\omega(\mathbf{q})$ is the phonon dispersion.
From a diagrammatic analysis a Dyson-like equation for the electron and phonon Green functions can be written, though now the electron one will be a 2×2 matrix equation.

$$[\widehat{G}(\mathbf{k},\, i\omega_n)]^{-1} = [\widehat{G}_0(\mathbf{k},\, i\omega_n)]^{-1} - \widehat{\Sigma}(\mathbf{k},\, i\omega_n), \tag{3.24}$$

$$[D(\mathbf{q},\, i\nu_n)]^{-1} = [D_0(\mathbf{q}, i\nu_n) - \Pi(\mathbf{q}, i\nu_n)]^{-1} \tag{3.25}$$

where Σ is the electronic self-energy and Π the bosonic one. In principle, in these self-energies, there are also vertex corrections. Migdal's approximation (see Figure 3.1) was to set the vertex values equal to the bare vertex, then the electron-phonon interaction is truncated at order $\sqrt{m/M} \sim \omega_D/E_F$.
By using the Hamiltonian reported in (3.13), the Coulomb interaction can be included and the discussion generalized to a temperature different from zero (Eliashberg wrote his equations at $T = 0$), obtaining

$$\begin{aligned}\widehat{\Sigma}(\mathbf{k},\, i\omega_n) = & -\frac{1}{\beta}\sum_{\mathbf{k}',n'} \sigma_3 G(\mathbf{k}',\, i\omega_{n'})\sigma_3 \\ & \times\left[\sum_{\nu}\left|g_{\mathbf{k},\mathbf{k}',\nu}\right|^2 D_\nu(\mathbf{k}-\mathbf{k}', i\omega_n - i\omega_{n'}) + V_C(\mathbf{k}-\mathbf{k}')\right],\end{aligned} \tag{3.26}$$

where $V_C(\mathbf{k}-\mathbf{k}')$ is the screened Coulomb potential which has been taken to depend only on the momentum transfer $\mathbf{k}-\mathbf{k}'$.
It is important to note that this equation actually represents four coupled equations, one for each component of the matrix Σ. This equation can be rewritten by using a linear combination of the Pauli matrices

$$\begin{aligned}\widehat{\Sigma}(\mathbf{k},\, i\omega_n) = & \; i\omega_n\left[1 - Z(\mathbf{k},\, i\omega_n)\right]\mathbb{1} + \chi(\mathbf{k},\, i\omega_n)\sigma_3 \\ & + \phi(\mathbf{k},\, i\omega_n)\sigma_1 + \bar{\phi}(\mathbf{k},\, i\omega_n)\sigma_2.\end{aligned} \tag{3.27}$$

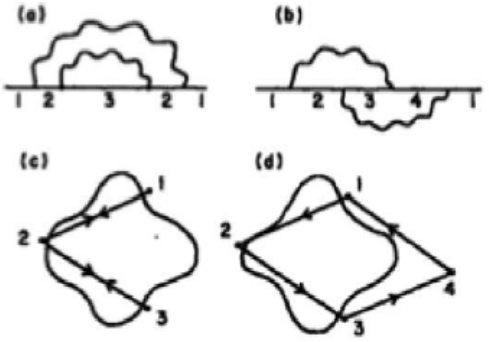

Figure 3.1: Feynman graph (a) and (b) are the next-order correction to the propagator. Graph (a) is included in Migdal's theory and graph (b) is the first term omitted. In (c) and (d) are shown schematic Fermi surfaces and particular k-states which contribute to (a) and (b) respectively. The last term, in general, will involve large energy denominators (as 3-4 and 1-4) so this results negligible. This theorem may fail in two special cases: first, if either phonon has $|\mathbf{q}|$ small, and second, if the Fermi surface has a one-dimensional topology.

By using the Dyson equation the Green function become

$$\left[\widehat{G}(\mathbf{k},\, i\omega_n)\right]^{-1} = i\omega_n Z\mathbb{1} - (\varepsilon_{\mathbf{k}} + \chi)\,\sigma_3 - \phi\sigma_1 - \bar{\phi}\sigma_2. \tag{3.28}$$

Now, the equation of the self energy (3.27) should be solved by using the Green functions (3.28). The solution with $\phi = \bar{\phi} = 0$ always exists and correspond to the normal state. However, a solution with non-zero ϕ or $\bar{\phi}$, if it exists, has a lower free energy and describes a state with Cooper-pairs condensation.
Now, the matrix inversion has to be applied

$$\begin{aligned}\widehat{G}(\mathbf{k},\, i\omega_n) &= \frac{1}{\Theta}\left[i\omega_n Z\mathbb{1} + (\varepsilon_{\mathbf{k}} + \chi)\,\sigma_3 + \phi\sigma_1 + \bar{\phi}\sigma_2\right] \\ &= \frac{1}{\Theta}\begin{pmatrix} i\omega_n Z + (\varepsilon_{\mathbf{k}} - \mu + \chi) & \phi - i\bar{\phi} \\ \phi + i\bar{\phi} & i\omega_n Z - (\varepsilon_{\mathbf{k}} - \mu + \chi) \end{pmatrix}\end{aligned} \tag{3.29}$$

where

$$\Theta = (i\omega_n Z)^2 - (\varepsilon_{\mathbf{k}} - \mu + \chi)^2 - \phi^2 - \bar{\phi}^2. \tag{3.30}$$

Eliashberg theory is valid also in the normal state [51], where $\widehat{G}$ is diagonal; therefore, in that case, ϕ and $\bar{\phi}$ must vanish and Z and χ must be determined by the normal-state self-energy; it is clear from the above equation that χ shifts the electronic energies and Z is a renormalizazion function. Actually, it can be shown that, if in the Hamiltonian there are no terms describing spin-dependent interactions, ϕ and $\bar{\phi}$ satisfy identical nonlinear equations hence the solution will have $\phi = \bar{\phi}$, except for a proportionality factor.[2]
Now, looking at the Green function, it appears clear that the poles, the electrons

[2]The arbitrary phase comes from the one of the one-electron state. Normally, the physical quantities cannot depend on this phase. However, it is measured by Josephson tunnelling. Thus BCS theory exhibits a broken gauge symmetry.

(and holes) elementary excitation are given by

$$E_{\mathbf{k}} = \sqrt{\left(\frac{\varepsilon_{\mathbf{k}} - \mu + \chi}{Z}\right)^2 + \left(\frac{\phi + \bar{\phi}}{Z}\right)^2}; \tag{3.31}$$

and then the gap function is given by

$$\Delta(\mathbf{k}, i\omega_n) = \frac{\phi - i\bar{\phi}}{Z}. \tag{3.32}$$

Now, inserting the Green function into the self-energy and comparing the result with the general expression a set of equations for Z, χ, ϕ and $\bar{\phi}$ is obtained:

$$\begin{aligned}
[1 - Z(\mathbf{k}, i\omega_n)]\, i\omega_n &= \frac{1}{\beta} \sum_{\mathbf{k}',n',\nu} \left|g_{\mathbf{k},\mathbf{k}',\nu}\right|^2 \frac{i\omega_{n'} Z(\mathbf{k}', i\omega_{n'}) D_\nu(\mathbf{k} - \mathbf{k}', i\omega_n - i\omega_{n'})}{\Theta(\mathbf{k}', i\omega_{n'})} \\
\chi(\mathbf{k}, i\omega_n) &= \frac{1}{\beta} \sum_{\mathbf{k}',n',\nu} \left|g_{\mathbf{k},\mathbf{k}',\nu}\right|^2 \frac{\chi(\mathbf{k}', i\omega_{n'}) + \varepsilon_{\mathbf{k}'}}{\Theta(\mathbf{k}', i\omega_{n'})} D_\nu(\mathbf{k} - \mathbf{k}', i\omega_n - i\omega_{n'}) \\
\phi(\mathbf{k}, i\omega_n) &= -\frac{1}{\beta} \sum_{\mathbf{k}',n',\nu} [\left|g_{\mathbf{k},\mathbf{k}',\nu}\right|^2 D_\nu(\mathbf{k} - \mathbf{k}', i\omega_n - i\omega_{n'}) - V_C(\mathbf{k} - \mathbf{k}')] \frac{\phi(\mathbf{k}', i\omega_{n'})}{\Theta(\mathbf{k}', i\omega_{n'})} \\
\bar{\phi}(\mathbf{k}, i\omega_n) &= -\frac{1}{\beta} \sum_{\mathbf{k}',n',\nu} [\left|g_{\mathbf{k},\mathbf{k}',\nu}\right|^2 D_\nu(\mathbf{k} - \mathbf{k}', i\omega_n - i\omega_{n'}) - V_C(\mathbf{k} - \mathbf{k}')] \frac{\bar{\phi}(\mathbf{k}', i\omega_{n'})}{\Theta(\mathbf{k}', i\omega_{n'})} \\
n &= 1 - \frac{2}{\beta} \sum_{\mathbf{k}',n'} \frac{\chi(\mathbf{k}', i\omega_{n'}) + \varepsilon_{\mathbf{k}'} - \mu}{\Theta(\mathbf{k}', i\omega_{n'})}
\end{aligned} \tag{3.33}$$

where the last row represents the electron number equation and determines the chemical potential μ. These are the *Eliashberg equations*. Usually, these equations are averaged over energy isosurface in $\mathbf{k}$-space and solved in one dimension. This approximation turns out to be good for elemental superconductors, but fails in describing more complex systems. Now, the arbitrary phase of ϕ, $\bar{\phi}$ can be fixed, then $\bar{\phi} = 0$. The $\mathbf{k}$-dependence in $\widehat{G}$ comes mainly from the explicit $\varepsilon_{\mathbf{k}}$ dependence of Θ, while can be averaged out in Z and ϕ (fixing $\varepsilon_{\mathbf{k}} = E_F$ because these quantities are non zero only near the Fermi surface), so:

$$\begin{aligned}
Z(\mathbf{k}, i\omega_n) &\rightarrow \langle Z(\mathbf{k}, i\omega_n)\rangle_{\varepsilon = E_F} = Z(i\omega_n) \\
\phi(\mathbf{k}, i\omega_n) &\rightarrow \langle \phi(\mathbf{k}, i\omega_n)\rangle_{\varepsilon = E_F} = \phi(i\omega_n) \\
\chi(\mathbf{k}, i\omega_n) &\rightarrow \langle \chi(\mathbf{k}, i\omega_n)\rangle_{\varepsilon = E_F} = \chi(i\omega_n)
\end{aligned} \tag{3.34}$$

The same $\mathbf{k}$ average in the right hand side of the Eliashberg equation can be done applying an operator $\frac{1}{N(0)} \sum_k \delta(\varepsilon_{\mathbf{k}})$ where $N(0)$ is the normal density of state at the Fermi level and introducing a unity factor $\int d\omega\, \delta(\omega - \omega_{\mathbf{q},\nu})$, where

$\mathbf{q} = \mathbf{k} - \mathbf{k}'$ is the phonon wavevector, and then [3]:

$$
\begin{aligned}
[1 - Z(i\omega_n)]\, i\omega_n &= -\frac{1}{\beta N^2(0)} \sum_{n'} \int d\omega \sum_{\mathbf{k},\nu} \sum_{\mathbf{k}'} \frac{\left|g_{\mathbf{k},\mathbf{k}',\nu}\right|^2 \delta(\varepsilon_{\mathbf{k}'})\delta(\varepsilon_{\mathbf{k}})\delta(\omega - \omega_{\mathbf{q},\nu}) 2\omega_{\mathbf{q},\nu}}{(\omega_n - \omega_{n'})^2 + \omega^2_{\mathbf{q},\nu}} \\
&\quad \times \int_{-\infty}^{\infty} d\varepsilon \frac{N(\varepsilon) i\omega_{n'} Z(i\omega_{n'})}{\Theta(\varepsilon, i\omega_{n'})} \\
\phi(i\omega_n) &= \frac{1}{\beta N^2(0)} \sum_{n'} \int d\omega \sum_{\mathbf{k},\nu} \sum_{\mathbf{k}'} \frac{\left|g_{\mathbf{k},\mathbf{k}',\nu}\right|^2 \delta(\varepsilon_{\mathbf{k}'})\delta(\varepsilon_{\mathbf{k}})\delta(\omega - \omega_{\mathbf{q},\nu}) 2\omega_{\mathbf{q},\nu}}{(\omega_n - \omega_{n'})^2 + \omega^2_{\mathbf{q},\nu}} \\
&\quad \times \int_{-\infty}^{\infty} d\varepsilon \frac{N(\varepsilon) \phi(i\omega_{n'})}{\Theta(\varepsilon, i\omega_{n'})} \\
\chi(i\omega_n) &= -\frac{1}{\beta N^2(0)} \sum_{n'} \int d\omega \sum_{\mathbf{k},\nu} \sum_{\mathbf{k}'} \frac{\left|g_{\mathbf{k},\mathbf{k}',\nu}\right|^2 \delta(\varepsilon_{\mathbf{k}'})\delta(\varepsilon_{\mathbf{k}})\delta(\omega - \omega_{\mathbf{q},\nu}) 2\omega_{\mathbf{q},\nu}}{(\omega_n - \omega_{n'})^2 + \omega^2_{\mathbf{q},\nu}} \\
&\quad \times \int_{-\infty}^{\infty} d\varepsilon \frac{N(\varepsilon) \left[\varepsilon - \mu + \chi(i\omega_{n'})\right]}{\Theta(\varepsilon, i\omega_{n'})} \\
n &= 1 - \frac{2}{\beta N(0)} \sum_{n'} \int_{-\infty}^{\infty} d\varepsilon \frac{N(\varepsilon) \left[\varepsilon - \mu + \chi(i\omega_{n'})\right]}{\Theta(\varepsilon, i\omega_{n'})},
\end{aligned}
\tag{3.35}
$$

as the phonon interaction is very low, the sum over $\mathbf{k}'$ has been splitted up into an angular average for $\varepsilon_{\mathbf{k}} = E_F$ and an integration in ε on the ε dependence of the electronic Green function. Only the states near the Fermi level will concur to this integral, because of the $\varepsilon_{\mathbf{k}}$ terms in $\Theta(\varepsilon, i\omega_n)$, then, if the density of state can be considered constant in this region, a further simplification can be introduced using $N(\varepsilon = \mu) = N(0)$ instead of $N(\varepsilon)$ and integrate analytically: in this way the final result is $\chi(i\omega_n) = 0$ and $n = 1$ (half filling approximation).
At this point is useful to define the electron-boson spectral function, that is always a positive-definite function,

$$
\alpha^2 F(\omega) = N(0) \sum_{\mathbf{q},\nu} g^2_{\mathbf{q},\nu} \delta(\omega - \omega_{\mathbf{q},\nu}) \tag{3.36}
$$

$$
= \frac{1}{N(0)} \sum_{\mathbf{k},\mathbf{k}'} \sum_{\nu} \left|g_{\mathbf{k},\mathbf{k}',\nu}\right|^2 \delta(\varepsilon_{\mathbf{k}'})\delta(\varepsilon_{\mathbf{k}})\delta(\omega - \omega_{\mathbf{q},\nu}), \tag{3.37}
$$

where

$$
g^2_{\mathbf{q},\nu} = \frac{1}{N^2(0)} \sum_{\mathbf{k}'} \left|g_{\mathbf{k},\mathbf{k}',\nu}\right|^2 \delta(\varepsilon_{\mathbf{k}+\mathbf{q}})\delta(\varepsilon_{\mathbf{k}}) \tag{3.38}
$$

[3] the equation for χ will be omitted from now on because, in many cases, its contribution can be neglected.

is the electron-phonon coupling which is **q**-depending. Then the Eliashberg system takes the form:

$$[1 - Z(i\omega_n)]\, i\omega_n = -\frac{\pi}{\beta}\sum_{\omega_{n'}} \frac{Z(i\omega_{n'})i\omega_{n'}}{\Xi(i\omega_{n'})} \int d\omega \frac{2\omega\alpha^2 F(\omega)}{(\omega_n - \omega_{n'})^2 + \omega^2} \tag{3.39}$$

$$\phi(i\omega_n) = \frac{\pi}{\beta}\sum_{\omega_{n'}} \frac{\phi(i\omega_{n'})}{\Xi(i\omega_{n'})}[\int d\omega \frac{2\omega\alpha^2 F(\omega)}{(\omega_n - \omega_{n'})^2 + \omega^2} - N(0)V_{col}] \tag{3.40}$$

$$\Xi(i\omega_n) = \sqrt{[Z(i\omega_n)\omega_n]^2 + [\phi(i\omega_n)]^2} \tag{3.41}$$

where V_{col} represents an appropriate Fermi surface average of the quantity V_C. The sum over Matsubara's frequencies can be cut off at an energy ω_C.
Solving these equations, it is possible to obtain the electron self energy at the Fermi level.

3.2.3 The Coulomb pseudopotential

The point to clarify is how the large Coulomb effects [56] can be replaced by a simple number $\mu^* \sim 0.1$.
Including the repulsive term in the Eliashberg equations is a hard task. The Coulomb interaction cannot be introduced with the same accuracy of the electron-phonon one, since it does not have a natural cut-off to ensure a convergent sum on the Matsubara's frequencies.
The electron-electron interaction has a large energy scale (and then a narrow interaction time) with respect to electron-phonon attraction. The electron-phonon interaction has a timescale typical of the much larger inverse phonon frequencies. The time scale difference is normally dealt using an energy window ω_C with a renormalized electron-electron interaction

$$\mu^* = \frac{\mu}{1 + \mu \ln(E_F/\omega_C)}, \tag{3.42}$$

which is called *Morel-Anderson pseudopotential*. In this formula, μ is an average electron-electron matrix element times the density of states at the Fermi level.
In the normal state self-energy the Coulomb potential is included, therefore only the off-diagonal term will be affected by this correction and the result is

$$\phi_{Coul}(i\omega_n) = -\mu^* \frac{\pi}{\beta}\sum_{\omega_{n'}} \frac{\phi(i\omega_{n'})}{\Xi(i\omega_{n'})}\theta(\omega_C - |\omega_{n'}|). \tag{3.43}$$

Including this contribution in the Eliashberg equation for ϕ, it becomes

$$\begin{aligned}\Delta(i\omega_n)Z(i\omega_n) &= \frac{\pi}{\beta}\sum_{\omega_{n'}}\frac{\Delta(i\omega_{n'})}{\sqrt{{\omega^2}_{n'}+\Delta^2(i\omega_n)}}\left[\lambda(i\omega_{n'}-i\omega_n)-\mu^*(\omega_C)\right]\theta(\omega_C-|\omega_{n'}|)\\ Z(i\omega_n) &= 1+\frac{\pi}{\omega_n\beta}\sum_{\omega_{n'}}\frac{\omega_{n'}}{\sqrt{{\omega^2}_{n'}+\Delta^2(i\omega_n)}}\lambda(i\omega_{n'}-i\omega_n)\end{aligned} \tag{3.44}$$

where $\lambda(i\omega_{n'}-i\omega_n)$ is a function related to the electron-boson spectral density $\alpha^2F(\omega)$ through the relation

$$\lambda(i\omega_n-i\omega_n)=2\int_0^\infty\frac{\Omega\alpha^2F(\Omega)d\Omega}{\Omega^2+(\omega_{n'}-\omega_n)^2}. \tag{3.45}$$

3.3 Real-axis Eliashberg equations

The Green function can be analytically continued onto the real-frequencies axis, by using the expression $\omega+i\delta$, where δ is an infinitesimal quantity.
The density of state is contained in the imaginary part of $G(\mathbf{k},\omega+i\delta)$.
In their real-axis formulation, Eliashberg equations are a set of two non-linear integral equations for a complex frequency-dependent gap $\Delta(\omega)$ and renormalization function $Z(\omega)$, which exists also in the normal state. Both $\Delta(\omega)$ and $Z(\omega)$ are temperature dependent.

$$\begin{aligned}\Delta(\omega,T)Z(\omega,T) &= \int_0^{\omega_C}d\omega'\,\Re\left[\frac{\Delta(\omega',T)}{\sqrt{\omega'^2-\Delta^2(\omega',T)}}\right]\int_0^\infty d\Omega\alpha^2F(\Omega)\\ &\times\left\{\left[n(\Omega)+f(-\omega')\right]\left[\frac{1}{\omega+\omega'+\Omega+i\delta^+}-\frac{1}{\omega-\omega'-\Omega+i\delta^+}\right]\right.\\ &\left.-\left[n(\Omega)+f(\omega')\right]\left[\frac{1}{\omega-\omega'+\Omega+i\delta^+}-\frac{1}{\omega+\omega'-\Omega+i\delta^+}\right]\right\}\\ &-\mu^*\int_0^{\omega_C}d\omega'\Re\left[\frac{\Delta(\omega',T)}{\sqrt{\omega'^2-\Delta^2(\omega',T)}}\right]\left[1-2f(\omega')\right],\end{aligned} \tag{3.46}$$

$$\begin{aligned}\left[1-Z(\omega,T)\right]\omega &= \int_0^\infty d\omega'\,\Re\left[\frac{\omega'}{\sqrt{\omega'^2-\Delta^2(\omega',T)}}\right]\int_0^\infty d\Omega\alpha^2F(\Omega)\\ &\times\left\{\left[n(\Omega)+f(-\omega')\right]\left[\frac{1}{\omega+\omega'+\Omega+i\delta^+}-\frac{1}{\omega-\omega'-\Omega+i\delta^+}\right]\right.\\ &\left.-\left[n(\Omega)+f(\omega')\right]\left[\frac{1}{\omega-\omega'+\Omega+i\delta^+}-\frac{1}{\omega+\omega'-\Omega+i\delta^+}\right]\right\}.\end{aligned} \tag{3.47}$$

Here, ω_C is the boson energy cut-off introduced into the Coulomb repulsion term in order to assure the convergence in (3.46), $f(\omega)=1/(e^{\beta\omega}+1)$ is the Fermi function and $n(\Omega)=1/(e^{\beta\Omega}-1)$ is the Bose function. The real part of the product $\Delta(\omega,T)Z(\omega,T)$ and of $Z(\omega,T)$ is determined by the principal-value integrals (3.46) and (3.47), while the imaginary part comes from the delta-function parts.

The denominators can vanish for particular energies, then the integrals in (3.46) and (3.47) must be done carefully when a numerical approach is used. The low frequency behaviour of the various functions is, at $T = 0$, $\Re[\Delta(\omega)] = c$, $\Im[\Delta(\omega)] = 0$, $\Re[Z(\omega)] = d$ and $\Im[Z(\omega)] = 0$ while, at $T \neq 0$, $\Re[\Delta(\omega)] \propto \omega^2$, $\Im[\Delta(\omega)] \propto \omega$, $\Re[Z(\omega)] = d(T)$ and $\Im[Z(\omega)] \propto 1/\omega$ where c and d are constants.

3.4 Simplified approaches

3.4.1 BCS limit

In order to better understand these equations, it can be useful to reduce them to BCS limit. To achieve this aim further approximations are introduced. First of all, in the most rough case, all the bosons factor in the real-axis Eliashberg equations can be ignored, i.e., real bosons scattering are not taken into account. Further, the imaginary parts of Δ and Z must be neglected and one can set $\Delta(\omega, T) = \Delta_0(T)$ for $\omega < \omega_D$ and $\Delta(\omega, T) = 0$ for $\omega \geq \omega_D$ where $\Delta_0(T)$ is a real number and ω_D is the Deybe energy. And $Z(\omega, T)$ can be replaced by its value in the normal state at $\omega = 0$ and $T = 0$, then

$$Z(0,T) - 1 = 2\int_0^\infty d\omega' \int_0^\infty d\Omega\, \alpha^2 F(\Omega) \left[\frac{f(-\omega')}{(\omega' + \Omega)^2} + \frac{f(\omega')}{(\omega' + \Omega)^2}\right] \equiv \lambda(T) \quad (3.48)$$

and, in the $T \to 0$ limit it becomes

$$Z(0,0) - 1 = \int_0^\infty d\Omega\, \alpha^2 F(\Omega) \int_0^\infty \frac{2d\omega'}{(\omega' + \Omega)^2} \equiv \lambda. \quad (3.49)$$

The gap equation becomes

$$\Delta_0(T) = \int_{\Delta_0(T)}^{\omega_D} d\omega' \frac{\Delta_0(T)}{\sqrt{\omega'^2 - {\Delta^2}_0(T)}} \frac{\lambda - \mu^*}{1 + \lambda} \Big[1 - 2f(\omega')\Big]. \quad (3.50)$$

It is interesting to note that now ω_D is important for both λ and μ^* contribution. If one consider $\varepsilon = \sqrt{\omega'^2 - {\Delta^2}_0}$, the equation can be rewritten as

$$\Delta_0(T) = \frac{\lambda - \mu^*}{1 + \lambda} \int_0^{\omega_D} d\varepsilon \frac{\Delta_0(T)}{\sqrt{\varepsilon^2 + {\Delta^2}_0(T)}} \left[1 - 2f\left(\sqrt{\varepsilon^2 + {\Delta^2}_0(T)}\right)\right], \quad (3.51)$$

which is the usual BCS equation at finite temperature. In the the $T \to 0$ limit

$$\Delta_0 = \frac{\lambda - \mu^*}{1 + \lambda} \int_0^{\omega_C} d\varepsilon \frac{\Delta_0}{\sqrt{\varepsilon^2 + {\Delta^2}_0}}\,, \quad (3.52)$$

which correspond to the BCS gap equation if a new coupling constant is defined, $\lambda_{BCS} = (\lambda - \mu^*)/(1 + \lambda)$.

The renormalization factor $1/(1+\lambda)$ comes from the Z term in the Eliashberg equation, i.e. from having included electron-phonon effect. In general the Eliashberg equations are solved numerically with iterative method until you reach convergence. The numerical procedure is very simple in the formulation on imaginary axis, much less in the real one. The critical temperature can be calculated by solving an eigenvalue equation [51] or, more easily, by giving a very small test value to superconducting gap (for the Pb it is $\Delta = 1.4$ meV at $T = 0$ K so, for example, $\Delta(T) = 10^{-7}$ meV) and looking for the temperature at which the solution converges. In this way, a precision in the T_c value is obtained that is much higher than the experimental verification.

3.4.2 The critical temperature's equations

Solving the Eliashberg system, even in the isotropic form, is a quite demanding task. However the most relevant results can be obtained with a simpler approach, that was proposed by Mc Millan [58]. Trough a fit of a large set of results obtained considering the spectral function of lead and solving the Eliashberg equations in a small range of the parameters ($\lambda < 2$ and $\mu^* < 0.15$), Mc Millan obtained an analytic formula for the critical temperature:

$$T_C = \frac{\Theta_D}{1.45} \exp\left[-\frac{1.04\,(1+\lambda)}{\lambda - \mu^*\,(1+0.62\lambda)}\right], \tag{3.53}$$

where Θ_D is the Debye temperature and the number λ appearing in this formula has the same meaning as the electron-phonon coupling parameter, and can be derived from the Eliashberg function as

$$\lambda = 2\int d\Omega \frac{\alpha^2 F(\Omega)}{\Omega}. \tag{3.54}$$

Later, this formula has been refined by Allen and Dynes [58] and the factor $\Theta_D/1.45$ has been substituted with $\Omega_{log}/1.2$, which uses a much more representative frequency:

$$\Omega_{log} = \exp\left[\frac{2}{\lambda}\int d\Omega \log\Omega\, \frac{\alpha^2 F(\Omega)}{\Omega}\right], \tag{3.55}$$

which is a weighted average of the phonon frequencies. The Mc Millan formula predicts an upper limit for T_C even if λ increases indefinitely. However this was a wrong conclusion because the equation (3.53) was not derived analytically but obtained by numerical solutions in a fixed range of the coupling constant and then it is not possible to consider the limit for $\lambda \to \infty$. For $\lambda \gg 1$, taking the limit of the Eliashberg equations the following expression for T_C can be obtained in an analytical way

$$T_C = 0.183\omega_D\sqrt{\lambda} \tag{3.56}$$

and it is clear that in Eliashberg theory does not exist an upper limit for the critical temperature.

3.5 Relation between the real- and the imaginary-axis formulation

3.5.1 Padé approximants method

Eliashberg equations on the real axis are very difficult to solve but in their formulation on the imaginary axis can be used almost only to evaluate the critical temperature.
Therefore, a procedure which allows obtaining the real-axis gap and the renormalization function by analytically continuing $\Delta(i\omega_n)$ and $Z(i\omega_n)$ is used [59, 60]. This procedure makes use of Padé approximants.
This allow to speed up the numerical solution of Eliashberg equations. However the Padé method is valid only at $T < T_C/10$, thus it is often necessary to solve for $\Delta(\omega)$ directly from the real-frequency equations. Also when in the Eliashberg equations exist some terms that describe the presence of impurities in the superconductor the accuracy of the Padé approximants can be not so good.
The N-point Padé approximant to a complex function $u(z)$ of the complex variable z, whose N values u_i (i = 1, ..., N) are given at N complex points z_i, is defined as a continued fraction:

$$C_N(z) = \cfrac{a_1}{1 + \cfrac{a_2(z-z_1)}{1+\cfrac{a_3(z-z_2)}{\vdots \cfrac{}{1+\ a_n(z-z_{n-1})}}}} \tag{3.57}$$

such that

$$C_N(z_i) = u_i, \quad i = 1, ..., N. \tag{3.58}$$

The coefficients a_i are given by recursive formula
$a_i = g_i(z_i)$, $g_1(z_i) = u_i$ with $i = 1, ..., N$,
$g_p(z) = \dfrac{g_{p-1}(z_{p-1}) - g_{p-1}(z)}{(z - z_{p-1})g_{p-1}(z)}$ with $p \geq 2$.
It can be shown that $C_N(z) = \frac{A_N(z)}{B_N(z)}$ where A_N and B_N are polynomials give by the recursion formula
$A_{n+1}(z) = A_n(z) + (z - z_n)a_{n+1}A_{n-1}(z)$ with $n = 1, 2, ..., N-1$
$B_{n+1}(z) = B_n(z) + (z - z_n)a_{n+1}B_{n-1}(z)$ with $n = 1, 2, ..., N-1$
and $A_0 = 0$, $A_1 = a_1$, $B_0 = B_1 = 1$.

A comparison between results obtained with the real-axis equations and results obtained with the Padé method is shown in Figure 3.2 .

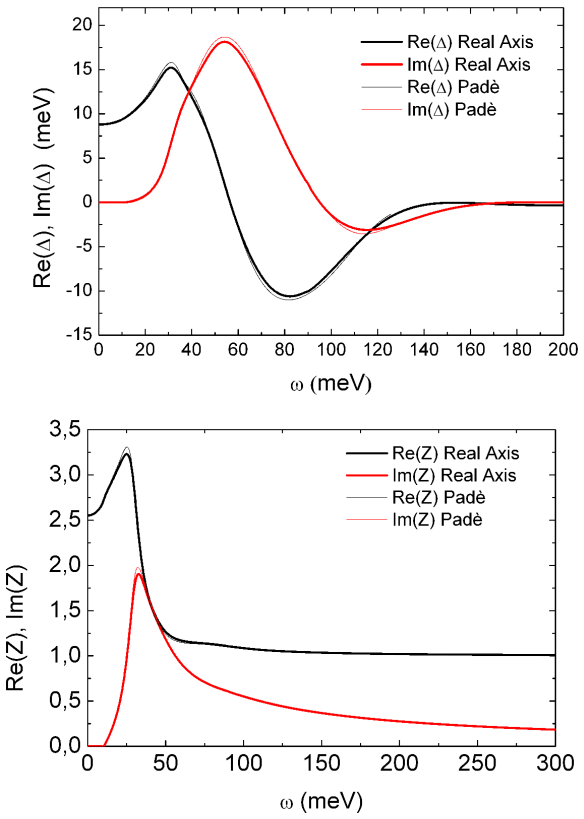

Figure 3.2: Validity check of Padé approximants methods. Here real and imaginary part of $\Delta(\omega)$ and $Z(\omega)$ are shown at $T < T_C/10$.

3.5.2 Marsiglio, Schossmann and Carbotte formulation

In a more recent method [53] of analytic continuation from imaginary to real axis there are two equations for the renormalized frequency $\widetilde{\omega}(\omega)$ and the pairing function $\phi(z)$, here $\widetilde{\omega}(z) = zZ(z)$.

$$\begin{aligned}\widetilde{\omega}(\omega) &= \omega + i\pi T \sum_{m=1}^{\infty} \frac{\widetilde{\omega}(i\omega_m)}{\sqrt{\widetilde{\omega}^2(i\omega_m) + \phi^2(i\omega_m)}} \big[\lambda(\omega - i\omega_m) - \lambda(\omega + i\omega_m)\big] \\ &\quad + i\pi \int_{-\infty}^{\infty} dz \frac{\widetilde{\omega}(\omega - z)}{\sqrt{\widetilde{\omega}^2(\omega - z) - \phi^2(\omega - z)}} \alpha^2 F(z) \big[n(z) + f(z - \omega)\big] \qquad (3.59) \\ \phi(\omega) &= i\pi T \sum_{m=1}^{\infty} \frac{\phi(i\omega_m)}{\sqrt{\widetilde{\omega}^2(i\omega_m) + \phi^2(i\omega_m)}} \big[\lambda(\omega - i\omega_m) - \lambda(\omega + i\omega_m) - 2\mu^* \theta(\omega_C - |\omega_m|)\big] \\ &\quad + i\pi \int_{-\infty}^{\infty} dz \frac{\phi(\omega - z)}{\sqrt{\widetilde{\omega}^2(\omega - z) - \phi^2(\omega - z)}} \alpha^2 F(z) \big[n(z) + f(z - \omega)\big]. \qquad (3.60)\end{aligned}$$

These equations give solutions for the real-axis gap and renormalization function that are identical to those obtained from the solution of the real-axis equations. Then they are valid at any temperature, but their numerical solution presents problems completely analogous to those of the formulation on the real axis. The choice between these equations and those on the real axis is just a matter of personal choice.

3.6 Approximations of Standard Eliashberg Equations

As mentioned before, the standard Eliashberg theory has been formulated within a lot of approximations. Here a list of these simplifications with possible generalizations is reported:

- **Validity of Migdal's theorem:** In almost all superconductors the condition $\omega_D/E_F << 1$ is fulfilled. In HTCS and fullerenes $\omega_D/E_F \sim 10^{-1}$ and the it is necessary to include the vertex correction in the self-energy [61, 62].

- **One conduction band:** Before the discovery of MgB_2 all the known superconductors could be described within one-band models. Then the theory has been generalized to two (MgB_2) [63] or more bands (iron pnictides).

- **Isotropic order parameter:** In the oldest superconductors the order parameter does not depend on the position on the Fermi surface. There are experimental evidences that this is not true in HTCS, i.e. $\Delta \equiv \Delta(\mathbf{k})$ [64–66].

- **Singlet superconductivity:** Usually the spin of Cooper pairs is equal to zero, but in Sr_2RuO_4 [67] probably it is equal to one and this implies also a different spatial symmetry (p-wave) [51].

- **Infinite conduction bandwidth:** In almost all superconductors the width of the conduction band is much larger then the representative energy of the boson mediating the Cooper pairs interaction (phonons, antiferromagnetic spin fluctuations) and then it can be considered to be infinite. In HTCS and Fullerenes this approximation breaks down and the real bandwidth has to be included in the theory [56].

- **Half filling:** Typically the number of the carriers conduction band is symmetric but in HTCS this is not true and the number of the Eliashberg equation increases because $\chi(\omega) \neq 0$ [56].

- **Flat normal density of state:** Generally the normal density of state can be approximated by a constant around the Fermi level. In $PuCoGa_5$ and in a small number of other compounds this approximation is not possible [68] and also in this case the number of Eliashberg equations increases [51].

- **No disorder and magnetic impurities:** A material can be disordered with chemical doping or neutron irradiation, moreover magnetic impurities can be added. In order to describe these physical situations new terms in the Eliashberg equations have to be introduced [69].

- **No proximity effect:** The system of a thin layer of a noble metal over a superconductor can be described by means of a generalization of Eliashberg equations [57].

3.7 Multiband Eliashberg Theory

The equations seen so far (in all their formulations) are suitable to describe only a relatively small number of superconductors. There are many materials which are less trivial and show a multiband structure. Consider a superconductor containing several different groups of electrons occupying distinct quantum states. The most typical example is a material with several overlapping energy bands. One can expect that each band will possess its own energy gap. This means that the density of states of the superconducting pairs contains several peaks. Of course if the energy gap were defined as the smallest quantum of energy that can be absorbed by the material, then only the smallest gap of the system would satisfy this definition. Thus to avoid misunderstanding, when talking about multigap structure of a spectrum we will mean explicitly the aforementioned multipeak property of the density of statesIn this case the previous equations must be generalized.
Considering a two band system [63] as the MgB_2, the parameters multiply: if a two bands model is considered, there are four separate electron-phonon spectral functions $\alpha^2_{ij}F(\Omega)$, where $i, j = 1, 2$ and four Coulomb pseudopotential μ^*_{ij}.
The isotropic Eliashberg equations generalized to n bands ($i = 1, ..., n$), without

impurities, are written on the imaginary axis as

$$\begin{aligned} \omega_n Z_i(i\omega_n) &= \omega_n + \pi T \sum_{m,j} \lambda_{ij}(i\omega_n, i\omega_m) N_j^Z(i\omega_m) + \\ &\quad + \sum_j \left[\Gamma_{ij} + \Gamma^M{}_{ij}\right] N_j^Z(i\omega_n) \qquad (3.61) \\ Z_i(i\omega_n)\Delta_i(i\omega_n) &= \pi T \sum_{m,j} \left[\lambda_{ij}(i\omega_n, i\omega_m) - \mu_{ij}^*(\omega_c)\right] \times \\ &\quad \times \Theta(\omega_c - |\omega_m|) N_j^\Delta(i\omega_m) + \sum_j [\Gamma^M{}_{ij} + \Gamma^M{}_{ij}] N_j^\Delta(i\omega_n) \qquad (3.62) \end{aligned}$$

where Γ_{ij} and $\Gamma^M{}_{ij}$ are the non magnetic and magnetic impurity scattering rates, and, in a manner quite similar to the single band case,

$$\lambda_{ij}(i\omega_m - i\omega_n) \equiv 2 \int_0^\infty d\Omega \frac{\Omega\, \alpha_{ij}^2 F(\Omega)}{\Omega^2 + (\omega_n - \omega_m)^2} \qquad (3.63)$$

and

$$N_j^\Delta(i\omega_m) = \Delta_j(i\omega_m) \cdot \left[\sqrt{\omega_m^2 + \Delta_j^2(i\omega_m)}\right]^{-1}, \qquad N_j^Z(i\omega_m) = \omega_m \cdot \left[\sqrt{\omega_m^2 + \Delta_j^2(i\omega_m)}\right]^{-1}.$$

The diagonal elements describe the intraband coupling, while the off-diagonal the interband one.
The values of the interband coupling constants are not completely free, but there is a constrain

$$\frac{\lambda_{ij}}{\lambda_{ji}} = \frac{N_i(0)}{N_j(0)}. \qquad (3.64)$$

This means that the ratio of the interband coupling constant λ_{12} and λ_{21} is equal to the ratio of density of states.
It is interesting and propaedeutic for the subsequent chapters to analyze different situations, as the coupling constants change, the limit of small interband coupling and the opposite case i.e. a pure interband case [63] will be considered. The first case is interesting because it allows understanding that an, even small, interband coupling leads to the correlation of the two bands, otherwise completely independent as it is shown in Figure 3.3. In a superconductor without interband coupling ($\lambda_{ij} = \lambda_{ji} = 0$) the bands behaves as n different superconductors and they will have n different transition temperatures, T_{C_1} and T_{C_2}, each associated with the respective band. The superconducting state will results, in several properties, the sum of the n bands contributions which are completely independent. As the off-diagonal components grow the n bands become connected. However, this does not means that the superconductor behaves as a one-band system. Until each band has different spectral function, and then different coupling constant, they will apport different contributions. Changing the off-diagonal elements λ_{ij}, different temperature dependence of the upper and lower gaps comes out. Each band contains its own set of Cooper pairs. Since, generally speaking, k_{Fi} and

k_{Fk} (here k_{Fi} and k_{Fk} are the Fermi momenta for different bands), there is no pairing of electrons belonging to different energy bands i.e. λ_{ik}, of course, does not represent a pairing between electrons of different bands. This does not mean, however, that the pairing within each band is completely insensitive to the presence of the other. On the contrary, a peculiar interband interaction and the appearance of nonlocal coupling constants are fundamental properties of the multiband model. Consider two electrons belonging to band i. They exchange phonons and form a pair as a result. There exists two pairing scenarios. In one of them, the first electron emits a virtual phonon and makes a transition into a state within the same energy band. The second electron absorbs the phonon and also remains in the same energy band, forming a bound pair with the first one. This is the usual pairing picture, described by a coupling constant λ_{ii}. However, the presence of the other energy band gives rise to an additional channel. Namely, the first electron, originally located in the i band, can emit a virtual phonon and make a transition into the k band. The phonon is absorbed by the second electron, which also is scattered into the k band, where it pairs up with the first electron. As we know, there is no energy conservation requirement for single virtual transitions; such conservation, however, must hold for the initial and final states. In our case this criterion is met. Indeed, the initial and final states correspond to particles on the Fermi surface. Note that, in addition, the initial and final total momenta are equal to zero. Thus the initial state had two electrons in the i band, while the final state finds a pair in the k band. Interband charge transfer processes are described by nondiagonal coupling constants λ_{ik}, and because of them the system is characterized by a single critical temperature. Otherwise, each set of electrons would have its own T_c.

There is a formal similarity between the Eliashberg equations for a proximity system [57] and for a two band system: if the mathematical expression of Eliasberg theory for a system with two gaps is compared with a proximity system it is possible to notice a profound formal analogy between these two situations. In both cases there is induced superconductivity because in the second band, as in a noble metal film, a very week intrinsic pairing can be chosen so this band alone would not become superconductive. However the mechanisms giving rise to induced superconductivity are very different. In the two band model the systems are "separated" in momentum space and the second band acquires an order parameter thanks to phonon exchange. The phase space for phonons is effectively increased. In the proximity effect on the other hand the systems are spatially separated and superconductivity is induced by the tunnelling of Cooper pairs.

The multiband Eliashberg model developed above can also be used to explain the experimental data of temperature dependence of the upper critical magnetic field [70, 71]. For the sake of completeness, the linearized gap equations in the presence of magnetic field, for a superconductor in the clean limit are reported.

In the following, v_{Fj} is the Fermi velocity of the $j-th$ band, and H_{c2} is the upper critical field:

$$\begin{aligned}
\omega_n Z_i(i\omega_n) &= \omega_n + \pi T \sum_{m,j} \lambda_{ij}(i\omega_n - i\omega_m)\mathrm{sign}(\omega_m) \\
Z_i(i\omega_n)\Delta_i(i\omega_n) &= \pi T \sum_{m,j} \left[\lambda_{ij}(i\omega_n - i\omega_m) - \mu^*_{ij}(\omega_c)\right] \cdot \\
&\quad \cdot\theta(|\omega_c| - \omega_m)\chi_j(i\omega_m)Z_j(i\omega_m)\Delta_j(i\omega_m) \\
\chi_j(i\omega_m) &= \frac{2}{\sqrt{\beta_j}} \int_0^{+\infty} dq \exp(-q^2) \cdot \\
&\quad \cdot \tan^{-1}\left[\frac{q\sqrt{\beta_j}}{|\omega_m Z_j(i\omega_m)| + i\mu_B H_{c2}\mathrm{sign}(\omega_m)}\right]. \qquad (3.65)
\end{aligned}$$

Here $\beta_j = \pi H_{c2} v_{Fj}^2/(2\Phi_0)$ and Φ_0 is the unit of magnetic flux. In these equations the bare Fermi velocities v_{Fj} [71] are the input parameters.

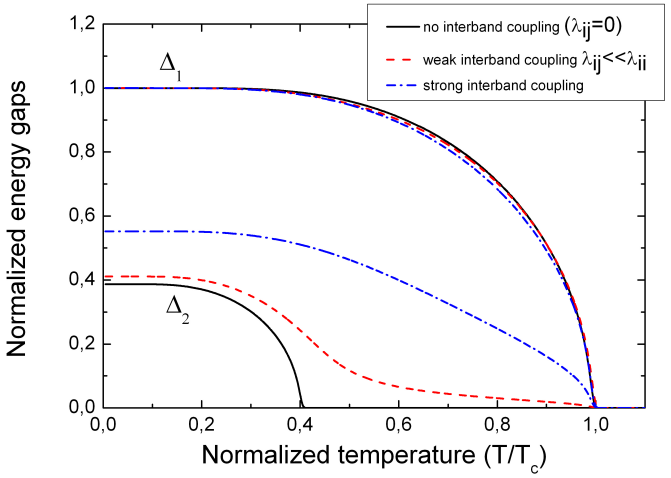

Figure 3.3: Temperature dependence of the gaps Δ_1 and Δ_2 in a two-band model, calculated in the cases of: no intraband coupling (solid lines); weak intraband coupling (dotted lines); strong interband coupling (dash-dot lines). The intraband coupling constants are arbitrary; here we used those for MgB_2.

Chapter 4

LiFeAs

In this chapter I will describe in more details LiFeAs compound, a member of the 111 family of FeSC. I will discuss both the normal and the superconducting phase. The resistivity curve will be studied above the critical temperature, in order to study the transport properties. As concern the superconducting state the symmetries and the amplitudes of the order parameters are discussed within the Eliashberg theory supported by DFT first principle calculations to evaluate the principal input parameters that are needed to solve the Eliashberg equations. In order to explain the phenomenology of LiFeAs superconductor we proposed a four-band s± Eliashberg model.
Experimental data taken from literature, in particular the critical temperature, the gap values and the upper critical magnetic field, can be reproduced very well within an effective model in a moderate strong coupling regime that must include both the usual interband spin-fluctuation coupling ($\lambda_{sf}^{tot} \sim 1.5$) and an unusual intraband term (with coupling strength $\lambda_{11} \sim 0.9$). The presence of a not negligible intraband coupling is discussed as a possible fictitious effect due to the breakdown of the Migdal's theorem.

"I don't mind not knowing. It doesn't scare me."
Richard P. Feynman

4.1 Introduction

The 111 class of iron compounds has been discovered in 2008 later than some other superconductors belonging to the 1111 and 122 classes were studied. The interest in these compounds was dictated obviously by the presence of the Fe-As structure, supposed to be heavly influence the superconducting properties in all the FeSc. It has been found that compounds as LiFeAs or NaFeAs are superconducting at 18K [72] and 9K [73] even without doping or applied pressure.

It was immediately clear that these compounds showed peculiar characteristics; as instance they are, at least from the structural point of view, simpler with respect to the other FeSCs discovered. This induced the hope to find answers to some questions about this new class of materials. Actually, the situation is not so simple: despite the huge theoretical and experimental effort devoted to the comprehension of its properties, several questions about this compound do not have a definite answer.

4.1.1 A very peculiar compound

LiFeAs is really peculiar with respect to all the other FeSC. In most of all superconductors belonging to this new family the main characteristic is the proximity or even the coexistence of the magnetic and the superconducting phase. However for LiFeAs the situation is not so clear. First principle calculations predicted a magnetic collinear stripped antiferromagnetic ground state with a very small spin moment and a structural transition from the tetragonal to the orthorombic *Cmma* state [74], suggesting an unconventional mechanism for the Cooper pairing [75], without anomalies with respect to the other iron compounds. However experimental data were not in agreement with these indications. There is no indication of AFM ordering down to T_c, no structural phase transition have been observed [76], even up to 20 GPa [77, 78] and neither a magnetic transition [79].

4.2 General properties

4.2.1 Crystal structure

The crystal structure of LiFeAs was already studied in 1968 [80] and the presence of Fe_2As_2 layers suggested, after the discovery of other superconductors with this characteristic, to deeper analyze this compound.
The synthesis of this compound was not easy, and at the beginning it was thought that in order to have superconductivity Li vacancies were needed [7].
LiFeAs crystallizes in a tetragonal unit cell with a=3.7914(7) Å and c=6.364(2) Å with spacegroup P4/nmm (No. 129). The crystal structure is shown in Figure 4.1 and all the crystal parameters are reported in Table 4.1.
As the other iron compounds, LiFeAs contains $FeAs_4$ edge-sharing tetrahedra. The Fe-As bond distance within the layers is 2.4204(4) Å, the nearest Fe-Fe distance is 2.6809(4)Å, compared with "1111" RFeAsO or "122" AFe_2As_2, both

c axis or ab plane is considerably shrunk for "111" LiFeAs. The Fe_2As_2 layers are alternately stacked along the c axis with nominal double layers of Li atoms. The parallel stacking of the FeAs layers in LiFeAs inhibits close inter-

Atom	Wyckoff	x	y	z
As(1)	2c	0.25	0.25	0.2635(1)
Fe(2)	2b	0.75	0.25	0.50
Li(3)	2c	0.25	0.25	0.8459(15)

Table 4.1: Crystal structure parameters of LiFeAs. Tetragonal unit cell with a=3.7914(7) Å and c=6.364(2) Å with spacegroup No. 129.

layer contacts between As atoms. This is different from the "slipped" stacking in (A,Ae)Fe_2As_2 wherein adjacent Fe_2As_2 layers are oriented by a mirror plane perpendicular to c passing through z=1/2, which allows closer, yet nonbonding, As-As interlayer distances. Although the interlayer distances in LiFeAs (3.1822 Å) are shorter than the ROFeAs phases, the nearest interlayer As-As distances are long (4.29297 Å). More importantly, unlike LaOFeAs, the nominal tetrahedral sites within the nominal Li-double layers Li-Li distances of 3.32184 Å, as shown in Figure 4.1 do not have any notable electron densities and thus are unoccupied.

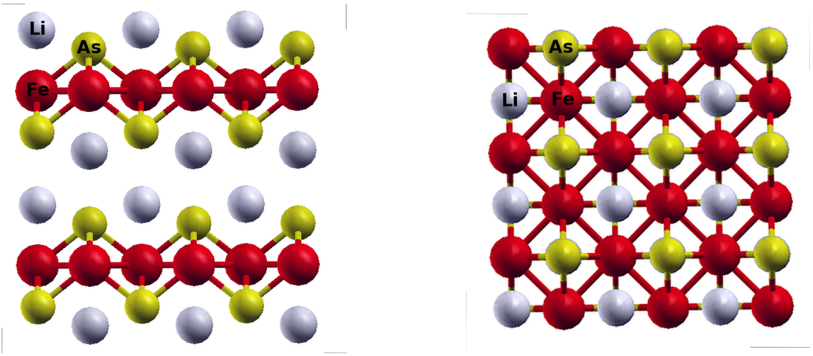

Figure 4.1: Crystal structure of LiFeAs superconductor lateral and top view.

4.2.2 Electronic structure

In LiFeAs, as in many other iron-compounds, the density of state (DOS) near the Fermi level is dominated by the Fe 3d states as depicted in Figure 4.2(a). In a similar way to other FeSCs the FS is composed of hole cylinders at the center of the BZ and electrons pockets at the corners [15]. We have evaluated the band structure and the Fermi surface of this compound, our results (reported in Figure 4.8(b) and Figure 4.3) are compatible with other calculations that can be

FS	N(0)	$v_F^{\parallel ab}$	$v_F^{\parallel c}$	$\omega_p^{\parallel ab}$	$\omega_p^{\parallel c}$
1	0.556	1.157	0.207	1.131	0.202
2	0.646	1.382	0.032	1.455	0.034
3	0.616	1.535	0.865	1.581	0.890
4	0.370	2.014	0.459	1.161	0.365
5	0.039	2.454	1.227	0.639	0.319
TOT	2.228	1.523	0.529	2.980	1.035

Table 4.2: Fermi Surface resolved Kohn Sham properties: The Fermi density of states ($N(0)$) is given in states/spin/eV, the Fermi velocities (v_F) in 10^5 m/sec, and plasma frequencies (ω_p) in eV. *ab* indicates the in-plane and *c* the out-of-plane direction of the Fermi velocities and the diagonals of the plasma tensor [82].

found in literature. We obtained three hole bands around the Γ point and two electronic bands at the corner of the Brillouin zone (around the M point). The

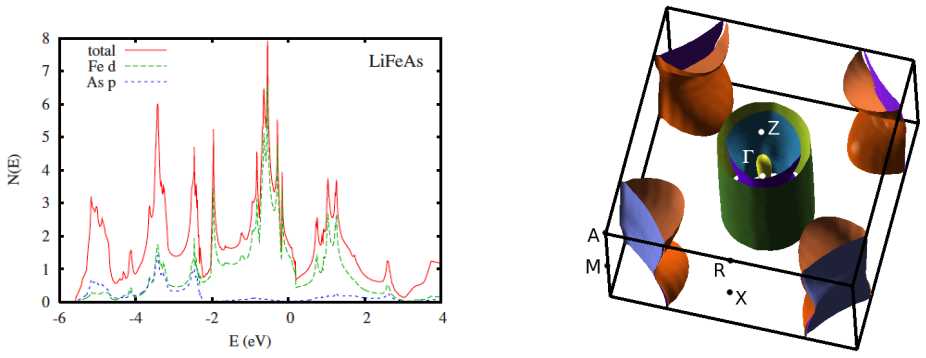

Figure 4.2: Electronic properties of LiFeAs: Density of the states (taken from [15]) and Fermi surface.

first principle calculations have been performed with Quantum Espresso [39] and compared with the results obtained within the all-electron code ELK [42].
The electronic calculations with Quantum Espresso [81] have been done within Kohn-Sham [31] density functional theory in the PBE [36] approximation for the exchange correlation functional and using the experimental lattice structure [72]. Ultrasoft pseudopotentials are used to describe core states, while valence wavefunctions are expanded in planewaves with a 40 Ryd cutoff (400 Ryd for charge expansion). A coarse grid of 20 x 20 x 16 k-points is explicitly calculated and then Fourier interpolated to compute accurate Fermi velocities and plasma frequencies. All the results obtained are reported in Table 4.2. All the calculations have been performed also with the all-electron, full-potential, linear augmented plane wave (FP-LAPW) method as implemented in the ELK code [42], still adopting the PBE approximation for the exchange-correlation potential. The Brillouin zone was sampled with a 20 x 20 x 16 mesh of k-points and the convergence of self-consistent field calculations has been attained with a total energy

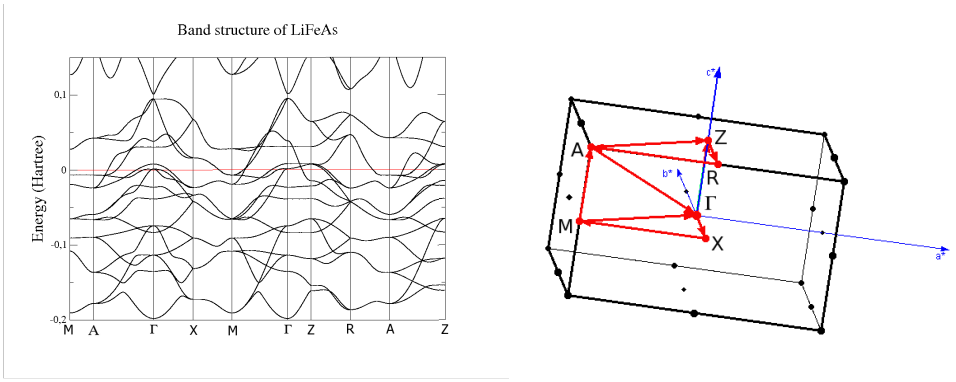

Figure 4.3: Band structure of LiFeAs evaluated within Elk code along the path depicted in the right panel.

convergence tolerance of 10^{-8} Hartree.
We set the parameter $\mathrm{RMTK_{max}} = 7$, where RMT is the smallest muffin-tin radius and $\mathrm{K_{max}}$ is a cutoff wave vector. The valence electrons wave functions inside the muffin-tin spheres are expanded in terms of spherical harmonics up to $\mathrm{l_{max}} = 8$, and in terms of plane waves with a wave vector cutoff $\mathrm{K_{max}}$ in the interstitial region. The charge density is Fourier expanded up to a maximum wave vector $\mathrm{G_{max}} = 13a_0$. The results are totally compatible with that obtained with the pseudopotential method and with other first principle calculations that can be find in literature [15] and also with experimental data, as can be seen by looking the Figure 4.4 (taken from [83]) where the authors compare the ARPES measurements with theoretical calculations. The largest hole band is almost perfectly two-dimentional, as found experimentally. However the other two bands centered in Γ seems to be a little bit more three-dimensional in our calculations with respect the measurements we are referring to. The electronic bands seems to be in very good agreement with measurements. A van Hove singularity in the proximity of the Fermi level can be obtained within first principle calculations and also observed with ARPES measurements. And this could be the necessary point to explain superconductivity in this compound. Moreover, de Haas-van Halphen measurements [84] suggest that the renormalized mass m^* is much larger with respect to other iron compounds, and this feature can have important implications as will be discussed hereafter.

4.2.3 Phonons

Several calculations prove that the electron-phonon coupling for iron based superconductors is too weak to justify so high critical temperatures [85]. The LiFeAs compound does not deviate from this feature. Also in this case DFT calculations

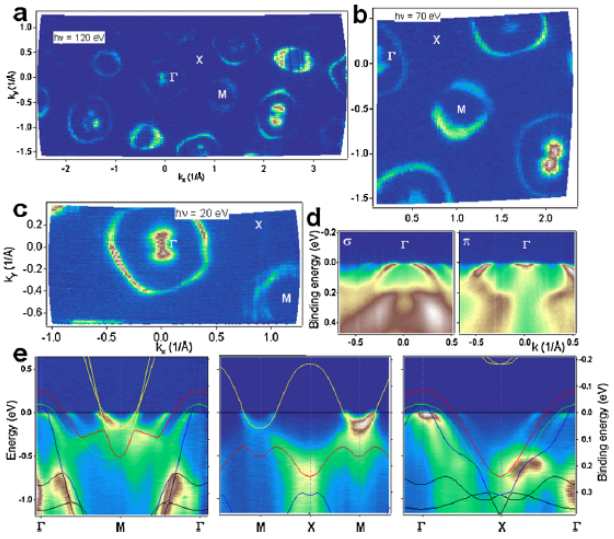

Figure 4.4: ARPES measurements of the electronic structure of LiFeAs: (a)-(c) Fermi surface maps at different excitation energies at ∼1 K, energy dispersion around the Γ point and (e) comparison with first principle calculations. Taken from [83].

of electronic and lattice properties [86] demonstrate that phonons cannot be responsible for the superconducting transition. The evaluated coupling strength is $\lambda \sim 0.29$. Considering the phonon spectra [86], that gives a logarithmic average phonon frequency (expressed in Kelvin) $\omega_{log} \sim 100$ K, one obtains through the Allen and Dynes formula a rough idea of the critical temperature:

$$T_c = \frac{\omega_{log}}{1.2} exp\left[\frac{-1.04(1+\lambda)}{\lambda - \nu^*(1+0.62\lambda)}\right]. \tag{4.1}$$

This results in a critical temperature lower than 1 K. The conclusion is then that LiFeAs, as other iron-based superconductors, is not a conventional superconductor.

Confirmations of this idea come from the experimental front [87] where the phonon modes have been investigated and no anomalies have been found across the superconducting transition nor evidence for relevant electron-phonon coupling has been measured.

4.2.4 Magnetic fluctuations

As already explained in Chapter 1, generally speaking, in this new class of superconductors there is a magnetic phase with a SDW order attributed to the presence of nesting between electron and hole pockets of the Fermi surface. The SDW order is then suppressed, often by a structural transition, and this allows the superconducting transition, in any case antiferromagnetic spin fluctuations

still persist below the critical temperature and are responsible for the pairing. However LiFeAs does not undergo to a structural or magnetic transition and its FS does not show nesting. This could suggest that this superconductor, because of its electronic structure, may have peculiar properties if compared with other Fe-compounds.
However, since 2010 the better quality of the single crystal allowed a lot of measurements in order to deep investigate the magnetic state of this compound and to clarify what are the possible coupling mechanisms in this peculiar compound. Strong evidences of low-temperature spin fluctuations came from NMR studies [88] and this could unify LiFeAs with other FeSC suggesting that they all share the same superconducting mechanism. Several questions about the relation between nesting and spin fluctuations at this point are still open, but it could seem that nesting is not necessary to have an unconventional superconductor.
Incommensurate magnetic fluctuations [76, 89] supposed to originate from the scattering between the large hole pocket and the two electron pockets [90]. The reason of the choice of the large hole pocket is that it is two dimensional; the inner hole pocket is smaller but strongly three dimensional and this would produce a strong dispersion of the incommensurate magnetic excitations along the q_z-axis [90]. Then LiFeAs is located very near the boundary with the magnetic phase and that AF spin fluctuations could play a significant role in the superconductivity of this compound. This is in agreement with the INS observation of a peak in the imaginary part of the susceptibility at an incommensurate AF wave vector [89] despite the poor nesting between the electron and hole pockets observed by ARPES [83]. Taylor et al. [91] observed an increase of the intensity at an energy of the order of 8 meV on cooling below T_c, this is consistent with a superconductivity-induced spin-resonance peak. It is quite important to notice that also ferromagnetic fluctuations are present but the AF-SF dominate at low energy that is the scale relevant for superconductivity.

4.3 The superconducting phase: a four band Eliashberg model

Dealing with the superconducting state the most important points to be discussed are the symmetry of the superconducting gaps and the pairing mechanism. We are able to reproduce experimental data taken from literature within a four band Eliashberg model with two hole and two electron gaps with opposite phase, as described for FeSC [25], where the spin fluctuations mediate the Cooper pairing, if a new intraband coupling is introduced. The presence of

this peculiar term is supposed to be a fictitious effect of the breakdown of the Migdal's theorem [92].

4.3.1 Order parameter

The SC gap, which characterizes the energy cost for breaking a Cooper pair, is an important quantity to clarify the SC mechanism. The gap size and its momentum dependence reflect the strength and the anisotropy of the pairing interactions, respectively. Several measurements of the superconducting gaps in LiFeAs are reported in literature. Low-temperature behavior of the penetration depth $\lambda(T)$ supports a fully gapped state [93], no evidence of zero-energy quasiparticle excitations are observed in thermal conductivity [94] supporting an isotropic gap, excluding the presence of nodes or deep minima in any direction of any part of the FS. The $s_{\pm}$ symmetry is also supported in some theoretical papers [95]. On the other hand there are APERS [96] and QPI [97] measurements that support anisotropy, but still excluding the presence of nodes.
As concern the coupling, some groups [83, 98] have supported LiFeAs to be a compound with $2\Delta/k_BT_c$ values much smaller with respect to other iron compounds. This could suggest the idea of a conventional superconductivity, differentiating this compound with respect all the other FeSC.
In 2012 ARPES measurements on high quality single crystals revealed the presence of four different gaps [96]. They are reported to be slightly anisotropic, but the presence of nodes is excluded. The isotropic values reported are $\Delta_1 = 5.0$ meV, $\Delta_2 = 2.6$ meV, $\Delta_3 = 3.6$ meV and $\Delta_4 = 2.9$ meV. It is important to note that the gap value is largest on the smaller band, i.e. $\Delta_1 = 5.0$ meV is on the inner hole pocket that barely cross the Fermi level [96]. The considerable amplitude of the larger gap suggests that high values of the coupling constants might be necessary to account for the experimental data so that the Eliashberg theory for strong-coupling superconductors should be used instead of the BCS theory.

4.3.2 The general model

Despite the Fermi surface shows five different sheets, according to our electronic structure calculations the 5-th sheet can be disregarded because of its low density of states (see Table 4.2 and Figure 4.8(b)) and size. Consequently, as a starting point, we can model the electronic structure of LiFeAs by using a four-band model [99, 100] with two hole bands (that will be indicated with 1 and 2) and two electron bands (in the following labelled with 3 and 4).
A four-band Eliashberg model includes eight coupled equations for the gaps $\Delta_i(i\omega_n)$ and the renormalization functions $Z_i(i\omega_n)$, where i is the band index

(that ranges between 1 and 4) and ω_n are the Matsubara frequencies. The imaginary-axis equations are here reported again:

$$\begin{aligned}\omega_n Z_i(i\omega_n) &= \omega_n + \pi T \sum_{m,j} \Lambda^Z_{ij}(i\omega_n, i\omega_m) N^Z_j(i\omega_m) + \\ &+ \sum_j \left[\Gamma_{ij} + \Gamma^M{}_{ij}\right] N^Z_j(i\omega_n) \end{aligned} \tag{4.2}$$

$$\begin{aligned} Z_i(i\omega_n)\Delta_i(i\omega_n) &= \pi T \sum_{m,j} \left[\Lambda^\Delta_{ij}(i\omega_n, i\omega_m) - \mu^*_{ij}(\omega_c)\right] \times \\ &\times \Theta(\omega_c - |\omega_m|) N^\Delta_j(i\omega_m) + \sum_j [\Gamma_{ij} + \Gamma^M{}_{ij}] N^\Delta_j(i\omega_n) \end{aligned} \tag{4.3}$$

where Γ_{ij} and $\Gamma^M{}_{ij}$ are the non magnetic and magnetic impurity scattering rates,

$$\Lambda^Z_{ij}(i\omega_n, i\omega_m) = \Lambda^{ph}_{ij}(i\omega_n, i\omega_m) + \Lambda^{sf}_{ij}(i\omega_n, i\omega_m), \tag{4.4}$$

$$\Lambda^\Delta_{ij}(i\omega_n, i\omega_m) = \Lambda^{ph}_{ij}(i\omega_n, i\omega_m) - \Lambda^{sf}_{ij}(i\omega_n, i\omega_m), \tag{4.5}$$

because obviously in the most general case both the phonon (ph) and the spin fluctuations (sf) couplings have to be taken into account.
$\Theta(\omega_c - |\omega_m|)$ is the Heaviside function and ω_c is a cutoff energy. Moreover,

$$\Lambda^{ph,sf}_{ij}(i\omega_n, i\omega_m) = 2\int_0^{+\infty} d\Omega\Omega \frac{\alpha^2_{ij}F^{ph,sf}(\Omega)}{(\omega_n - \omega_m)^2 + \Omega^2}, \tag{4.6}$$

$\mu^*_{ij}(\omega_c)$ are the elements of the 4×4 Coulomb pseudopotential matrix and, finally,

$$N^\Delta_j(i\omega_m) = \Delta_j(i\omega_m) \cdot \left[\sqrt{\omega^2_m + \Delta^2_j(i\omega_m)}\right]^{-1}, \tag{4.7}$$

$$N^Z_j(i\omega_m) = \omega_m \cdot \left[\sqrt{\omega^2_m + \Delta^2_j(i\omega_m)}\right]^{-1}. \tag{4.8}$$

As usual, the electron-boson coupling constants are defined as

$$\lambda^{ph,sf}_{ij} = 2\int_0^{+\infty} d\Omega \, \frac{\alpha^2_{ij}F^{ph,sf}(\Omega)}{\Omega}. \tag{4.9}$$

The solution of (4.2) and (4.3) requires a huge number of input parameters (32 functions and 16 constants). Nevertheless, some of these are interdependent, others may be extracted from experiments and still others fixed by appropriate approximations.
At the beginning we fixed the same conditions that have been used for many other pnictides, as reported by Mazin at al. [25], and we assumed that:
(i) the total electron-phonon coupling constant is small and mostly intraband [101];
(ii) antiferromagnetic spin fluctuations mainly provide interband coupling [102,

103].

To account for these assumptions in the simplest way (as has already been done for other iron-compounds with good results) we can set, considering the assumption (i), the phonon coupling constants to zero ($\lambda_{ii}^{ph} = \lambda_{ij}^{ph} = 0$) doing the same for the Coulomb pseudopotenzial $\mu_{ii}^{*}(\omega_c) = \mu_{ij}^{*}(\omega_c) = 0$. This does not really mean that they are really zero, instead that the electron-phonon coupling constant and the Coulomb pseudopotential compensate each other, at least in first approximation.

For what concerns the coupling mediated by spin fluctuations, the assumption (ii) allow us to set $\lambda_{ii}^{sf} = 0$, i.e. spin fluctuations produce only interband coupling [103]. Moreover, as the coupling mediated by spin fluctuations is pair braking unless the order parameter has opposite sign in the two pockets, the result is that there is no coupling between the hole bands and neither between the electron ones. Therefore, in the specific case of LiFeAs considering two hole and two electron bands, $\lambda_{12}^{sf} = \lambda_{34}^{sf} = 0$. At this point the matrix of the coupling constant would be:

$$\lambda_{ij} = \begin{pmatrix} 0 & 0 & \lambda_{13} & \lambda_{14} \\ 0 & 0 & \lambda_{23} & \lambda_{24} \\ \lambda_{31} = \lambda_{13}\nu_{13} & \lambda_{32} = \lambda_{23}\nu_{23} & 0 & 0 \\ \lambda_{41} = \lambda_{14}\nu_{14} & \lambda_{42} = \lambda_{24}\nu_{24} & 0 & 0 \end{pmatrix} \tag{4.10}$$

where $\nu_{ij} = N_i(0)/N_j(0)$ and $N_i(0)$ is the normal density of states at the Fermi level for the $i-th$ band (in this case, $i = 1, 2, 3, 4$).

We chose spectral functions with Lorentzian shape to describe the spin fluctuations in the superconducting state i.e:

$$\alpha_{ij}^2 F_{ij}(\Omega) = C_{ij}\big\{L(\Omega + \Omega_{ij}, Y_{ij}) - L(\Omega - \Omega_{ij}, Y_{ij})\big\} \tag{4.11}$$

where

$$L(\Omega \pm \Omega_{ij}, Y_{ij}) = \frac{1}{(\Omega \pm \Omega_{ij})^2 + Y_{ij}^2} \tag{4.12}$$

and C_{ij} are normalization constants, necessary to obtain the proper values of λ_{ij}, while Ω_{ij} are the peak energies and and Y_{ij} specifies the width of the Lorentzian functions, respectively [103].

In all the calculations we set $\Omega_{ij} = \Omega_{ij}^{sf} = \Omega_0^{sf} = 8$ meV [91], and $Y_{ij} = Y_{ij}^{sf} = \Omega_{ij}^{sf}/2$ [104]. The cut-off energy is $\omega_c = 18\,\Omega_0^{sf}$ and the maximum quasiparticle energy is $\omega_{max} = 21\,\Omega_0^{sf}$. We set the parameters of the impurities to be zero Γ_{ij}=$\Gamma^{M}{}_{ij}$=0 because the ARPES measurement are on very good quality single crystals of a non-magnetic stoichiometric compound [96] then also the disorder should be absent.

Band structure calculations (see Table 4.2) provide information about the factors ν_{ij} that enter the definition of λ_{ij}. The obtained values are $\nu_{13} = 0.9019$,

	λ_{11}	λ_{tot}	λ_{13}	λ_{23}	λ_{14}	λ_{24}	Δ_1	Δ_2	Δ_3	Δ_4	T_c
Ex.	-	-	-	-	-	-	5.0	2.6	3.6	2.9	18.0
sf	0.00	1.80	1.78	0.66	0.45	0.52	3.7	2.6	3.6	2.9	15.9
sf,?	2.10	2.00	1.15	0.80	0.45	0.30	5.0	2.6	3.6	2.9	18.6
sf, ph (1)	0.86	1.62	1.06	0.79	0.42	0.30	5.1	2.6	3.7	2.9	20.0
sf, ph (2)	0.90	1.63	1.15	0.80	0.45	0.30	5.0	2.6	3.6	2.9	20.1

Table 4.3: The first row shows the experimental data. The second row concerns the pure interband case ($\lambda_{ii} = 0$) while the last three include an intraband term ($\lambda_{11} \neq 0$): A very large value appears in the first case (the third row), a smaller one if the phonon spectral function $G(\Omega)$ (fourth row) or the electron-phonon spectral function $\alpha^2F(\Omega)$ (fifth row) are considered. The critical temperatures are given in K and the gap values in meV.

$\nu_{14} = 1.5010$, $\nu_{23} = 1.0483$, $\nu_{24} = 1.7447$.

4.3.3 The inclusion of an intraband coupling

However, within these assumptions, we were not able to reproduce the gap values of LiFeAs, and in particular the high value of Δ_1, the best results that can be obtained within this model are reported in the second row of Table 4.3.
In order to solve this problem it is necessary to introduce at least an intraband coupling in the first band, then $\lambda_{11} \neq 0$.
The final matrix of the electron-boson coupling constants becomes

$$\lambda_{ij} = \begin{pmatrix} \lambda_{11} & 0 & \lambda_{13} & \lambda_{14} \\ 0 & 0 & \lambda_{23} & \lambda_{24} \\ \lambda_{31} = \lambda_{13}\nu_{13} & \lambda_{32} = \lambda_{23}\nu_{23} & 0 & 0 \\ \lambda_{41} = \lambda_{14}\nu_{14} & \lambda_{42} = \lambda_{24}\nu_{24} & 0 & 0 \end{pmatrix} \tag{4.13}$$

After these considerations the free parameters are reduced to the five coupling constants λ_{13}, λ_{23}, λ_{14}, λ_{24} and λ_{11}.
First of all we solved the system on the imaginary axis (equations 4.2 and 4.3) and we continued them analytically on the real-axis by using the approximants Padé technique. This process is less time consuming and at low temperature it provides the same results (as shown in Chapter 3). In this way we fixed the free parameters in order to reproduce the gap values at low temperature.
This value reproduced the experimental data[1] as can be seen in Figure 4.5

The large number of free parameters (five) may suggest that it is possible to find different sets that produce the same results. This is not the case, as a matter of

[1] note that the gap values we are referring to [96] are measured at 8 K. Then we fixed the values of the coupling constants at a lower temperature, in a range where the Padé approximants methods is valid but keeping into account that the values at 8 K were fixed.

fact the predominantly interband character of the model drastically reduce the number of possible choices.
At the beginning, in order to have the fewest number of free parameters, we set Ω_{11} to be the same of the antiferromagnetic SF. It is important to underline that with the symmetry of the order parameter considered in this case an intraband coupling cannot be mediated by SF, our choice is just made in order to see the effect of an intraband coupling and not to have a new free parameter, because following the phonon's calculations they cannot be responsible of superconductivity as the electron-phonon coupling is reported to be small. The question mark that we inserted in the set of data reported in Table 4.3 indicates precisely this, i.e. that we do not know which boson can mediate a coupling of that type with the same characteristic energy of spin fluctuations.
The results obtained within this model are reported in the third row of Table 4.3, the value of λ_{11} necessary to obtain the large value of the first gap is very large.

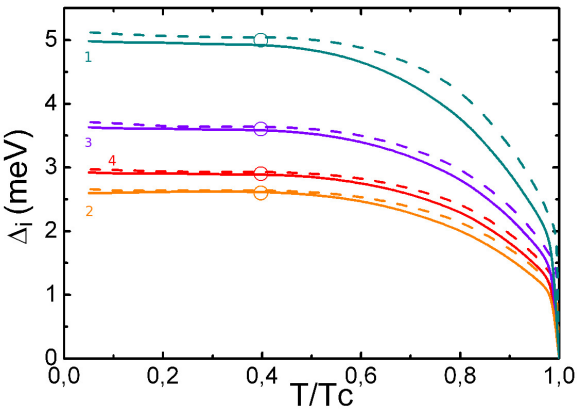

Figure 4.5: Temperature dependence of the absolute gap values (*lines*) and experimental data (*symbols*) at 8 K. The dark cyan solid (dashed) line represents the first gap, the orange solid (dashed) line the second one, the violet solid (dashed) line the third and the red solid (dashed) line the fourth, calculated with the parameters of fourth (third) row of Table 4.3.

4.3.4 The breakdown of the Migdal's Theorem

A lot of high-temperature superconductors (such as cuprates and fullrene compounds) are characterized by a very small value of the Fermi energy (E_F), of the order of the characteristic energy of the mediating boson (the Debye frequency if the superconductor is conventional). This implies a breakdown of the Migdal's theorem and then a generalization of the many-body theory of superconductivity (therefore of the Eliashberg equations) is required. The inclusion in a perturbative way (with respect to the parameter $\lambda\omega_D/E_F$) of the first order corrections

have been discussed in several papers by Pietronero, Grimaldi, Strässler and coworkers [61, 62, 105, 106]. They showed that when the vertex corrections are positive an enhancement of the critical temperature is possible and that the discussion can be extended also to unconventional superconductors. The vertex corrections have a complex structure and they depend on the frequency and the momentum of the exchanged phonon. In particular for small momentum they give rise to a positive correction and then to an enhancement of T_c.
This means (reverting the point of view) that in the case where the vertex corrections are positive and the bare Eliashberg equations are applied anyway a fictitious very strong coupling $\lambda \sim 3$ phenomenology will occur; all of this can be reinterpreted, within the theory that include this further perturbative order, in terms of a weak-coupling scheme with $\lambda = 0.5 - 1.0$.
From band structure calculations on LiFeAs it is possible to see that the value of the Fermi energy for the smaller hole band is very small. Than we can suppose that a peculiar behavior can take place because of the breakdown of the Migdal's theorem. The effect of the vertex corrections [61, 62] can be simulated by an effective coupling that is bigger than real coupling [106, 107]. Then we allowed the value of λ_{11} to change. The presence of an intraband coupling concentrated only in the first band is pretty peculiar, however is important to stress once again that this is explained as a fictitious enhancement of the real coupling constant due to the fact that we are using a theory that do not include the vertex corrections.

4.3.5 A fictitious enhancement of the phonon coupling

At this point it can be reasonable to consider phonons. Even if it has been demonstrated and summarized in Section 4.2.3 that the electron-phonon coupling is small this is just a fictitious effect due to the fact that vertex correction should not be disregarded.
Then we considered for Ω_{11} the typical phonon energies [108]. In this case (as reported in fourth and fifth row of table 4.3) the value of intraband coupling constant obviously decreases with respect to the previous case and we obtain $\lambda_{11} = 0.86 - 0.9$, while the antiferromagnetic spin fluctuations contribution still correspond to a moderate strong coupling regime ($\lambda_{tot}^{sf} \sim 1.5$).
We have solved the Eliashberg equations in two other cases: in the first case we used as spectral function for the first band the calculated phonon density of states $G(\Omega)$ and in the second case we considered the calculated total electron-phonon spectral function $\alpha^2 F_{tot}(\Omega)$ both of them appropriately scaled.
The proper choice is the second one, but this spectral function should be in principle different for each band because it is not only the phononic spectra, but it describes the coupling with the electrons and in principle this is not the same for all the bands of the FS; moreover, in LiFeAs the first band shows peculiar

characteristics and then the evaluation of the electron-phonon coupling could be not so reliable. Then we decided to use the phonon spectra $G(\Omega)$ and let the coupling (λ_{11}) to be a free parameter. These two spectral functions are shown in Figure 4.6. At this point there are no more free parameters and the model

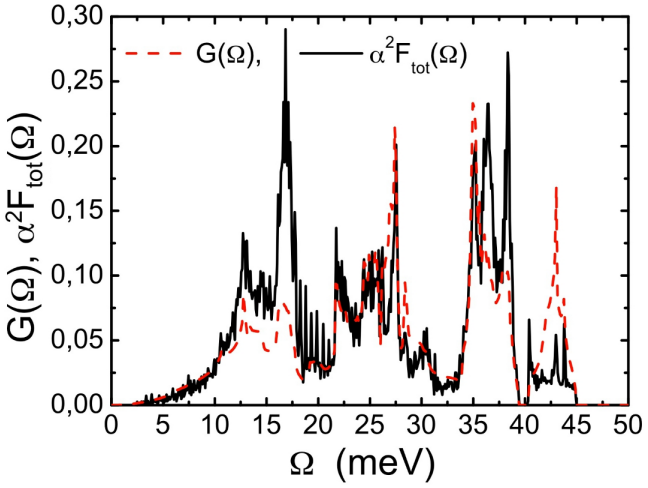

Figure 4.6: The calculated phononic density of states $G(\Omega)$ (red dashed line) and the calculated total electron-phonon spectral function $\alpha^2F_{tot}(\Omega)$ (black solid line).

can be tested and used to reproduce other experimental data. First of all we can use the real-axis Eliashberg equations to evaluate the temperature dependence of the superconducting gaps (reported in Figure 4.5) and to obtain in this way the critical temperature. We obtain a value that results to be very close to experimental one, $T_c^{calc} = 18.6 - 20.1$ K.
All the procedure has been followed both for the case with G(Ω) both for that with $\alpha^2F(\Omega)$ the parameter used are reported in the third and fourth row of Table 4.2 however the difference is not relevant from the practical point of view.

4.3.6 Critical magnetic field

The multiband Eliashberg model that we have developed above now can be used to explain the experimental data of temperature dependence of the upper critical magnetic field [109]. For simplicity, I report here the linearized gap equations in the presence of magnetic field for a superconductor in the clean limit. In the following, v_{Fj} is the Fermi velocity of the j-th band, and H_{c2} is the upper critical

magnetic field:

$$\omega_n Z_i(i\omega_n) = \omega_n + \pi T \sum_{m,j} \Lambda^Z_{ij}(i\omega_n - i\omega_m)\text{sign}(\omega_m) \quad (4.14)$$

$$Z_i(i\omega_n)\Delta_i(i\omega_n) = \pi T \sum_{m,j} \left[\Lambda^\Delta_{ij}(i\omega_n - i\omega_m) - \mu^*_{ij}(\omega_c)\right] \times \times\theta(|\omega_c| - \omega_m)\chi_j(i\omega_m)Z_j(i\omega_m)\Delta_j(i\omega_m) \quad (4.15)$$

$$\chi_j(i\omega_m) = \frac{2}{\sqrt{\beta_j}} \int_0^{+\infty} dq \exp(-q^2) \times \times \tan^{-1}\left[\frac{q\sqrt{\beta_j}}{|\omega_m Z_j(i\omega_m)| + i\mu_B H_{c2}\text{sign}(\omega_m)}\right]. \quad (4.16)$$

Here $\beta_j = \pi H_{c2} v^2_{Fj}/(2\Phi_0)$ and Φ_0 is the unit of magnetic flux. In these equations the four bare [71] Fermi velocities v_{Fj} are the input parameters. Since, as I have already explained, the first band shows peculiar characteristics with important consequences on the value of the parameters that enter the model if the simple bare theory, i.e. still without the vertex corrections, then also in the calculation of the Fermi velocity associated to this first band some anomalous behavior can be present. For this reason we decided to let the first Fermi velocity to be a free parameter and we choose it in order to obtain the best fit of the experimental data [109] while the other values have been fixed to the values reported in Table 4.2. In this way, we allow a sort of renormalization of the Fermi velocity in order to reabsorb the possible effect of the perturbative order that are not included in the Eliashberg equations.

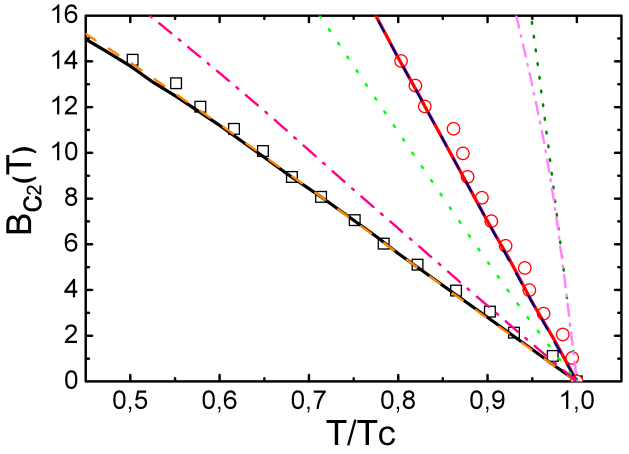

Figure 4.7: Experimental temperature dependence of the upper critical field (symbols), and the relevant fitting curves (lines) obtained by solving the Eliashberg equations in magnetic field. Red circles and solid red (dashed dark blue) line for $H_{\|c}$, black square symbols and solid black (dashed orange) line for $H_{\|ab}$ calculated with the parameters of fourth (third) row of Table 4.3. The dotted olive ($H_{\|c}$) and navy ($H_{\|ab}$) and the dashed-dotted magenta ($H_{\|c}$) and pink ($H_{\|ab}$) lines are,respectively, the fourth and first case of Table 4.3 but where v_{F1} is not a free parameter but it is taken by Table 4.2.

Then v_{F1}, in each case, is the only free parameter.
As done before we analyzed two different cases and the values that we have obtaind are: $v_{F1}^{\|c} = 2.28 \cdot 10^5$ m/s and $v_{F1}^{\|ab} = 1.74 \cdot 10^5$ m/s, in the phonon case, while if the spin fluctuation spectral function is considered the values that allows the best fit of the experimental data are $v_{F1}^{\|c} = 2.79 \cdot 10^5$ m/s and $v_{F1}^{\|ab} = 2.14 \cdot 10^5$ m/s. Figure 4.7 shows the experimental data and the best theoretical curves (solid and dashed lines) obtained by solving the Eliashberg equations within the model discussed above. As can be seen, the results obtained in the two considered cases are almost indistinguishable and in very good agreement with the experimental data.
In the Figure 4.7 also the curves calculated with v_{F1} taken by Table 4.2 when $\lambda_{11} \neq 0$ (fourth case in Table 4.3, dotted line olive and navy) and when $\lambda_{11} = 0$ (first case in Table 4.3, dashed-dotted line magenta and pink). In both situations there is no agreement with the experimental data. The curves calculated in absence of the term λ_{11} do not agree with the experimental data, so we deduce that the higher value of $v_{F1}^{\|ab,c}$ is not produced by the presence of an intraband term ($\lambda_{11} \neq 0$) but, probably, by the peculiar characteristics of band 1. However one must consider the fact that the Eliashberg equations are derived by assuming compliance to Migdal's theorem. In presence of an anomalous band dispersion as for band 1, the theory may partially break down. Allowing $v_{F1}^{\|ab,c}$ as a free parameter implicitly implies that we are "phenomenologically" going beyond the first order contributions (i.e. now we cannot neglect the effects of the vertex corrections in the band 1). The break down of the Migdal's theorem leads to use effective values of λ_{11} and v_{F1} different from real value because the framework of the theory is partially inadequate.

4.4 The normal phase: resistivity

We consider the experimental temperature dependent resistivity as measured by Heyer and coworkers [110], and reported in Figure 4.8(a). Its saturation at high temperature [109] suggests that the presence of several sheets in the Fermi surface also affects the normal state transport properties. While the low temperature behavior $\rho(T) \propto T^2$ seems to indicate that a non-phononic mechanism plays a relevant role [111].
We tried to fit the data within a one-band model [112, 113] (see equation 4.18 with $i = 1$) where the phonon spectrum has been taken from DFT calculations [114] and the plasma energy has been obtained by first principle calculation (see Table 4.2). The transport coupling constant and the value of the impurities are considered as free parameters and they are fixed to reproduce the experimental data. The obtained values are reported in Table 4.4, in particular $\lambda_{tr,tot} = 0.32$ which is in agreement with the calculated value of the transport electron-phonon

coupling constant [108]. However, as can be seen in Figure 4.8(a), within a one-band model (black dashed line) the experimental data cannot be reproduced.

4.4.1 The model for resistivity in a multiband metal

A saturation at high temperature in the normal-state electrical resistivity has been observed in many alloys [115, 116] since the 60s. This behavior can be explained within a phenomenological model containing two kinds of carriers with different scattering parameters [117], then two parallel conductivity channels have to be considered so that

$$\frac{1}{\rho(T)} = \frac{1}{\rho_e(T)} + \frac{1}{\rho_{sat}}, \tag{4.17}$$

where $\rho_e(T)$ is the resistivity of the first group of carriers, characterized by a strong temperature-dependent scattering because of its weak scattering on defects, and ρ_{sat} is the contribution of the second group of carriers that gives a strong temperature-independent contribution. It has been discussed for other iron compounds [118] that this shunt model can be derived for hole doped iron pnictides and can explain the normal-state resistivity saturation in $Ba_{1-x}K_xFe_2As_2$ single crystals. The resistivity in a multiband case can thus be obtained, extending the single-band case [112, 113] and considering the contribution of all the different channels:

$$\frac{1}{\rho(T)} = \frac{\varepsilon_0}{\hbar} \sum_{i=1}^{N} \frac{(\hbar\omega_{p,i})^2}{\gamma_i + W_i(T)}, \tag{4.18}$$

where N is the total number of the different carriers considered, $\omega_{p,i}$ is the bare plasma frequency of the ith-band and

$$W_i(T) = 4\pi k_B T \int_0^\infty d\Omega \left[\frac{\hbar\Omega/2k_BT}{\sinh\left(\hbar\Omega/2k_BT\right)} \right]^2 \frac{\alpha^2_{tr,i}F_{tr}(\Omega)}{\Omega}, \tag{4.19}$$

with $\gamma_i = \sum_{j=1}^{N}(\Gamma_{ij} + \Gamma^M_{ij})$, that is the sum of the inter- and intra-band non-magnetic and magnetic impurity scattering rates, and

$$\alpha^2_{tr,i}F_{tr}(\Omega) = \sum_{j=1}^{N} \alpha^2_{tr,ij}F_{tr}(\Omega), \tag{4.20}$$

where $\alpha^2_{tr,ij}(\Omega)F_{tr}(\Omega)$ are the inter- and intraband electron-boson transport spectral functions related to the Eliashberg functions [112]. Just for practical purposes we can define a normalized spectral function $\alpha^2_{tr,ij}F'_{tr}(\Omega)$ such that

$$\alpha^2_{tr,ij}F_{tr}(\Omega) = \lambda_{tr,ij}\alpha^2_{tr,ij}F'_{tr}(\Omega), \tag{4.21}$$

where the coupling constants $\lambda_{tr,ij}$ are defined as in Eliashberg theory [51, 112]. In order to capture the main concepts of the physical problem and not to get lost in a huge number of free parameters, we set all the normalized spectral functions to be equal, i.e. $\alpha^2_{tr,ij}F'_{tr}(\Omega) = \alpha^2_{tr}F'_{tr}(\Omega)$. In this way the transport spectral functions $\alpha^2_{tr,ij}F_{tr}(\Omega)$ differ only for a scaling factor, i.e. the coupling constant.

$$\alpha^2_{tr,i}F_{tr}(\Omega) = \lambda_{tr,i}\alpha^2_{tr}F'_{tr}(\Omega), \tag{4.22}$$

where, obviously, $\lambda_{tr,i} = \sum_{j=1}^{N}\lambda_{tr,ij}$. It is also possible to define the total transport coupling constant

$$\lambda_{tr,tot} = \sum_{i=1}^{N} N_i\lambda_{tr,i} / \sum_{i=1}^{N} N_i \tag{4.23}$$

(N_i being the density of the states at the Fermi level of the $i-$th band) for similarity with the superconducting state where

$$\lambda_{sup,tot} = \sum_{i,j=1}^{N} N_i\lambda_{sup,ij} / \sum_{i=1}^{N} N_i. \tag{4.24}$$

Note that the specific shape of the spectral function depends on which is the boson that mediates the interaction.

4.4.2 Spin fluctuations or phonons?

In the wake of our model for the superconducting state, we propose a multiband model [118, 119] to analyze the resistivity data. Two possible mechanisms responsible for resistivity will be examined: phonons and antiferromagnetic spin fluctuations.

The basic idea, based on ARPES and de Haas-van Alphen data, is that transport is drawn mainly by the electronic bands and that the hole bands have a weaker mobility [120]. Then the impurities are mostly present in the hole bands and $\gamma_{1,2} \gg \gamma_{3,4}$, while the transport coupling is much higher in bands 3 e 4 and this means that, at least as a first approximation, λ_1 and λ_2 can be fixed to be zero. In this way we will have two contributions almost temperature independent and two which change the slope of the resistivity with the temperature [118].

Let us start with the phononic case. For simplicity we considered all the spectral functions to be proportional to the phonon spectra used also in a previous fit [114]. As mentioned above the transport spectral functions are similar to the standard Eliashberg functions. The main difference is the behavior for $\Omega \to 0$ [112], where the transport function behaves like Ω^4 instead of Ω^2 as in the superconducting state. So the condition $\alpha^2{}_{tr}(\Omega)F_{tr}(\Omega) \propto \Omega^4$ has been imposed

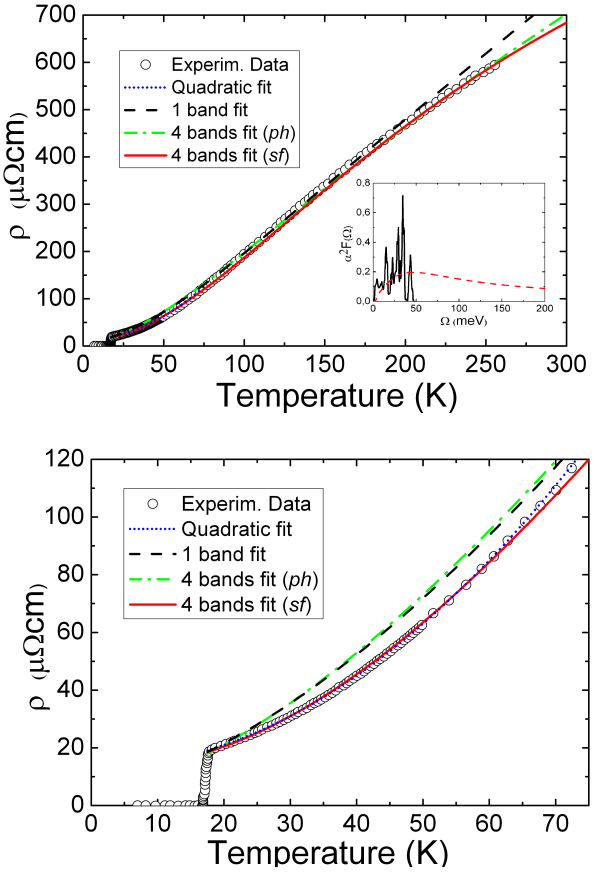

Figure 4.8: Temperature dependence of resistivity in LiFeAs. Experimental data (from Ref. [110]) and calculated fits are reported. The black dashed line comes from a single-band model. Within a four-band model two different cases have been considered, one obtained with the phononic spectrum (green dash-dotted line) and one with the antiferromagnetic spin fluctuation spectrum (red solid line). The inset shows the two normalized spectral functions that have been used, the phonon spectrum (black solid line) and the spectrum used for antiferromagnetic spin fluctuations (red dashed line). The lower panel is an enlargement of the upper panel at low temperature.

in the range $0 < \Omega < K_B T_D/10$ and then

$$\begin{aligned} \alpha^2{}_{tr}(\Omega)F'{}_{tr}(\Omega) &= b_i\Omega^4\vartheta(k_B T_D/10-\Omega) \\ &\quad +c_i\alpha^2{}_{tr}(\Omega)F''{}_{tr}(\Omega)\vartheta(\Omega-n_B T_D/10), \end{aligned} \tag{4.25}$$

where $T_D = 240$ K is the Debye temperature [121], the constant b_i and c_i have been fixed by imposing the continuity in $K_B T_D/10$ and the normalization. $\alpha^2{}_{tr}(\Omega)F''{}_{tr}(\Omega)$ is proportional to the electron-phonon spectral function [114] while $\alpha^2{}_{tr}(\Omega)F'{}_{tr}(\Omega)$ is shown in the inset of Figure 4.8(a).

All the plasma frequencies have been determined by first principle calculations (see Table 4.2) and the coupling constants considered as free parameters as well as the impurities parameters. The best fit is obtained with $\lambda_{tr,tot} = 0.14$, as reported in Table 4.4, which is in agreement with the hypothesis that the phonon

	$\lambda_{tr,tot}$	$\lambda_{tr,3}$	$\lambda_{tr,4}$	γ_1	γ_2	γ_3	γ_4	Ω_0
ph 1 band	0.32	-	-	0.90	-	-	-	-
ph 4 bands	0.14	0.44	0.10	5100	5100	0.65	550	-
sf 4 bands	0.77	1.70	1.70	164	164	4.87	1.52	47

Table 4.4: The first and second rows concern the phonon case while the third one concerns the case of the antiferromagnetic spin fluctuation spectral function. The γ_i and Ω_0 are given in meV.

coupling in LiFeAs is very weak and the value of $\lambda_{tr,4}$ almost does not influence the final result. However the experimental data are not perfectly reproduced, as can be seen by looking the green dash-dotted curve in FIG. 4.8. Moreover a huge quantity of impurity has been necessary to obtain this theoretical curve and this is not consistent with the good quality of the single crystal [109].
Then we considered the case of antiferromagnetic spin fluctuations. Now for $\Omega \to 0$ the transport function behaves like Ω^3 instead of Ω as in the superconducting state. So the condition ${\alpha^2}_{tr}(\Omega)F_{tr}(\Omega) \propto \Omega^3$ has been imposed in the range $0 < \Omega < \Omega_0/10$, then

$$\begin{aligned} {\alpha^2}_{tr}(\Omega){F'}_{tr}(\Omega) &= b_i\Omega^3\vartheta(\Omega_0/10-\Omega) \\ &\quad + c_i{\alpha^2}_{tr}(\Omega){F'}_{tr}(\Omega)\vartheta(\Omega-\Omega_0/10) \end{aligned} \tag{4.26}$$

and the constants b_i and c_i have been fixed in the same way as before.
For the spectral function ${\alpha^2}_{tr}(\Omega){F''}_{tr}(\Omega)$ we chose the theoretical antiferromagnetic spin fluctuation function in the normal state [100]

$${\alpha^2}_{tr}F''(\Omega) \propto \frac{\Omega_0\Omega}{\Omega^2+\Omega_0^2}\vartheta(\Omega-\Omega_0), \tag{4.27}$$

where Ω_0 is a free parameter: from the fit of experimental data we obtain $\Omega_0 = 47$ meV.
Also in this case the value of the free parameters are reported in Table 4.4 and in Figure 4.8 depicts the obtained results with the red solid line as well as the spectral function (in the inset). It is also important to note that the values of the impurities obtained in this case better reflect the fact that these measurements have been done on high-quality single crystal.

4.5 Conclusion

In this chapter I have discussed the very peculiar properties of LiFeAs, both in the superconducting and in the normal state.
A phenomenological model for LiFeAs superconductor able to describe its critical temperature, the multigap structure measured by Umezawa and coworkers [96]

and the critical magnetic field measurements [109].
However this process was not straightforward. In order to conjugate a spin fluctuation dominated pairing with the experimental gap structure we have been forced to introduce an intraband coupling that acts only on the first band.
This seems to be a phononic, purely intraband term and this would suggest an intrinsic incompatibility between this structure of the superconducting gaps and a purely spin-fluctuation mediated pairing.
A possible explanation may be linked to the very low Fermi energy of the band for which vertex corrections [61, 62] to the usual Migdal-Eliashberg theory may be relevant, and are expected to increase the intensity of the phononic coupling constant [106, 107], i.e. if the theory is forcedly used even out of the range of validity of the Migdal's theorem it turns out that in any case the data can be reproduced but the parameters used will be larger than the real ones.
An analogous effect appears if we try to fit the experimental data of the upper critical field. In this case we suppose that the effect of the breakdown of the Migdal's theorem can be reabsorbed in a fictitious enhancement of the value of the fermi velocity. Allowing $v_{F1}^{\|ab,c}$ as a free parameter implicitly implies that we are "phenomenologically" going beyond the first order contributions.
In conclusion, as concern the superconducting state, the breakdown of the Migdal's theorem leads to use effective values of λ_{11} and v_{F1} different from real value because the framework of the theory is partially inadequate. Our calculations show that LiFeAs presents peculiar features with respect to other iron compounds and it cannot be explained within the framework of a pure interband spin-fluctuation mediated superconductivity.

As concern the normal state we considered a model with two kind of carriers, grouping together holes and electrons. This approach reproduces accurately the experimental data, significantly better than previous attempts. The total coupling obtained is $\lambda_{tr,tot} = 0.77$ consistent with expectations, and actually smaller than the value in the superconducting state.
Moreover the impurity scattering parameters seem to account properly for the high quality of the sample. We are aware that, in spite of the good fitting, this is still a rough simplification as compared to the more plausible situation where the two mechanisms coexist. However, it is clear from our analysis that the antiferromagnetic spin fluctuations must constitute the main contribution.
In conclusion, we have shown that antiferromagnetic spin fluctuations play an important role not only in the superconducting state but also in the normal state, and by fitting the experimental resistivity we have extracted relevant information on the energy peak of the spectral function and the total transport coupling constant.

Chapter 5

$Ba(Fe,Co)_2As_2$

In this chapter I will investigate the properties of the iron based compound that has been perhaps the most studied: $Ba(Fe_{1-x}Co_x)_2As_2$. I discuss the normal and the superconducting state, both in single crystal and in thin films. As concern the former Point-Contact Andreev Reflection (PCAR) measurements are analyzed in order to obtain information about the symmetry and the amplitude of the order parameter. A further analysis of the normalized conductance spectra and in particular of the additional features that appear at energy higher than the gaps allow exploring the possible coupling mechanism will be explained and the results obtained on thin films are reported.
As regards the normal state properties, a comparison of the temperature dependence of resistivity between single-crystals and thin films is presented analyzing different level of doping. A model analogous to that used for LiFeAs is proposed and this allow a good reproduction of the experimental data if one admits a "hardening" of the electron-boson spectral function in thin films that can be explained as an effect of the strain due to the presence of the substrate.

"Believe you can do it and you are halfway there."
Theodore Roosvelt

5.1 Introduction

The 122 class is probably the most studies among all the iron based superconductrs. The prototypical member of this class is the parent compound $BaFe_2As_2$. Superconductovity can be induced by doping (both with holes [4] and electrons [6]), with isovalent substitution for example of P instead of As or applying pressure [122].

The stoichiometric parent compound undergoes a coupled structural and antiferromagnetic transition at 140 K [123]. Even if several studies have been made on this compound a lot of question are still unanswered. The main question, not only associated to this compound but to all the iron-based superconductors, is still related to the role of spin fluctuations. The cobalt doped compound is particular interesting because this kind of doping suppresses both the the magnetic and structural transitions leading to superconductivity [6], then this material allows an exploration of the interrelation between the structural and magnetic phase transitions with superconductivity.
As concern the superconducting state of the 122 superconductors a multigap scenario is suggested by the presence of several sheets of the fermi surface (as can be understood from the band structure of a specific case reported in Figure 5.1) but different possible situation can occur depending on several factors. A nodeless OP is expected (referring to the usual s± symmetry predicted for spin fluctuation superconductivity in iron compounds) but some authors promoted the hypothesis of a peculiar nodal symmetry, with three-dimensional nodes on one hole-like Fermi surface, when the latter acquires a more three-dimensional character [124] and a possible relation has been claimed between the ratio $2\Delta_h/k_BT_c$ (where Δ_h is the amplitude of the gap associated to the hole band) and the occurrence of nodes of the order parameter [125] suggesting nodless gaps for hole-doped (Ba,K)Fe_2As_2 and electron-doped $Ba(Fe,Co)_2As_2$ and a nodal order parameter for the isovalent compound $BaFe_2(As,P)_2$ [29, 125]. In this direction PCARS may help. Thanks to this technique the symmetry of the order parameter and the possible presence of nodes can be investigated, I will discuss this point in more details hereafter in this chapter. The properties of the normal

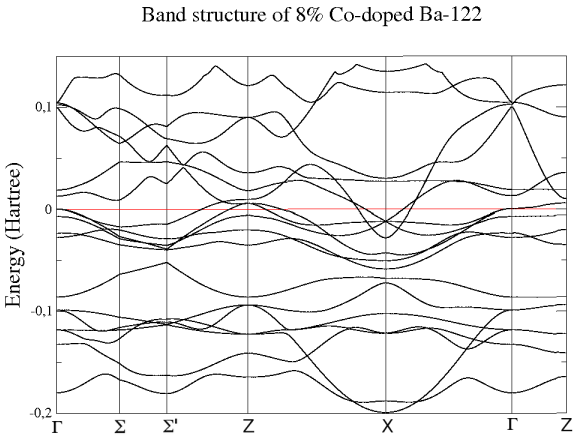

Figure 5.1: Band structure of $Ba(Fe_{1-x}Co_x)_2As_2$ with x=0.08, details of calculation are given in Section 5.3.2

state may give a lot of information also about the superconducting properties of

the material under investigation. The transport properties are a huge support to investigate the relationship between superconductivity and magnetism. In the parent compound $BaFe_2As_2$ for which electron and hole contents are identical the Hall coefficient is surprisingly negative, indicating that electrons dominate the transport properties. The same observation is found for the Co-doped samples. An analysis of the resistivity in a two-band model may allow drawing some conclusion about the properties of this compound and about the importance of spin fluctuations also in the normal state.

5.2 PCARS and the 3D version of the BTK model

The order parameter is one of the fundamental quantities of the superconducting phase of the material since it gives information on the Cooper pairs, and as a consequence, also about the coupling mechanism. Then the study of the properties of the gap, such as the number, the amplitude and the symmetry, is a fundamental step to add an important piece of information to complete complex puzzle of the properties of iron based superconductors. Here I will discuss some results obtained with the PCARS technique in compounds of the 122 family. As already described in this dissertation, the order parameter of iron compounds is generally characterized by a sign changing (i.e. a different phase factor) on the different sheets of the Fermi surface, with or without the presence of nodes depending on the specific compounds. Even if the point-contact spectroscopy is not able to appreciate the phase difference between the gaps belonging to separate sheets of the FS, but only its module, important information about the gap can be extracted with this kind of analysis.

5.2.1 The Andreev-reflection phenomenon

Andreev reflection is a particular type of scattering which occurs at the interface between a normal metal (N) and a superconductor (S) in the ideal condition of no potential barrier between them, for clearness the situation is schematized in Figure 5.2(a).
If the energy of an incident electron coming from the N side is higher than the value of the gap of S, i.e. $E > \Delta$, then the electron simply propagates in S if on the other side of the interface there are vacant electronic state at that energy. If instead the energy of the electron is $E < \Delta$ it cannot propagate because at that energy on the other side only Cooper pairs exist. But if a hole is reflected and two electrons can be transmitted in S as a Cooper pair, conserving the total charge and momentum.

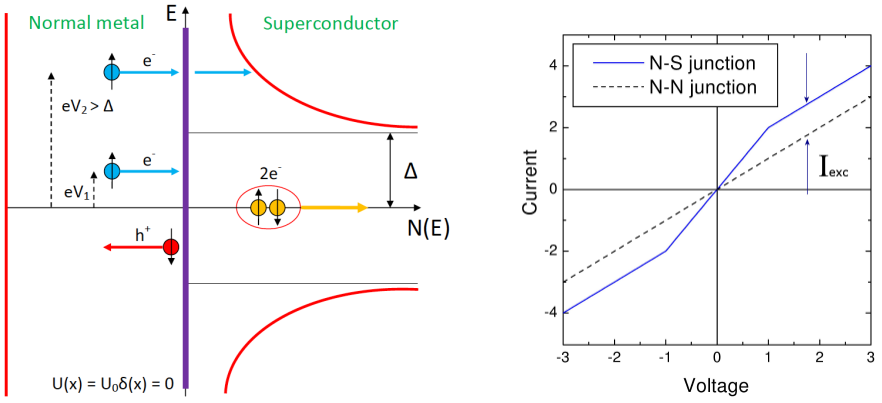

Figure 5.2: Schematic representation of the Andreev reflection taken from [126] and the I-V curve in the ideal case of an interface with no potential barrier.

If a voltage V is applied at the interface a double current, and then a double conductance, is expected as long as the energy of the electrons $E = eV$ is smaller than the gap value. Then measuring the I-V curve, as can be appreciated by looking Figure 5.2(b), the amplitude of the order parameter Δ can be determined. From the solution of the Bogoliubov-de Gennes equations near a N-S interface [127] it is possible to note that Andreev reflection does not occur abruptly at the interface but over a length scale ξ of the order of the coherence length. In general this is also the scale over which Δ is depressed due to the proximity effect generated by N on S. However, if the contact size is smaller than ξ, this effect can be neglected. Analyzing the shape of normalized conductance, i.e. $\mathrm{d}I/\mathrm{d}V$ divided by the respective conductance of the normal state, several information about the gap can be extracted and in particular condition even about the boson that mediate the superconductivity.

5.2.2 2D-BTK model

The first theoretical formulation of this phenomenon appeared in 1982 and it was proposed by Blonder, Thinkam and Klapwijk [128]. The most noticeable simplification is that the model is 1D, i.e. all the involved momenta are normal to the interface and parallel to the x axis. The barrier is represented by a repulsive potential $U_0(x)$ located at the interface, which enters in the calculations through the dimensionless parameter $Z = U_0/\hbar v_F$. In 1996 the generalization to the 2D case was proposed [129] and the normalized conductance G(E)=$(\mathrm{d}I/\mathrm{d}V)_{NS}/(\mathrm{d}I/\mathrm{d}V)_{NN}$ at T=0 (where I_{NS} and I_{NN} are the current flowing through the interface when the material is in the supeconducting or in

the normal state) can be written as a function of two quantities:

$$N_q = \frac{E}{\sqrt{E^2 - \Delta^2}} \qquad \text{and} \qquad N_p = \frac{\Delta}{\sqrt{E^2 - \Delta^2}} \tag{5.1}$$

whose real parts are the BCS quasiparticle and pair density of states, respectively. In the 2D version the charge carriers can approach the interface from any direction in the plane xy and the only condition set by the AR theory is that the component of the **k** vector parallel to the interface is conserved in all processes. In the S side a Cooper pair propagates essentially in the same direction as the incident electron (neglecting the small refraction due to the different fermi velocities in the two side of the interface). Calling θ the angle between the direction of the incident electron and the normal to the interface, the conservation of transverse momenta leads to the following dependence of the transparency τ_N on θ:

$$\tau_N(\theta) = \frac{\cos^2\theta}{\cos^2\theta + Z^2} \tag{5.2}$$

at the increase of Z the transmission becomes progressively weaker and more directional around the perpendicular to the interface. In particular, for a transparent barrier (Z = 0), the normal transmission probability is identically 1 for any direction of the incoming electron. When Z≠0, instead, the barrier transparency depends on the direction of the incoming electron; and for Z = 10 (tunneling regime) the transmission probability is always small and highly directional. it is possible to demonstrate that the BTK conductance at T = 0 is given by:

$$\sigma_S(E,\theta) = \frac{1 + \tau_N(\theta)|\gamma(E)|^2 + (\tau_N(\theta) - 1)\,|\gamma^2(E)|^2}{|1 + [\tau_N(\theta) - 1]\,\gamma^2(E)|^2} \tag{5.3}$$

where

$$\gamma(E) = \frac{N_q(E) - 1}{N_p(E)} \tag{5.4}$$

and finally the conductance is given by:

$$G_{2D}(E) = \frac{\int_{\pi/2}^{\pi/2} \sigma_S(E,\theta)\tau_N(\theta)\cos\theta\,\mathrm{d}\theta}{\int_{\pi/2}^{\pi/2} \tau_N(\theta)\cos\theta\,\mathrm{d}\theta} \tag{5.5}$$

Immediate generalization of this model allow to properly include the effects of the temperature and the inclusion of possible inelastic scattering at the interface. The first point is very simple to solve and a convolution of the normalized conductance with the Fermi function is sufficient, the second point can be solved adding an imaginary part to the energy [130] described by a broadening parameter γ and then $E \to E + i\Gamma$ because this describe the reduction of the quasiparticle lifetime.

5.2.3 3D-BTK model

In order to analyze the AR spectra of iron based a first obvious generalization that allow the inclusion of the contribution of the several sheets of the Fermi surface is necessary.
With the aim to keep limited the number of fitting parameters, the standard approach is to consider a two-band and two-gap system where the values of Δ_i, Z_i and Γ_i of each band ($i = 1, 2$) have to be determined by the best fit of the experimental curves. The total normalized conductance is thus written as:

$$G_{\mathrm{tot}}(E) = w_1 G_1(E) + (1 - w1) G_2(E) \tag{5.6}$$

where $G_i(E)$ is the normalized conductance of the i-th band, evaluated in 1D or 2D BTK model, depending on the case under discussion and w_1 is the weight of the band that at this point is still a free parameter but within the 3D model will be fixed by the interaction between FS shape and the direction of the current injection.
Now the model has to be generalized to arbitrary shapes of the FS, the final result will be the full 3D generalization of the BTK model to any anisotropic feature both of the FS and of the pair potential symmetry. For simplicity the calculations is limited to the contribution of only two bands and for the directionality of the contact, only the current injections along the x axis (yz -plane interface) and along the z axis (xy-plane interface) will be analyzed (as they represent the typical experimental conditions in single crystals of the Fe-based compounds, i.e. ab-plane and c-axis contacts, respectively. The particular shape of the i-th FS is described by the wave vector $\mathbf{k}_{F,i}(\theta, \phi)$, while the unitary vector perpendicular to the FS at any point of the reciprocal space is given by

$$\mathbf{n}_{F,i}(\theta, \phi) = \frac{\partial \mathbf{k}_{F,i}(\theta, \phi)}{\partial \theta} \times \frac{\partial \mathbf{k}_{F,i}(\theta, \phi)}{\partial \phi} \tag{5.7}$$

by neglecting possible interference effects between bands that can lead to the formation of bound states at the surface the normalized conductance for current injection along the x axis is given by:

$$G_{3D,x}(E) = \frac{\displaystyle\sum_i \int_{\phi_{\min}}^{\pi-\phi_{\min}} \int_{-\pi/2}^{\pi/2} \sigma_{x,i}(E,\theta,\phi)\, \tau_{N,x,i}(\theta,\phi) \frac{v_{\mathrm{F}x,i}(\theta,\phi)}{v_{\mathrm{F}i}(\theta,\phi)}\, k_{\mathrm{F}i}^2(\theta,\phi) \sin\theta \,\mathrm{d}\theta \,\mathrm{d}\phi}{\displaystyle\sum_i \int_{\phi_{\min}}^{\pi-\phi_{\min}} \int_{-\pi/2}^{\pi/2} \tau_{N,x,i}(\theta,\phi)\, \frac{v_{\mathrm{F}x,i}(\theta,\phi)}{v_{\mathrm{F}i}(\theta,\phi)} k_{\mathrm{F}i}^2(\theta,\phi) \sin\theta \,\mathrm{d}\theta \,\mathrm{d}\phi}, \tag{5.8}$$

and on the z axis

$$G_{3D,z}(E) = \frac{\sum_i \int_{\phi_{\min}}^{\pi/2} \int_0^{2\pi} \sigma_{z,i}(E,\theta,\phi)\, \tau_{N,z,i}(\theta,\phi) \frac{v_{\mathrm{F}z,i}(\theta,\phi)}{v_{\mathrm{F}i}(\theta,\phi)}\, k^2_{\mathrm{F}i}(\theta,\phi) \sin\theta \,\mathrm{d}\theta \,\mathrm{d}\phi}{\sum_i \int_{\phi_{\min}}^{\pi/2} \int_0^{2\pi} \tau_{N,z,i}(\theta,\phi)\, \frac{v_{\mathrm{F}z,i}(\theta,\phi)}{v_{\mathrm{F}i}(\theta,\phi)} k^2_{\mathrm{F}i}(\theta,\phi) \sin\theta \,\mathrm{d}\theta \,\mathrm{d}\phi}, \tag{5.9}$$

where

$$\tau_{N,x,i}(\theta,\phi) = \frac{v_{\mathrm{F}i}(\theta,\phi) v_{\mathrm{N}x}}{\left[v_{\mathrm{F}i}(\theta,\phi) + v_{\mathrm{N}x}\right]^2 + 4Z^2_{x,i} v^2_{\mathrm{N}}} \tag{5.10}$$

and $\tau_{N,z,i}$ has an analogous expression obtained projecting along the z axis.

To obtain this generalization of the BTK model some reasonable hypothesis have been kept or added. First of all the FS of the N side is considered always spherical, moreover the points on the FS are close to the points of maximum symmetry of the energy bands, i.e. they are close to the top or the bottom of parabolic-like bands, and this hypothesis is absolutely valid in iron based superconductors. The condition of no mismatch of Fermi velocities across the interface translates here into $v_{Fi}(\theta^*,\phi^*) = v_N$ where θ^* and ϕ^2 define a point on the FS (usually in the k_xk_y plane) where we suppose the two velocities to be equal. By imposing this condition, we eliminate the need to know the term $\hbar/m^*$ that enter in the general formulation of the Fermi velocities. In this way, of course, we neglect the small deviation of the quasiparticles in crossing the interface due to the modest mismatch of Fermi velocities in N and S simply arising from the geometry of the FS in S. Finaally the limits of integration in ϕ ($\phi_{\min}$ and $\pi - \phi_{\min}$ for the injection along the x axis and $\phi_{\min}$ and $\pi/2$ for the injection along the z axis) are fixed to restrict the integration over the first Brillouin zone.

5.3 The order parameter symmetry of 122 Fe-based superconductors

Here I will discuss some results of directional point-contact Andreev-reflection measurements in single crystals of 8% Co-doped Ba-122 and thin films with the same Co-content. The PCAR spectra are analyzed within the two-band 3D version of the BTK model for Andreev reflection, that includes an analytical expression for the Fermi surface in order to mimic the one calculated within the Density-Functional Theory. In the first case, the PCAR spectra taken with the current injected along the *ab* plane are compatible with the presence of two nodless gaps of different amplitude of different amplitude, with the smaller associated to the electronic band, as suggested by ARPES measurements [131]. In the case of thin films the current is injected along the c axis and the 3D-BTK

model with two nodless gaps fails to fit the PCAR spectra at low energy. This last argument is still under discussion, this could indicate the presence of "hot spots" where where the gap is strongly suppressed or 3D nodal lines on some sheets of the FSs, which has been proposed [28] to explain Raman results in this compound [132]. Moreover, some results obtained in single crystals of 6% Co-doped Ca-122 will be discussed within a model that includes line nodes on the smallest gap (residing in this case on the holelike sheet of the Fermi surface) while the large gap is supposed to be isotropic.
This picture agrees with the predictions about the emergence of 3D nodes in the order parameter of 122 compounds when the holelike FS evolves toward a topological transition from a warped cylinder to separate pockets [29, 133].

5.3.1 Experimental details

The $Ba(Fe_{1-x}Co_x)_2As_2$ single crystals (with x = 0.08) were prepared by the self-flux method [6] under a pressure of 280 MPa at the National High Magnetic Field Laboratory in Tallahassee. The crystal size is $\sim$ 1 x 1 x 0.1 mm^3, and the c axis is perpendicular to the larger surface. The resistive transition starts at $T_c^{\rm on}$= 24.5 K with $\Delta T_c(10-90\%)$=1 K. The $Ba(Fe_{1-x}Co_x)_2As_2$ epitaxial films (with x = 0.08) were deposited at the Leibniz Institute for Solid State and Materials Research (IFW) in Dresden, Germany. Two kinds of substrates were used: single-crystalline CaF_2 or MgO (in this case, with a Fe buffer layer on top of it) and the c axis is perpendicular to the surface. The superconducting transition of the films on CaF_2 has a midpoint at $T_c^{\rm mid}$= 23.35 K and its width is $\Delta T_c(10-90\%)$=1.70 K while for the films on MgO the same quantities are $T_c^{\rm mid}$= 23.8 K and $\Delta T_c(10-90\%)$=1.50 K.
The $Ca(Fe_{1-x}Co_x)_2As_2$ single crystals were grown at ETH Zurich [134], and were plate-like, with the c axis perpendicular to the plate. The superconducting transition measured from DC susceptibility starts at $T_c^{\rm on}$= 20.0 K and an effective $T_c^{\rm eff}$= 17.0 K can be determined by extrapolating the linear part of the curve.

The point contacts were made by using the "soft" technique [126]. In single crystals the contacts were put on a fresh side surface so that the current was mainly injected along the *ab* planes. In films, the point contacts were put on the top surface. Owing to the film orientation, this means that the injection occurs along the c axis. The conductance curves dI/dV vs. V of each point contact were obtained by numerically differentiating the measured I-V characteristics. The spectra were then normalized, i.e. divided by the normal-state conductance of the same contact [135].

5.3.2 Calculations of the Fermi surface within the VCA

The FS of the materials under study, i.e. $Ba(Fe_{1-x}Co_x)_2As_2$ with $x = 0.08$ and $Ca(Fe_{1-x}Co_x)_2As_2$ with x=0.06, was calculated within the DFT by using the ELK code where the generalized gradient approximation, in the Perdew-Burke-Ernzerhof version [38] was used for the exchange correlation potential. The effects of doping are included by means of the virtual-crystal approximation (VCA), an average-potential approximation that is beyond the method based only on the rigid bands shift. Generally speaking this approximation is valid at low level of doping (max 15-20%) because one studies a crystal with the primitive periodicity, but composed of fictitious "virtual" atoms that is a sort of mixture between the original specie and that used as substitutive.
In ELK [42] this approximation is implemented in the standard way, by introducing a fictitious atom at the original sites which has a fractional charge between that of the original atom and the dopant, mixing the properties of the two atoms in each orbital. This approach differs from rigid band in that it includes the self-consistent rearrangement of the charge density.
All calculations presented here in the case of $Ba(Fe_{1-x}Co_x)_2As_2$ have been performed with the experimental crystal structure for $BaFe_2As_2$ with spacegroup I4/mmm, and not the low-temperature orthorhombic distortion. The arsenide Whyckoff position is fixed to the value value obtained with the relaxation of the internal coordinates, in agreement with [15] and then $z_{As} = 0.342$. Magnetism breaks the tetragonal symmetry and leads to a small orthorhombic distortion that also affects the lattice. However, the orthorhombic distortion of the lattice parameters is small and at for our scope can be ignored. The lattice constants used for the calculations in the case of $Ba(Fe_{1-x}Co_x)_2As_2$ are $a = b = 3.9625$ Åand $c = 13.0168$ Å [15]. The height of the As atom above the Fe layer is $h_{As} = 2.0567$ Å, in agreement with the doping dependence of this parameter [15]. The resulting FS is shown in Figure 5.3(a). It features two hole-like FS sheets in Γ at the center of the Brillouin zone. Both have the shape of warped cylinders whose cross section is maximum at the top and bottom edges of the BZ, but the outer one shows a more marked warping. The two electron-like FS sheets at the corners of the BZ are also warped cylinders with the characteristic elliptical cross section whose semi-major axis varies along k_z.
The Brillouin zone was sampled with a 28x28x1 mesh of k-points and the convergence of self-consistent field calculations is attained with a total energy convergence tolerance of 10^{-5} Hartree. The radius of the muffin-tin spheres for the carbon atoms were taken as $1.3a_0$, where a_0 is the Bohr radius. We set the parameter RMTKmax = 7, where RMT is the smallest muffin-tin radius and Kmax is a cutoff wave vector. The valence electrons wave functions inside the muffin-tin spheres are expanded in terms of spherical harmonics up to lmax = 8, and in terms of plane waves with a wave vector cutoff Kmax in the interstitial

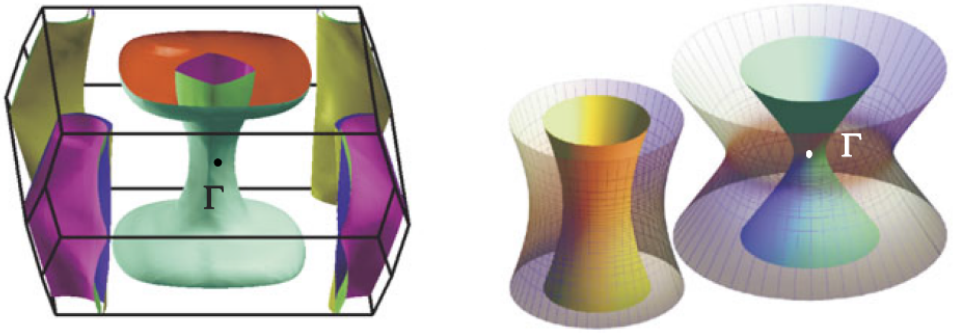

Figure 5.3: The Fermi surface of $Ba(Fe_{1-x}Co_x)_2As_2$ with x=0.08 as evaluated by first principle calculations. And the representation of the analitical expression used in the 3D-BTK model to fit the experimental conductance curves *(solid surfaces)* with the amplitude of the corresponding energy gap *(gridded surfaces)*.

region. The charge density is Fourier expanded up to a maximum wave vector Gmax = 13a_0.

Similar ab initio calculations have been done for $Ca(Fe_{0.94}Co_0.06)_2As_2$. In this case the problem was that there were no experimental information about the low-temperature lattice constants. Owing to the small dependence of the room temperature lattice parameters on the doping content [136], we assumed the low-temperature lattice constants of the parent compound $CaFe_2A_2$ in the tetragonal phase to be a good first approximation to the real ones at the doping content of our interest (x = 0.06). We then started from the lattice constants of the orthorhombic phase of $CaFe_2A_2$ at pressure P = 0 calculated as in [137], and then we made the structure tetragonal by averaging a and b. The result is $a = b = 3.925$ Å and $c = 11.356$ Å.
These values are in good agreement with the experimental ones measured in the tetragonal phase of $CaFe_2A_2$ at 300 K (and pressure P = 0.8-1 GPa [138]). Starting from the calculated equilibrium phase and always considering the antiferromagnetic phase, an optimized parameter h_{As} = 1.309Åwas obtained. The charge density was thus integrated over 8 x 8 x 4 k-points in the Brillouin zone and the band structure as well as the FSs were calculated in the nonmagnetic body-centered tetragonal phase. The resulting FS is shown in Figure 5.4(a).
It is clear that at this doping content the hole-like FS sheets are undergoing a topological transition. While at lower doping, they have the shape of strongly warped cylinders (similar to those shown for Ba-122 in Figure 5.3(a)), at x = 0.06 they split into separate cup-shaped pockets centered around the Z points.

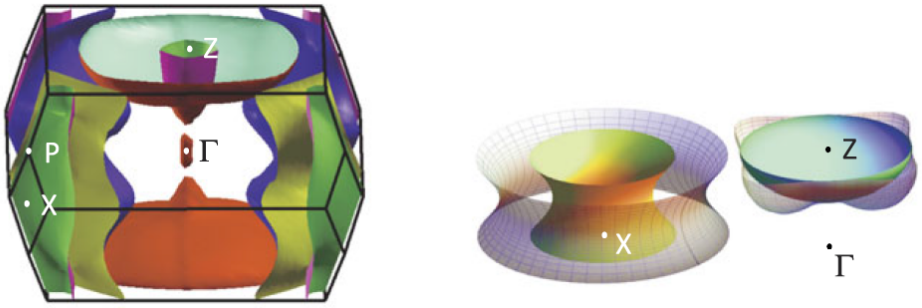

Figure 5.4: The Fermi surface of $Ca(Fe_{1-x}Co_x)_2As_2$ with x=0.06 as evaluated by first principle calculations and the the representation of the analitical expression used in the 3D-BTK model to fit the experimental conductance curves *(solid surfaces)* with theamplitude of the corresponding energy gap *(gridded surfaces)* .

5.3.3 $Ba(Fe_{1-x}Co_x)_2As_2$ single crystals

The results obtained within the ab intio calculations are useful information for the analysis of the superconducting state. Now the Fermi surfaces can be used within the 3D-BTK model in order to reproduce the normalized conductance of the Andreev-reflection spectra.

In Figure 5.5 are reported two of the spectra measured on $Ba(Fe_{0.92}Co_{0.08})_2As_2$ single crystals, both the result of *ab*-plane contacts. Both the curves (and also all the other measured on this sample) show a zero-bias dip. This is a very strong indication of the symmetry of the order parameters, this suggests both the gap to be nodeless, in agreement with ARPES measurements [131]. Moreover, two symmetric maxima appear at energy of the small gap and two other kinks related to the larger gap, in both the curves. These two structures are indicated by the dashed lines in Figure 5.5. Additional structures appear at higher energies, as indicated by the arrows. These structures are supposed to be bosonic resonances but the discussion of this kind of structure is resend to the Section 5.4. The red curve in Figure 5.5 represent the fit obtained within the 3D-BTK model that takes into account the real shape of the Fermi surfaces, as depicted in Figure 5.3(a), via the analitic approximation showed in Figure 5.3(b). Our approximation of the FS consists of two separate hyperboloids of revolution, meant to simulate the main hole-like and electron-like sheets, whose radii at the center and at the top (and bottom) of the BZ are in the same proportions as in the real FS, although in Figure 5.3(b), the distance between them has been enhanced for clarity.

Taking into account all the considerations formulated so far, the model formulated in order to fit these curves contains two order parameter with s-wave symmetry, with different amplitude. The large gap is called Δ_1 and it is allocated on the hole band, while Δ_2 is the small gap, set on the electron sheet. The

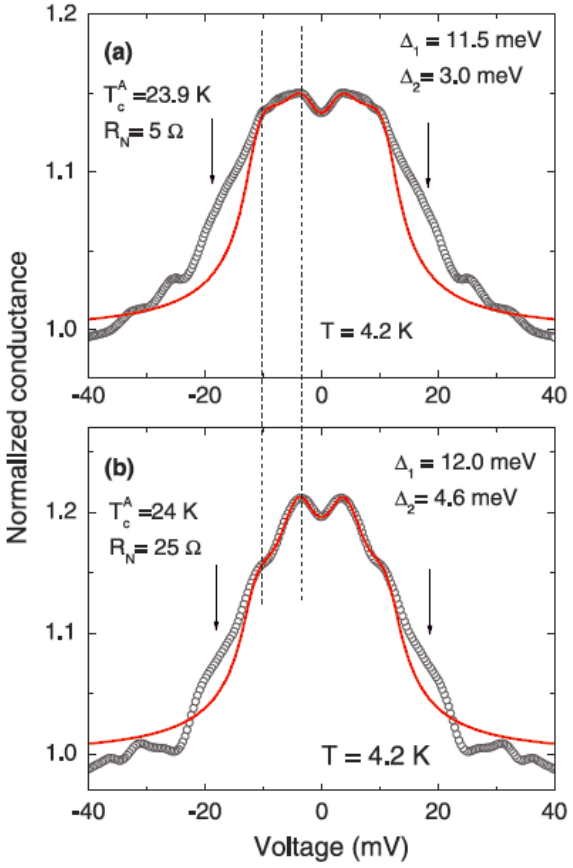

Figure 5.5: Two examples of normalized conductance curves of *ab*-plane point contacts in $Ba(Fe_{0.92}Co_{0}.08)_2As_2$ single crystals (black symbols) and of the relevant fit (red lines) with the 3D-BTK model using the FS shown in Figure 5.3(b). The fitting parameters of the curve in (a) are: $\Delta_1 = 11.5$ meV, $\Gamma_1 = 1.85$ meV, $Z_1 = 0.03$, and $\Delta_2 = 3.0$ meV, $\Gamma_2 = 3.60$ meV, $Z_2 = 0.31$. The weights of the two bands in the conductance are $w_1 = 0.23$ and $w2 = 0.77$. The parameters for the fit of the curve in (b) are instead $\Delta_1 = 12.0$ meV, $\Gamma_1 = 1.75$ meV, $Z_1 = 0.08$, and $\Delta_2 = 4.6$ meV, $\Gamma_2 = 3.00$ meV, $Z_2 = 0.245$. The weights in this case are $w_1 = 0.21$ and $w_2 = 0.79$.

model contains 3 adjustable parameters for each band, i.e. the gap amplitude Δ_i, the barrier parameter Z_i and the broadening parameter Γ_i, with $i = 1, 2$. The weight of each band is directly fixed by the shape of the Fermi surface and by the barrier parameter.

The values of the parameters used to obtain the best fit of the Figure 5.5 are indicated in the caption and summed in Table 5.1; the average values are $\Delta_1 = 11.75 \pm 0.25$ meV and $\Delta_2 = 3.8 \pm 0.8$ meV.
If the 2D-BTK model were considered to evaluate the best fit of the same curves the gaps turned out to be $\Delta_1 = 10.7 \pm 0.2$ meV and $\Delta_1 = 4.4 \pm 0.6$ meV. With respect to the 2D-BTK fit, the 3D one gives smaller values of the small gap and

larger values of the large gap, and the theoretical curves are narrower. This is

	Δ_1	Δ_2	Γ_1	Γ_2	Z_1	Z_2	w_1	w_2	T_c
curve (a)	11.5	3.0	1.85	3.60	0.030	0.310	0.21	0.79	23.9
curve (b)	12.0	4.6	1.75	3.00	0.080	0.245	0.21	0.79	24.0

Table 5.1: Parameter used in 3D-BTK model for $Ba(Fe_{0.92}Co_0.08)_2As_2$ single crystals. Here Δ_i and Γ_i are reported in meV and the T_c in K.

due to the fact that in the 3D model the weight is fixed (in these two cases, the weight of band 1 is about 0.2). Indeed, the 2D fit can be forced to follow the experimental curve at energies higher than 13 meV (where the 3D fit fails) if the weight of the bands is kept around 0.5, but this clearly would not reflect the real shape of the FS sheets. The inability of the model to reproduce the higher-energy structures (in particular the kinks at about 20 meV) simply confirms that these structures are related to effects that are not accounted for by the model (and indeed can be explained as being due to the strong electron-boson coupling, as shown in will be explained in Section 5.4).

5.3.4 $Ca(Fe_{1-x}Co_x)_2As_2$ single crystals

Having a look at Figure 5.6 it appears immediately clear that in the case here analyzed, i.e. single crystal of $CaFe_2As_2$ with 6% of cobalt doping, the situation is very different. The two curves depicted with black symbols show two examples of typical conductance curves of *ab*-plane contacts. Contrary to the case just analyzed, here zero-bias maxima or peaks appear in all the curves measured. This is a clear sign that one of the gaps is strongly anisotropic in the (k_x, k_y) plane.
Theoretical calculations [29] demonstrated that the pnictogen height h_{As} strongly reduces with the P substitution of As in $BaFe_2As_2$ and that this causes the increase of the outer hole-like FS sheet in the vicinity of the top and bottom faces of the BZ and that this can create the good condition for the appearance of nodal lines.

The DFT calculations here presented show that the effect of Co substitution in $CaFe_2As_2$ is very similar, and that the FS of Figure 5.4(a) is actually the extreme consequence of a doping-induced increase in the warping of the hole-like sheet. Thus, these PCAR measurements confirm that, even within a general s± picture of spin-fluctuation mediated superconductivity, nodal lines can appear in the hole-like FS when the latter is strongly deformed. In particular, it seems that the crucial point is the topological transition that splits into separate closed

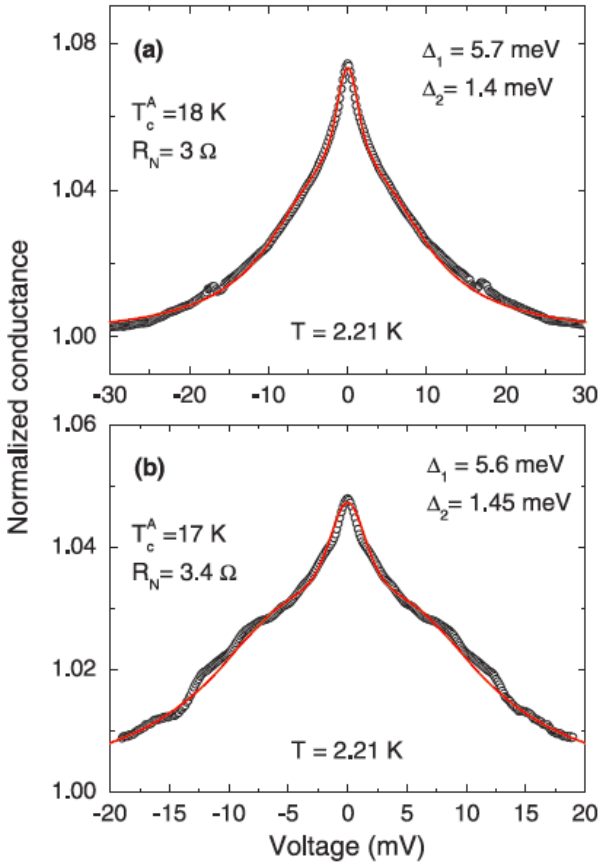

Figure 5.6: Two examples of normalized conductance curves of *ab*-plane point contacts in $Ca(Fe_{1?x}Co_x)_2As_2$ single crystals with $x = 0.06$ (black symbols) and of the relevant fit (red lines) with the 3D-BTK model using the FS shown in Figure 5.4(b). The fitting parameters of the curve in (a) are: $\Delta_1 = 5.70$ meV, $\Gamma_1 = 6.15$ meV, $Z_1 = 0.145$, and $\Delta_2 = 1.40$ meV, $\Gamma_2 = 1.25$ meV, $Z_2 = 0.050$. The parameters for the fit of the curve in (b) are instead $\Delta_1 = 5.60$ meV, $\Gamma_1 = 6.50$ meV, $Z_1 = 0.230$, and $\Delta_2 = 1.45$ meV, $\Gamma_2 = 1.70$ meV, $Z_2 = 0.050$. In both (a) and (b), the angle between the normal to the interface and the a axis is $\alpha = \pi/8$.

pockets the hole sheet.

Thus the FS has been modeled with one hyperboloid (for the electron-like sheets) and one spheroid (for the hole-like pocket) as in Figure 5.4(b) and assumed an isotropic large gap Δ_1 on the former and an anisotropic small gap Δ_2 on the latter.

The gap on the hole FS should be the evolution of the situation before the topological transition and should have a symmetry that produce the zero-bias maximum (and then the the probability of constructive interference between electron-like and hole-like quasiparticles). However to create this situation a change of sign of the gap is not absolutely necessary, the existence of angular regions where the gap has very small amplitude could also be sufficient [139].

Therefore we modeled the gap on the hole-like pockets with a fully anisotropic s-wave gap of equation $\Delta_2(\vartheta,\phi) = \Delta_2 \cos^4(2\vartheta)\sin^2\phi$ and the other one is fixed to be isotropic, as depicted by the gridded surfaces in Figure 5.4(b). The fit of the two spectra are reported with red solid lines in Figure 5.6. The parameters used for this fit are reported in the caption and summarized in Table 5.2. From different

	Δ_1	Δ_2	Γ_1	Γ_2	Z_1	Z_2	T_c
curve (a)	5.70	1.40	6.15	1.25	0.145	0.050	18.0
curve (b)	5.60	1.45	6.50	1.70	0.230	0.050	17.0

Table 5.2: Parameter used in 3D-BTK model for $Ca(Fe_{0.94}Co_{0.06})_2As_2$ single crystals. Here Δ_i and Γ_i are reported in meV and the T_c in K.

fits, we get the following average values for the gaps: $\Delta_2 = 1.4 \pm 0.1$ meV and $\Delta_1 = 5.5 \pm 0.3$ meV. If one chooses a d-wave symmetry for the small gap, a fit of comparable quality is obtained, but the values of the gaps are $\Delta_1 = 1.6 \pm 0.1$ meV and $\Delta_2 = 5.3 \pm 0.2$ meV [133].

5.3.5 $Ba(Fe_{1-x}Co_x)_2$ thin films

In Figure 5.7 two example of PCAR spectra obtained in $Ba(Fe_{1-x}Co_x)_2$ thin films with $x = 0.8$. The two spectra have been measured in two different kind of films: the (a) curve refers to a film on MgO substrate with Fe buffer layer, while the (b) curve was measured in a film on CaF_2.
Comparing the curves in Figure 5.7 the first thing that leaps out is that in the curve (a) some structures appear at energies similar to that of single crystal, but they are even clearer. On the other hand the curve (b) show much smoother structures, in particular the large gap manifests itself with very broadened shoulders at about ± 6 meV.
In the case of thin films the normal state at T_c^A is not related to the contact alone, but includes a contribution from the portion of the film between the point contact and the voltage electrode and this gives rise to some ambiguity to the normalization and consequently could affect the shape of the curve and, to some extent, the fitting parameters, actually the gap values are do not change, but the broadening Γ and the barrier parameter are most affected. In Figure 5.7 are reported fit obtained within the 3D-BTK model (blue dashed lines) where the same analitical form of the FS has been used (see Figure 5.3(b)). It is clear that the 3D-BTK model fails in well reproducing the curve of thin films because of a Z-enhancing effect due to the shape of the FS [139]. In fact, even if the values relate to the potential barrier are kept to zero in band 2 and to a very small vale in band 1 the very deep minimum at zero-bias cannot be removed. All

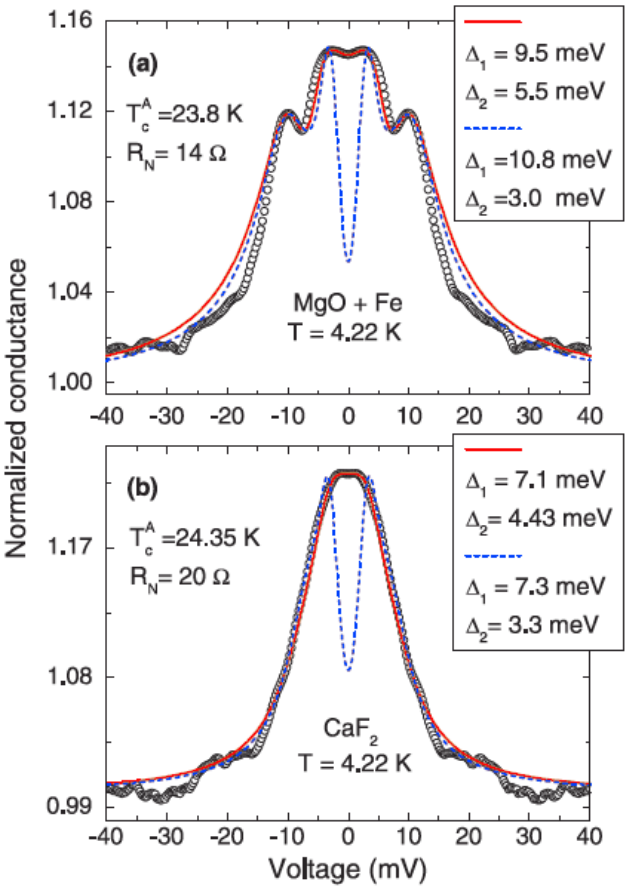

Figure 5.7: Two examples of normalized conductance curves of c-axis point contacts in $Ba(Fe_{1-x}Co_x)_2As_2$ films with $x = 0.08$ (black symbols) but on different substrates: MgO + Fe buffer layer in (a) and CaF_2 with no buffer layer in (b). The blu dashed lines represent the 3D-BTK fit, while solid lines represent the 2D-BTK fit. The corresponding gap amplitudes are indicated in the labels. The weights of the bands in the 3D fit are $w_1 = 0.39$ and $w_2 = 0.61$. The 2D fit was performed by fixing instead $w_1 = 0.44$ and $w_2 = 0.56$.

the parameters of the two fit shown in Figure 5.7 are reported for completness in the label and in Table 5.2. Several factors can be responsible of this failure. The first possibility is that, maybe caused by the roughness of the surface and then a not-oriented percentage of grains, the probe current is injected mainly along the *ab*-plane despite the orientation of the film. However, in the present case, this possibility is rather unlikely. The other possibility is that the use of two isotropic gaps is not the best choice to reproduce the real distribution of the gaps over the FS. Indeed, the presence of "hot spots" where the gap is significantly suppressed has been evidenced by Raman spectroscopy [132] and then justified theoretically [28]. The hot spots seem to reside on the electron-like FS sheets, then one might try to improve the model by using a small anisotropic gap with zeros and a large isotropic gap (as we did in the case of $Ca(Fe_{1-x}Co_x)_2As_2$). This would certainly improve the fit because the quasiparticle excitations, even

at very low energy, thanks to the anisotropy might compensate the Z-enhancing effect [139].

As already said, in the 2D-BTK model the presence of two more adjustable parameters allows sometimes a better fit. In this case the results obtained letting w_1 and w_2 to change with respect to the value obtained considering the real shape of the Fermi surfaces are reported in Figure 5.7 with the red solid lines. The fits are rather good in the energy region of the gaps and catch the main features of the curves but now the values of the two weight have not been determined from the FS.

All the adjustable parameters have been fixed to better reproduce the experimental curves and mediated over several different fit obtained changing the weight of the two bands. Their final values for the curve (a) are $\Delta_1 = 9.5 \pm 0.2$ meV and $\Delta_2 = 5.4 \pm 0.2$ meV, while for the curve (b) we obtained $\Delta_1 = 7.4 \pm 0.3$ meV and $\Delta_2 = 4.20 \pm 0.25$ meV. In the labels of Figure 5.7 and in Table 5.3 are reported the values used for the specific fit showed here.

	Δ_1	Δ_2	Γ_1	Γ_2	Z_1	Z_2	w_1	w_2	T_c
curve (a) 2D	9.5	5.5	0.47	1.85	0.95	0.12	0.44	0.56	23.80
curve (a) 3D	10.8	3.0	3.85	1.40	0.10	0.00	0.39	0.61	23.80
curve (b) 2D	7.1	4.4	4.00	2.16	0.36	0.14	0.50	0.50	24.35
curve (b) 3D	7.3	3.3	2.65	1.20	0.02	0.00	0.39	0.61	24.35

Table 5.3: Parameter used in 3D-BTK model for $Ca(Fe_{0.94}Co_0.06)_2As_2$ single crystals. Here Δ_i and Γ_i are reported in meV and the T_c in K.

Comparing these results with 2D-BTK fit of similar curves (with current injection along the c axis) in single crystals of the same material where $\Delta_1 = 9 \pm 1$ meV and $\Delta_2 = 4.1 \pm 0.4$ meV [140], a partial superposition of the gap values can be appreciated, although there is not a perfect agreement. This is not particularly surprising, first of all the situation in a thin film is more complex with respect that observed in single crystals and there may be some effect of the substrate, especially in the case of the films on Fe buffer layer; moreover, although the high quality of these thin films, the measurements highlight a certain degree of inhomogeneity in the superconducting properties. For these reasons the statistics of the measurements in films needs to be extended to draw definite conclusions.

5.4 Analysis of bosonic structures in AR spectra

The presence of bosonic resonances in the normalized conductance of the Andreev-reflection spectra is signal of strong electron-boson-interaction (EBI). These

structures appear in the sign-changed first derivative of the normalized conductance at $E_p \sim \Omega_0 + \Delta_{max}$ where Ω_0 is the characteristic bosonic energy and Δ_{max} is the maximum gap. Analyzing the temperature dependence of the peak energies we can obtain information about the representative bosonic energy and its nature [141].

5.4.1 The 2D-BTK model with Eliashberg theory

The mean-field BCS definition of a constant superconducting order parameter Δ is only a crude approximation of the physical reality. Actually, as described in Chapter 3, even in the weak-coupling regime Δ is a complex function of the energy as outlined in Eliashberg theory. Electron-boson structures appear in normalized conductance of quasiparticles tunneling or also in the Andreev-reflection regime if this energy dependence is taken into account.
By solving Eliashberg equations in a strong-coupling regime (within a model defined for each compound adjusting defining the number and the symmetry of the OP, the coupling, by means of the spectral functions, the Coulomb pseudopotential μ^* on the base of experimental data and theoretical calculations) it is possible to obtain the full energy dependence of the order parameter $\Delta(E)$. The imaginary part of the order parameter increases at the increase of the coupling and accounts for the finite lifetime of Cooper pairs. Since the BTK theory and its modifications reduces to the BCS theory for superconducting tunnel in the limit of large Z it is easy to predict that the introduction of $\Delta(E)$ into the BTK expressions will lead to electron-phonon interaction structures in the normalized conductance for any Z value in the ballistic regime [142, 143]. This can be done because the BTK theory contains operators which do not affect the energy.
As can be seen in in Figure 5.8 in the simple case of lead, that is a 'classic' strong-coupling superconductor for which the spectral function is known and $\mu^* = 0.11$ at $eV \approx \Delta_{Pb} + E_{ph}$ (where E_{ph} represents the range of energies of the electron-phonon spectral function of lead) the electron-phonon interaction structures appear for any Z value but their amplitude increases with Z Figure 5.8(a). In Figure 5.8(b) the sign-changed first derivative of the normalized conductance $-dG/dV = -d^2I_{NS}/dV^2$ vs. V is compared to the lead spectral function (top red curve). The positions of the structure hardly change when Z decrease, this means that it is possible to use the same law of the tunneling case to obtain the characteristic bosonic energy.
The BTK model is suitable only for isotropic superconductors. It is possible to relax this condition and describe Andreev-reflection point-contact spectroscopy also for anisotropic superconductors. However this is not the case of the compound under discussion here that can be described by an isotropic model, where

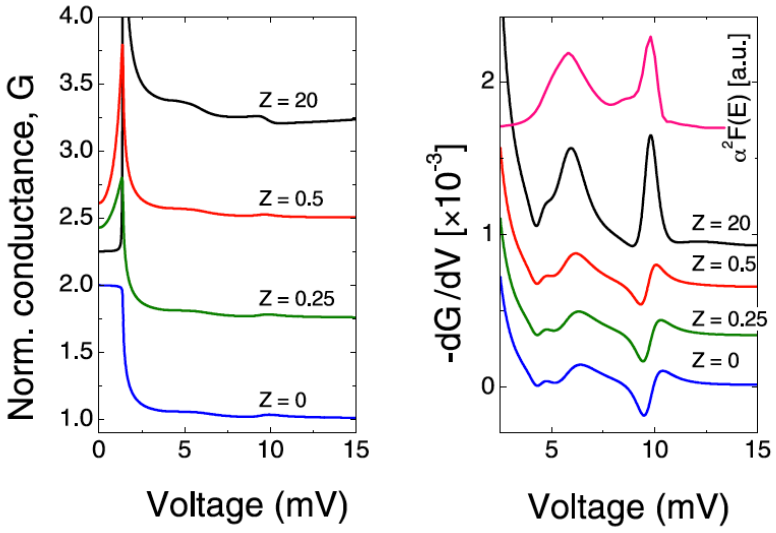

Figure 5.8: Normalized conductance and sign changed voltage derivative of the normalized conductance $-dG/dV$, for different Z values within the 3D BTK model in the Pb case [126]. The curve represents the Eliashberg spectral function and its is here reported in arbitrary units (it is translated of a value equal to the amplitude of gap).

the order parameter have opposite sign on the different sheets of the FS (this characteristic that cannot be appreciated by tunnelling or Andreev reflection measurements that are not phase sensitive).

5.4.2 $Ba(Fe_{1-x}Co_x)_2$ thin films

In particular PCARS measurements on a thin film of $Ba(Fe,Co)_2As_2$ with 8% of cobalt content are now considered, for example the spectrum described by symbols in Figure 5.9. A possible bosonic resonance appears around 20-25 meV. The following line of reasoning has to be followed in order to verify that this is really correlated to the electron-boson interaction. First of all the analysis with the standard two bands 2D-BTK model (the blue curve in Figure 5.9) has been done. In this way it is possible to obtain two gap values and, from their temperature dependence, the critical temperature, this gave as results Δ_1=Δ_e=4 meV, Δ_2=Δ_h=7 meV and T_c=25.4 K [140].
Furthermore on the base of the phenomenological relation between Ω_0 and T_c, valid in almost all iron-compounds and already verified also for $Ba(Fe,Co)_2As_2$ [140] the characteristic bosonic energy can be taken to be $\Omega_0 = 11$ meV. This value supports the picture of a pairing mediated by antiferromagnetic spin fluctuations and it is in good agreement with neutron inelastic scattering [104]. At this point an analysis within a three bands s± Eliashberg model, is possible [140]. Here there is one holonic order parameter that has opposite sign with respect to the

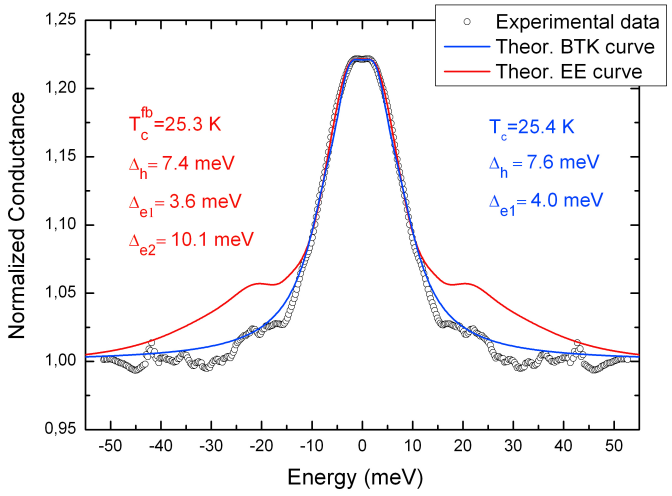

Figure 5.9: Andreev reflection spectra at 4.2 K in Ba(Fe$_x$Co$_{1-x}$)$_2$As$_2$, with x=8%. The dark blu curve is the usual BTK fit, and the orange curve is the fit obtained with the inclusion of the Eliashberg theory.

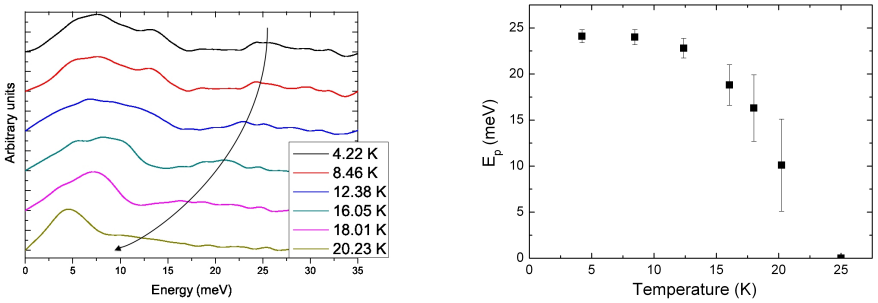

Figure 5.10: Temperature dependence of the bosonic stuctures in Ba(Fe$_{1-x}$Co$_x$)$_2$As$_2$ thin film with x=8%. In the left panel is depicted the temperature dependence of the sign-changed first derivative of the normalized conductance spectra. The black arrow indicates the evolution in temperature of the resonance. And the right panel shows the temperature dependence of the energy of the peak in the sign-changed first derivative of the normalized conductance spectra.

two electronic ones and now the coupling is present only between the holonic (indicated by the index 2) and the electronic bands (indicated by the index 1 and 3) i.e. $\lambda_{23} = \lambda_{e1,e2}$=0. In these calculations, in order to describe the electron-boson spectral function a lorentzian spectral function peaked at Ω_0 with FWHM of 4 meV [140] has been chosen. In order to fix the free parameter $\lambda_{12} = \lambda_{h,e1}$ and $\lambda_{13} = \lambda_{h,e2}$, the Eliashberg equations have been solved to reproduce the low temperature gap values and the values obtained are $\lambda_{h,e1} = 0.50$ and $\lambda_{h,e2} = 1.65$,